ABSTRACT

SOFTWARE AND HARDWARE IMPROVEMENTS FOR DIGITAL SOLAR MAGNETOGRAPH SYSTEM

by

Shu Yang

Digital solar imaging systems have been widely used in solar observations. Their high resolution, high rate of image acquisition and convenience for off-line image processing have provided significant improvements to solar physics research. In this project, two digital magnetograph systems established at Big Bear Solar Observatory (BBSO) have been described. One is used to provide a high frame rate magnetogram system, and the other provides a real-time image alignment, i.e., a correlation tracker system.

The developed correlation tracker system consists of a high-speed 64x64 CCD camera, an EDT image grabbing board, an agile mirror, a D/A board and a Sun Ultra-30 workstation. Based on the same hardware, digital magnetograph system has been built and tested. The novel correlation tracker system does not use traditional FFT hardware and is more integrated in a Sun Ultra-30. The system software has been developed by using C and Motif graphical user interface under Solaris 2.6. Both systems have been demonstrated to work very efficiently at BBSO.

After tens of thousands of solar magnetograms have been grabbed with the digital magnetograph system, various image processing methods have been studied to improve resolution, eliminate image noise and stray light effect. The efficiencies of different processing methods have been discussed and their Fourier spectra have been analyzed. After noise deduction and stray light elimination, the processed magnetograms have been proved to be much better than the original images.

SOFTWARE AND HARDWARE IMPROVEMENTS FOR DIGITAL SOLAR MAGNETOGRAPH SYSTEM

by
Shu Yang

A Dissertation
Submitted to the Faculty of
New Jersey Institute of Technology and
Rutgers, The State University of New Jersey - Newark
In Partial Fulfillment of the Requirement for the Degree of
Doctor of Philosophy in Applied Physics

Federated Department of Physics

May 2001

APPROVAL PAGE

SOFTWARE AND HARDWARE IMPROVEMENTS FOR DIGITAL SOLAR MAGNETOGRAPH SYSTEM

Shu Yang

Dr. Haimin Wang, Dissertation Advisor — Date
Professor of Physics, NJIT

Dr. Philip R. Goode, Committee Member — Date
Professor of Physics, NJIT

Dr. Ken K. Chin, Committee Member — Date
Professor of Physics, NJIT

Dr. Nuggehalli M. Ravindra, Committee Member — Date
Professor of Physics, NJIT

Dr. Dale E. Gary, Committee Member — Date
Associate Professor of Physics, NJIT

Dr. Zhen Wu, Committee Member — Date
Associate Professor of Physics, Rutgers University, Newark

BIOGRAPHICAL SKETCH

Author: Shu Yang

Degree: Doctor of Philosophy

Date: May 2001

Undergraduate and Graduate Education:

- Doctor of Philosophy in Applied Physics,
  New Jersey Institute of Technology, Newark, NJ, 2001
- Master of Science in Applied Physics,
  Northwestern Polytechnical University, Xi'an, P.R.China, 1988
- Bachelor of Science in Physics,
  North West University, Xi'an, P.R.China, 1982

Major: Applied Physics

Presentations and Publications:

Haimin Wang, C. Denker, Tom Spirock, P. R. Goode, S. Yang, W. Marquette, J. Varsik, R. J. Fear, J. Nenow and D. D. Dingley,
"New Digital Magnetograph At Big Bear Solar Observatory", Solar Physics, vol. **183**, no. 1, pp.1-13, November 1998

Jingshan Wang, Haimin Wang, Nuggehalli M. Ravindra, Philip R. Goode, Feiming Tong, Shu Yang and T. Spirock,
"Solar Near-Infrared Filter System", AGU Spring Meeting, SH21C-03, Boston, May, 1998

Haimin Wang, Carsten Denker, Thomas Spirock, Shu Yang, Philip Goode,
"New Digital Magnetograph at Big Bear Solar Observatory", American Astronomical Society, SPD meeting, #28, #15.03, Boston, May 1997

Shu Yang,
"Computer generated holographic lens with detour phase coding", Acta Photonica Sinica, suppl., vol **23**, pp. 103-109, 1994

Shu Yang, Changxing Dong, Bingbo Wei,

"High undercooling and rapid entectic growth of Sn-38.1%Pb alloy", Proceedings of First Chinese National Conference on Phase Transformations, pp. 333-336, Beijing, China, 1993

Shu Yang, Changxing Don, Bingbo Wei,

"Microstructural morphology of faceted-growth phase grown in undercooled eutectic alloys", Proceedings of Third China-Russia-Ukraine Symposium on Astronautical Science and Technology, pp.716-719, Xi'an, China, 1994

Chnagxing Dong, Shu Yang,

"Undercooling and phase separation of Cu-Pb monotectic alloys", Proceedings of Third China-Russia-Ukraine Symposium on Astronautical Science and Technology, pp.720-723, Xi'an, China, 1994

Changxing Dong, Shu Yang,

"Undercooling and rapid dentritic growth of Ni-10%Fe alloys", Journal of Northwestern Polytechnical University, vol. **12**, no. 2, pp.334-336, 1994

Shu Yang, Nuo Wang,

"A research on optical current induced by laser", The First Shannxi Conference on Laser Optics, Xi'an, China, 1989

Changxin Dong, Shu Yang, Bingbo Wei,

"Undercooling and rapid crystal growth of Ag-Ge eutectic alloy", Acta Photonica Sinica, vol. **23**, pp. 221-225, 1994

To My Beloved Family

ACKNOWLEDGMENT

I would like to express my deepest appreciation to Dr. Haimin Wang, who has been not only my research supervisor, providing valuable help and countless resources, but also my precious friend, constantly giving me support, encouragement and reassurance.

Very special thanks to Dr. Dale E. Gary and Dr. Nuggehalli M. Ravindra for their precious comments and careful inspection of this dissertation. Without their help, this dissertation could not have been done. I also appreciate the opportunity that Professors Gary and Ravindra gave me in sharing my experience and advising me on my future.

I also want to thank Tom Spirock for building the control part of the liquid crystal, Owen Phairis for building the Bessel filter and Leonid Didkovsky for testing Correlation Tracker at BBSO. Their contribution has been crucial in building the Correlation Tracker at Big Bear Solar Observatory. Also, I must thank Dr. Jongchul Chae, whose great help has been reflected throughout the study of stray light elimination.

Thanks are also given to Dr. Philip R. Goode, Dr. Carston Denker, Dr. John Varsik, for their help in my project. Special thanks have to be given to Dr. John Federici and Dr. Ken K. Chin, who have shown their great kindness and given me most valuable care during the hardest time in my life. Finally, thanks are also given to Dr. Zhen Wu for participating in my committee.

Many of my fellow graduate students in the Center for Solar Research are also deserving of recognition for their support.

This work was supported partially by NASA SRT program (NAG5-9682), NSF Solar-Terretrial program (ATM-9628862).

TABLE OF CONTENTS

TABLE OF CONTENTS
(Continued)

Chapter **Page**

TABLE OF CONTENTS
(Continued)

Chapter **Page**

LIST OF TABLES

LIST OF FIGURES

LIST OF FIGURES
(Continued)

LIST OF FIGURES
(Continued)

CHAPTER 1

INTRODUCTION

1.1 Objective

The objective of this dissertation is to build two digital image systems in Big Bear Solar Observatory, a digital solar magnetograph system and a real-time image alignment system, i.e., correlation tracker system. Also, after obtaining the digitized magnetographs, different image processing methods have been applied to deduct the image noise and stray light effect. The properties of different methods have been studied both in space domain and Fourier domain.

1.2 Solar Magnetogram

Nearly 1,392,000 km in diameter and $1.99\text{x}10^{30}$ kg in mass, the sun is the geometric and gravitational center of the planetary system. Because of the high temperature, solar materials are actually in an ionized plasma state [1], which refers to a gas of ionized atoms. Since the sun is an ionized gas sphere, when speaking of the solar surface, one is not referring to a solid surface, but rather to the photosphere, a fictitious spherical surface from which the bulk of solar radiation originates.

There is no question today among solar astronomers about the fundamental importance of the solar magnetic field in most of the physics of the sun. In the visible layers of solar atmosphere, this field is shaping and controlling the solar plasma, providing the energy source for the explosive phenomenon, like solar flares, forming sunspots, appearing in supergranular cell boundary as subarcsecond (1 arcsec $\approx$ 730km) concentrations of kilogauss field strengths and interacting with the convective motions of the subsurface plasma to produce the solar cycle. This fundamental role of the magnetic field has prompted the development over years of instruments to measure the field.

The goal of magnetic field observations are to measure the magnetic structure as large with dynamic range and with as high resolution as possible. Magnetograph observations with high resolution and sensitivity are essential to help us to understand the magnetic field in the quiet sun, and associated flow motions [2]. The interaction between magnetic field on the sun and the convective flows has been a fundamental topic in solar physics.

The fundamental method of measuring solar magnetic field at most ground-based solar observatories is the Zeeman effect. From the Zeeman effect, the frequency and wavelength of a spectral line will be split according to,

$$\Delta\nu = \frac{Z}{h} g \cdot \mu_B \cdot B, \tag{1.1}$$

$$\Delta\lambda = \frac{Z}{hc} g \cdot \mu_B \cdot \lambda^2 \cdot B, \tag{1.2}$$

where g is the Lande factor that depends on angular momentum quantum numbers of the state, Z is the number of electrons, μ_B is the Bohr magneton and B is the magnetic field. $\Delta\nu$ is the amount of frequency split. Because B is very weak except in sunspots, usually the magnetic field cannot be measured directly from the above formula.

The study of magnetic fields on the Sun was revolutionized by the development of the magnetograph by Harold Babcock [1] in 1953. In the Zeeman effect, one line splits into three components: π and σ. π is the undisplaced component and σ is the component corresponding to $\pm\Delta\nu$ lines with $\Delta m = \pm 1$. Both lines are seeing as left- and right-hand circularly polarized along the direction of the magnetic field. If a liquid crystal is put in the system, it produces a retardation of $\pm\lambda/4$, which changes the circularly polarized σ components into two beams linearly polarized at right angles to one another. By putting a polarizer behind the liquid crystal, an image from one σ component can be obtained at a time. Using this method, two magnetic component images are obtained. The difference between the two images is proportional to the longitudinal magnetic field. By this means, the magnetic field is measured.

1.3 Correlation Tracker

A correlation tracker is a real time image correction system based on hardware that can eliminate the image shift in real time. Figure 1.1 shows a basic diagram of the Correlation Tracker system. For a real time correlation tracker, besides the CCD camera and image grabbing board, a tilt mirror and a D/A board is also required to provide a tool to adjust the optical system rapidly. In the old type of correlation tracker, all the FFT calculations are carried out by a hardware unit, a FFT unit, and the image sensor array and A/D converter are realized by using separate hardware. In the new generation of correlation tracker, all of the separate hardware components have been integrated into one high-speed workstation, and the software has played a more central role in the whole system, performing the FFT and calculating the corresponding error signal.

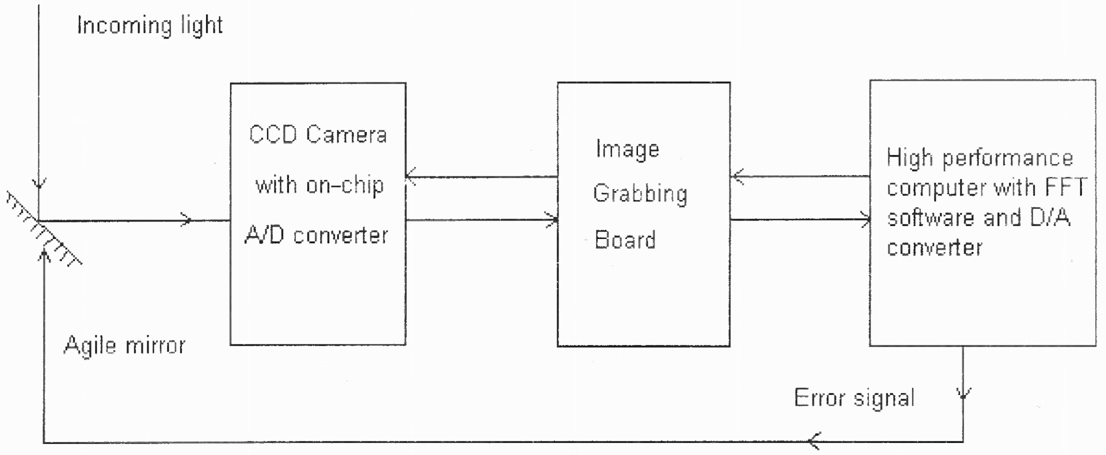

Figure 1.1 Correlation Tracker

1.4 Digital Magnetograph System

Charge Coupled Device (CCD) cameras are widely used in many imaging applications. Though most of the CCD cameras use an analog output [7], with the help of high data depth CCD camera and a fast speed image grabbing board, the digital magnetograph system with high-resolution digital output has become more feasible [3-6].

The Video Magnetograph (VMG) system has been widely used for many years at the Big Bear Solar Observatory (BBSO). But the system's shortcoming is also very evident due to longer image exposure time and only 8 bits dynamic range [8]. By using a digital magnetograph system, not only the above shortcoming can be overcome, but also it provides us a very wide range of image processing options that can be either performed in real time or after the fact. The basic control part of the digital magnetograph system has been described in Figure 1.2.

The control part of the digital magnetograph system consists of a digital camera, an image grabbing board, a computer and corresponding software. The grabbed image can either be stored in the image buffer to gain a very high image grabbing speed or be stored in the large external hard disk. Also, some real time image processing method can be used during the image-grabbing period, such as image alignment. Compared to the old Video Magnetograph (VMG) system, the digital magnetograph system can significantly improve the sensitivity and spatial resolution with the help of a high resolution CCD camera and high frame grabbing speed. The resolution of the CCD camera and the image frame grabbing speed of the image board are two key components that determine the quality of the whole system. The software development will focus on user-friendly interface design and some online image processing routines.

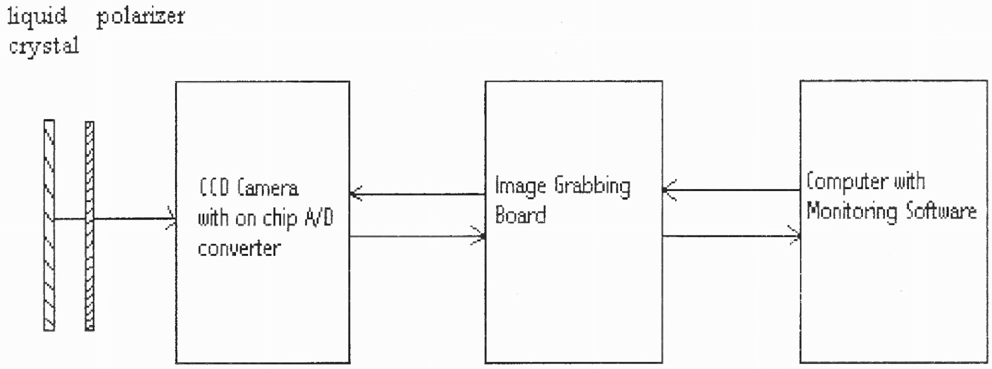

Figure 1.2 Digital Magnetograph System

1.5 Digital Magnetogram Processing

Digital image processing has been widely used in astronomical science [9-15]. The main object of our task is to find the best way to reduce the different kinds of noise and to improve resolution in solar magnetograms. To construct a magnetogram, there are three main elements that can influence the image quality significantly [9-10], the white noise, the seeing and the stray light effects. The main purposes of the digital solar magnetogram processing can be divided into two main functions: increasing the spatial resolution and reducing the noise.

In a raw digital solar magnetogram, the noise is widely dominated by the white noise. The white noise comes from any randomly distributed fluctuation that may come from CCD camera's readout noise or digitization noise. Unfortunately, in a single image, noise cannot be reduced because it is not separable from the signal. But because of its random nature, the noise is different from one image to the next. Adding m images multiplies the signal by a factor of m and the noise by a factor of only $\sqrt{m}$. Then the signal-to-noise ratio has been multiplied by a factor of $\sqrt{m}$ [11]. This property of the noise provides us a very good tool to reduce the noise scale by image averaging. By using image selection before doing image averaging, the noise can be even more effectively reduced.

Another element in reducing the image contrast comes from the bad seeing, which usually comes from the disturbance of the earth's atmosphere [1], and results in image motion and smearing between different images and also between different parts in a single image. One effective tool to eliminate part of the seeing is to use the cross-correlation method [12-14] to find the shift between images or the destretching method to find the shift between different parts in an image, and shift them back. If the cross-correlation is being done in real time by hardware, the corresponding system is then called a Correlation Tracker [15-21].

The stray light that comes from the atmosphere and optics of the instrument is another element in reducing the image contrast, and can be divided into large-scale scattering light and small scale blurring light [2-3]. To eliminate the stray light, several methods have been intensively researched, like deconvolution [22-31], Gauss fitting with Wiener filter[32, 33], and maximum entropy [2, 3, 34-39]. All these methods are based on the system's point spread function or its Fourier transformation, i.e., the Modulation Transfer Function (MTF).

The role of image processing is not to invent the details that have disappeared at the telescope. It is to transform an image with the aim of seeing better the details inside. It is impossible to obtain a good processed image from a poor raw image, as the details have already been irretrievably lost.

CHAPTER 2

CORRELATION TRACKER

2.1 Cross-Correlation Method

Image motion can significantly affect the resolution of an astronomical telescope. Observations that are taken with exposures longer than the timescales of the motion are usually severely degraded, such as integrated magnetograms. Image motion originates from instrument shake and guiding errors as well as from random wavefront tilts averaged over telescope entrance aperture which are caused by atmospheric turbulence.

Image motion compensation systems constitute the simplest systems that actively correct atmospheric disturbances, commonly termed "adaptive optics" [16]. But the atmospheric resolution can be partially improved by simply using correlation relation method.

The definition of cross-correlation relation between two functions *f(x,y)* and *g(x,y)* is,

$$f(x,y)\otimes g(x,y)=\int f^{*}(u,v)\cdot g(u+x,v+y)dudv, \tag{2.1}$$

where ⊗ denotes correlation operator and * denotes conjugate operator.

Consider two images $i_1(x,y)$ and $i_2(x,y)$, and the second image has a small shift x, y with respect to the first image. The cross-correlation relation between the two images is,

$$i_1(x,y)\otimes i_2(x,y)=\int i_1^{*}(u,v)\cdot i_2(u+x,v+y)dudv. \tag{2.2}$$

Take Fourier transformation on both sides,

$$FFT[(i_1(x,y)\otimes i_2(x,y)]=I_1^{*}(u,v)\cdot I_2(u,v), \tag{2.3}$$

where, $I_1(u,v)$ and $I_2(u,v)$ are Fourier transform of $i_1(x,y), i_2(x,y)$ respectively.

If the second image is shifted back with the same x,y, then i_1, i_2 will be totally identical and the above cross-correlation will become a self-correlation. Thus their multiplication will reach its maximum,

$$I_1^*(u,v) \cdot I_2(u,v) = I^2(u,v). \qquad (2.4)$$

When using the correlation principle, first, a reference image has to be determined, then the cross-correlation in the Fourier domain is calculated for each image relative to the reference image. The maximum position in the cross-correlation will be the image shift.

The procedure to use the above principle to correct image shaking is as follows: The CCD camera continuously scans the solar surface at the region of interest, such as the solar granulation pattern. At the beginning, the image is stored as a reference. During the working procedure, successive images are compared with the reference image, and relative shifts are measured. The shifts are then converted into error signals and sent to a D/A board, which are applied to an agile mirror in order to reposition the image.

2.2 Correlation Tracker

Correlation systems that measure motions on the Sun have been studied for some time [15-21]. The recent advent of fast digital hardware has made the construction of correlation trackers feasible and affordable. Up to now, most image stabilization systems for solar observations have been the so-called spot trackers [17]. The movement of a distinct, high contrast feature such as a sunspot, is measured with a simple quadrant detector and compensated with a tilt mirror in the optical path. However, distinct, high contrast features are in general not close enough to most areas of interest. So alternative techniques are required to sense the movements of arbitrary target regions.

Unlike the spot tracker, the correlation tracker is specially designed to lock on low contrast features such as solar granulation or other small-scale structures [17]. It is a simple adaptive system that stabilizes atmospheric and instrumental image motion. The live images collected from the telescope are compared to a previously stored reference image and they are cross-correlated in real time. The reference images are frequently updated in order to adapt to the changing small-scale features. The error signal is derived from measuring the position of the maximum of the cross correlation. The error signal is then sent to a D/A board, magnified by a high voltage amplifier, then to control the adjustable mirror to eliminate the shift. The basic diagram of a correlation tracker is shown as in Figure 2.1.

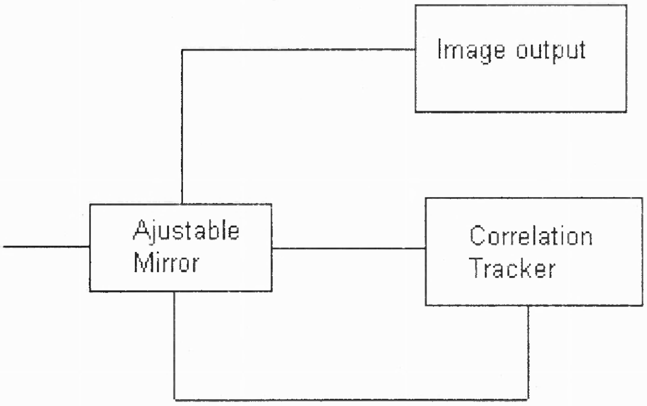

Figure 2.1 Correlation tracker, a simple illustration.

Recent performance tests show that the residual image motion in the tracked image is 0.05 arc sec rms compared to a typical 0.5 arc sec rms for untracked image [21]. The bandwidth of the tracking system is approximately 40Hz and thus clearly sufficient to stabilize image motion on a meter class telescope with a field of view below 10”[17].

Several correlation tracker systems for solar image motion control have been developed or are under development [15-21]. The first such system to successfully compensate image motion of a ground-based solar telescope was the breadboard correlation tracker built by the solar physics group at Lockheed Palo Alto Research Laboratory [15]. This system was designed for image motion compensation in a space borne solar telescope. Previous correlation tracking systems are all established upon the hardware FFT unit system. The typical main components of this kind of correlation tracker system are shown in Figure 2.2 [17].

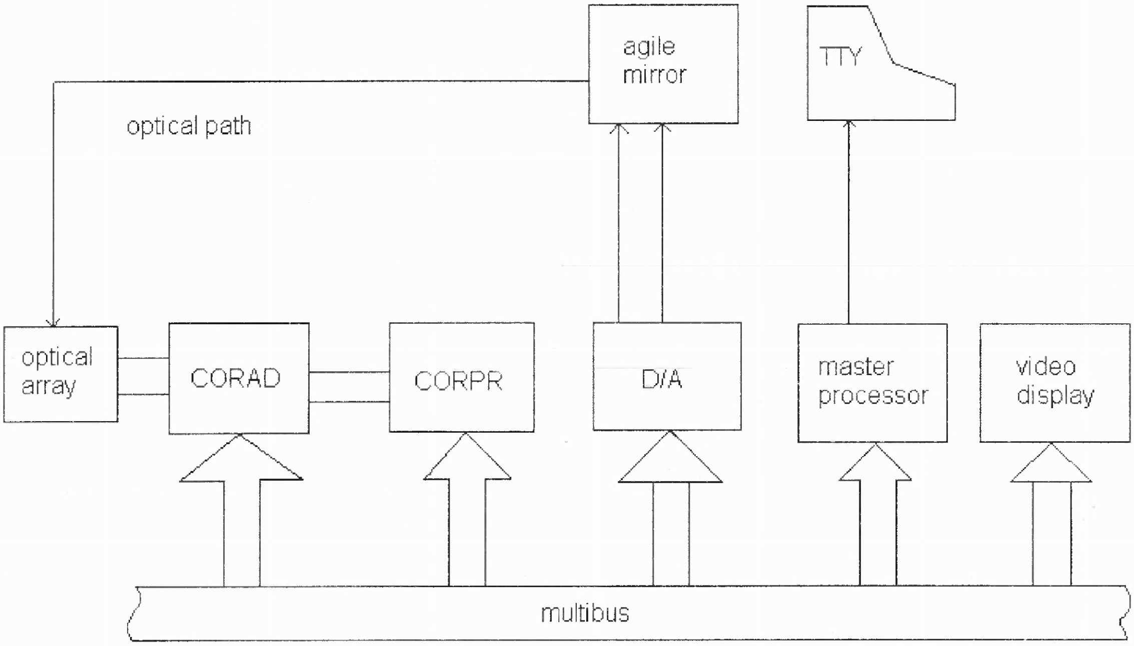

Figure 2.2 Correlation Tracker based on hardware FFT component.

The various components in Figure 2.2 are as follows:

- CORAD is the correcting analog to digital converter. This component digitizes data from the array detector, and presents clean data to the correlation processor for further analysis.
- CORPR is the correlation processor. This processor accesses data from CORAD through a high-speed bus and computes its Fourier transform with fast, dedicated hardware. For reasons of processing speed, only a 16 by 16 pixel subfield is actually processed by CORPR. This component generates a cross covariance function, which is accessible to the master processor.
- The master processor provides the user interface, initializes and supervises hardware and schedules tracking tasks. Mirror drive signals are generated by the master processor, which determines the peak position in the covariance function produced by CORPR.
- A four channel digital-to-analog (D/A) converter.
- A video display board, which is used to monitor the performance of the system.
- An agile mirror.

2.3 Correlation Tracker at Big Bear Solar Observatory

The correlation tracker project at BBSO started in 1997. The principle of this Big Bear correlation tracker is based on the same cross-correlation method as described above. However, the realization is quite different from all the present correlation tracker systems. The Big Bear correlation tracker consists of three parts: image acquisition, image FFT and the shift calculation, D/A converter and error signal driving process. The main difference between this correlation tracker and the existing ones is that all the data processing is accomplished by using a Sun Ultra-30 workstation and no special hardware is needed to perform the FFT, such as CORPR as described above. Since a CCD camera with digital output has been used, CORAD is no longer needed and the A/D process is being executed by an on-camera A/D chip. The system block diagram is shown in Figure 2.3.

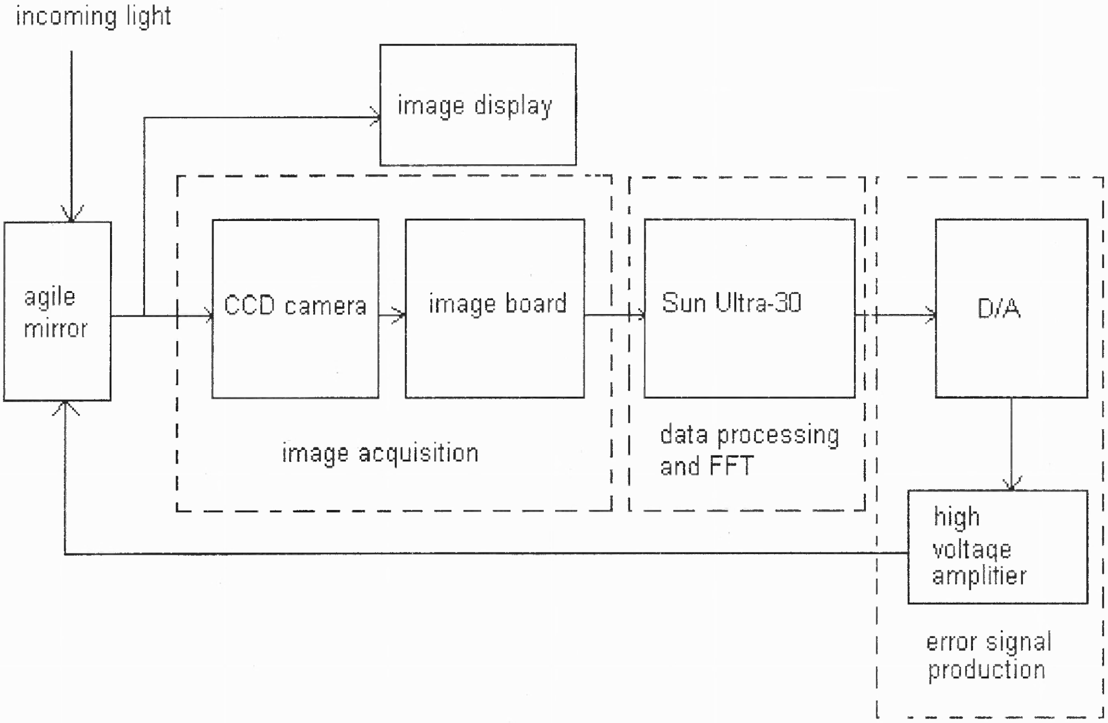

Figure 2.3 Correlation tracker at BBSO.

The image acquisition part consists of a Dalsa CCD camera and an image grabbing board. The FFT and data processing part is simply accomplished by Sun Ultra-30 workstation. An analog error signal is produced and amplified by a D/A board and a high-voltage amplifier. Since the FFT and data processing are accomplished by the Sun

Ultra-30, the software development was a key component in the Big Bear correlation tracker system.

2.4 Image Acquisition

2.4.1 CCD Camera

The CCD camera used in the BBSO correlation tracker is a CA-D10064T area scan camera made by Dalsa. Dalsa specializes in high performance solid-state CCD image sensors and modular cameras. Its cameras provide the maximum resolution at the highest data transfer speed of known products in the industry. The CA-D10064T camera has a 64x64 pixel x 12bits digital image with a typical frame rate of 1310/s without binning and 2480 with 2x2 binning enabled. The pixel size is 16μm x 16μm. The data transfer speed is 10MHz. All User Bus controls use RS422 format. RS422 is an electrical specification for the transmission of digital data. The standard is available from the EIA(Electronic Industries Association). It defines voltage levels, expected transmission speeds over various cable lengths, common mode voltage operating requirements for transmitters and receivers, and input impedances and sensitivities for receivers. RS422 requires the use of shielded twisted pair cable. Figure 2.4 shows a graph of ideal communication data rate vs. cable length for the RS422 standard.

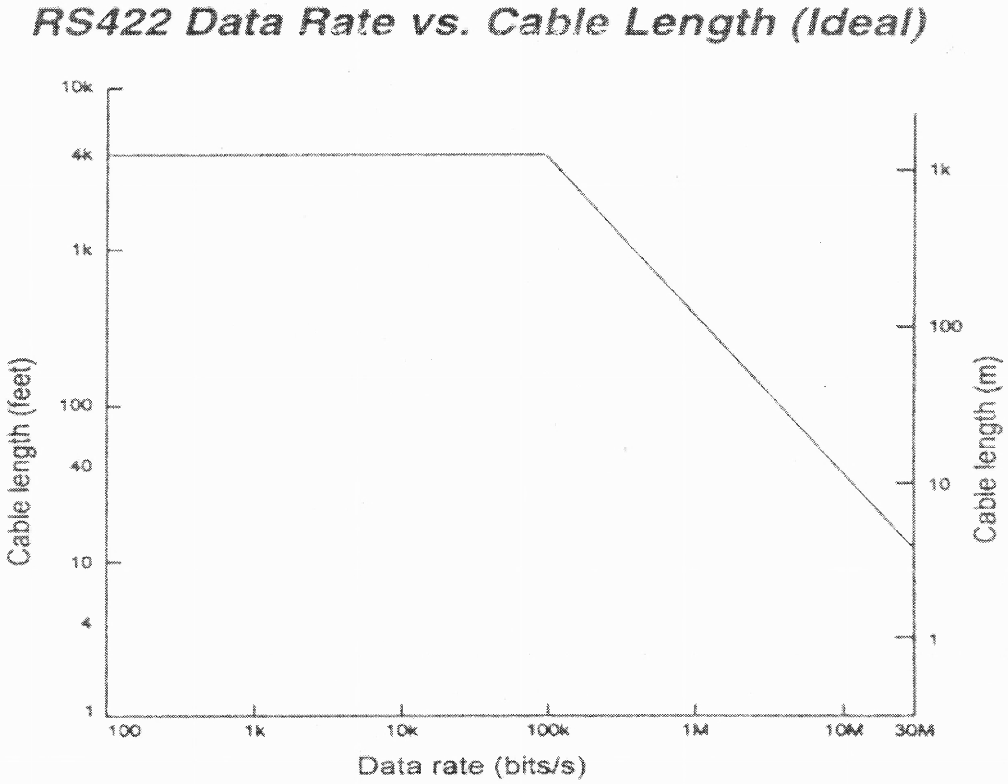

Figure 2.4 Data rate vs cable length.

From the graph, if the image frame grabbing speed is about 1000 frames per second with a 2x2 binning mode, the cable length should be within 10 meters. This is the cable length that has been used at BBSO.

Since the research in National Solar Observatory at Sunspot shows that the servo system's bandwidth of 40Hz will be clearly sufficient to stabilize image motion on a meter class telescope (the detector in Sunspot's correlation tracker can be scanned with a rate of 976 pictures per second), the CA-D10064T has been considered a suitable CCD camera for the correlation tracker. The main configurations of CA-D10064T CCD camera are shown in Tab 2.1 [48].

Table 2.1 CA-D10064T Major Configuration [48]

Calibration Conditions, 64x64	**Units**	**Min.**	**Typ.**	**Max**
Frame Rate	Hz	819	1310	1638
Frame Rate (with 2x2 binning)	Hz	1550	2480	3100
Light Intensity	μW/cm^2	43.8	70	88
Light Intensity (with 2x2 binning)	μW/cm^2	20.7	33.1	41.6
Test Specification, 64x64				
Saturation Output Amplitude	DN	3800	3950	4095
Fixed Pattern Noise	DN	4	15	
Fixed Pattern Noise (2x2 binning)	DN	8	30	
Random Noise	DN	3	4	
Random Noise (with 2x2 binning)	DN	4	5	

The CA-D10064T hardware interface is shown in Figure 2.5.

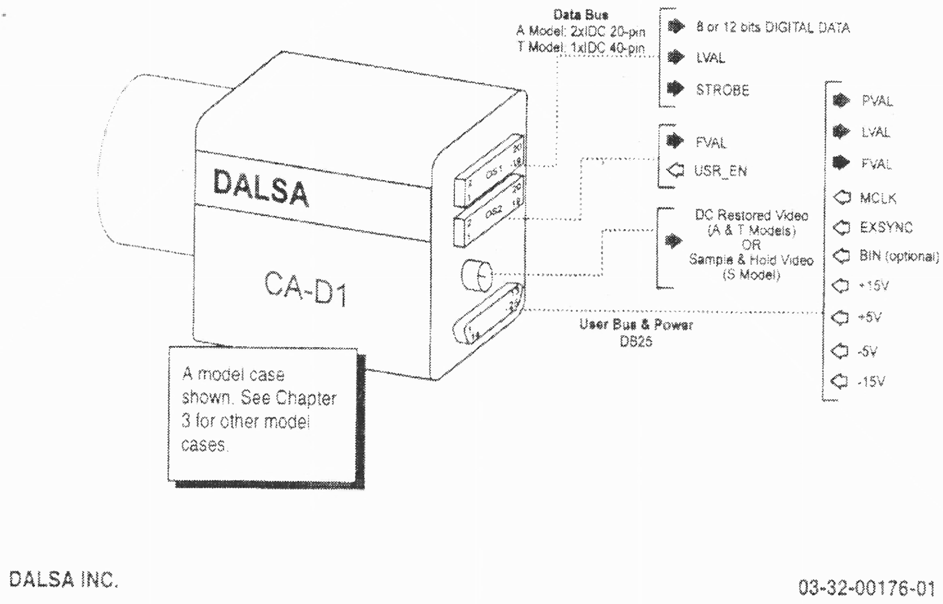

Figure 2.5 CA-D10064T hardware interface.

The pixel binning is available as an option on CA-D10064T. The principle of 2x2 binning mode is shown in Figure 2.6.

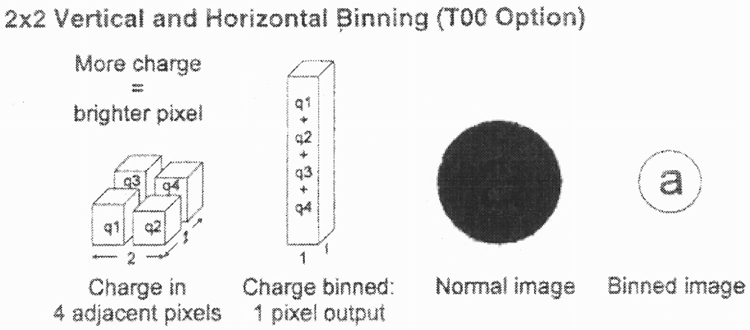

Figure 2.6 Binning mode.

For binning-enabled cameras, BIN high causes the image sensor to combine the charges in adjacent pixels, increasing sensitivity and frame grabbing speed while reducing image resolution. From Figure 2.5, the BIN is an optional signal. It can be fulfilled either by hardware or by software control. Due to the speed consideration, the CA-D10064T works with a 2x2 binning mode in Big Bear Correlation Tracker and the software binning control is being used.

2.4.2 The Image Grabbing Board

2.4.2.1 General Description The image grabbing board used in the BBSO correlation tracker is a PCI-DV image board from EDT Company, which uses the Digital Video Camera Interface standard for PCI Local Bus Computers. EDT company is the first to set new standards with single-slot interface boards developed for the Sun SPARCstation and it is the only CCD camera interface fully tested by Sun (Test result shown in Table 1.3).

The PCI DV board is a single-slot PCI bus board that implements a high speed DMA channel between an external digital video camera and a UNIX-based workstation. Due to the high speeds and large amounts of data involved, the system must have at least 300MHz or faster processor and 128Mb minimum memory. The Sun Ultra 30, Ultra 60 or Enterprise with Solaris 2.6(SunOS 5.6) as operating system are recommended. The PCI DV board comes with system driver and camera configuration file. Since the camera configuration file works only under 64x64 discontinuous mode with binning disabled, this driver was modified to fit our special requirements at BBSO. Table 2.2 shows the PCI DV Specifications [49].

Table 2.2 Major PCI DV Specifications

PCI Bus Compliance	
Number of slots	1
Transfer size	1,4,and the highest valid burst size of 8,16,32 or 64 bytes.
DVMA master	yes
PCI Bus memory	32 bits
Clock rate	33MHz
Device Data Transfer	
Format	Programmable
Buffers	4KB FIFO for input
Software	Driver for Solaris 2.6+
Power	5V at 1.5A
Environmental	
Operating Temperature	10 to 40°C

In Table 2.2, the image frame grabbing speed has not been given since the frame grabbing speed depends on several undetermined factors, camera, and system settings, such as the size of the image grabbing buffer and image grabbing mode (continuous or discontinuous). For the correlation tracker used in BBSO, the actual image frame grabbing speed is about 1000-1700 frames/sec with CA-D10064T under 2x2 binning mode.

2.4.2.2 Image Board Driver and Configuration File The original PCI DV board did not have a specific driver for the Dalsa CA-D10064T. However, a very rough driver was made available, which runs at a relatively low speed (about 400frm/sec without binning). The upgrading to the latest firmware has updated the program in the field-programmable gate array that implements the PCI interface through a 32 bits flush ROM data register. Subsequent modification to the CCD camera configuration file to continuous mode has led to the frame grabbing speed of around 900frm/sec without binning and up to 1700frm/sec with a 2x2 binning.

The PCI DV configuration files are saved to the camera_config subdirectory. Each file stores configuration information for a specific camera model. This information is used by the initialization program (initcam), the device driver, the C libraries, and the application. During the test procedure, several Dalsa0064 configuration files have been built. The parameters of depth, height, width, frame_delay, method_flushdma, serial_timeout and continuous have been changed to fit to our Dalsa CA-D10064T camera. To perform continuous data transfer, ring buffers have been enabled by setting the edt_configure_ring_buffer parameter in the camera configuration file. Even so, the driver still occasionally crashes the system under some circumstances, especially high speed image grabbing. This problem has been reported to EDT and the cause is still under investigation.

2.4.2.3 Programming Interface There are two program libraries that come with the PCI DV board, Digital Video Library and DMA library. The PCI DV digital video library provides a high-level programming interface to the PCI DV, which handles the necessary bookkeeping, error recovery, camera shutter trigger, timing tasks and thread control. This interface is recommended by EDT and works well in the BBSO correlation tracker. Somehow, the digital video library and the PCI DV driver do not provide thread control correctly to Research Systems Inc.'s image processing package IDL, which means the IDL cannot be used properly when PCI DV board is running because the PCI DV driver and software library use thread control. This is unfortunate since IDL provides very strong image processing tools and most solar physics researchers use it. Another library, i.e., DMA library, is a lower-level interface that is called by the digital video library to perform the actual data transfer. For some unknown reason, the DMA library calls could not work well by using direct calling under our correlation tracker.

2.5 Sun Ultra-30 Workstation

Sun™ is the first company to implement the PCI I/O bus specification in a multiple-channel 64-bit, 66MHz configuration, which not only improves I/O throughput but also delivers the performance necessary for high-speed video and other real-time applications. Its 66MHz PCI bus and 1.6GB/sec Ultra Port Architecture (UPA) are the most significant reasons why the Sun's Ultra-30 has been chosen as our mainframe processor. The main architecture of Ultra-30 is shown in Table 2.3 [50].

Table 2.3 Main Technical Parameters of Ultra-30

Processor	Speed/Model/Cache	300 MHz UltraSPARCII, 2MB
	integer benchmark	12.1 (SPECint95)
	floating point benchmark	18.3 (SPECfp95)
Memory	Size	2048 MB
	Throughput	1.6GB/sec
I/O	Expansion Slots	1 64-bit 66 MHz PCI 3 64/32-bit 33MHz PCI
	Throughput	200 MB/sec
	Graphic Slots	2 UPA Slot, 100MHz
	Graphic Throughput	800 MB/sec per port
Graphics	Top system	Elite3D m6
	2D benchmark	4.3 million 2D vectors/sec
	3D benchmark	130 CDRS-03

Because only PCI cards that have Solaris support can work with Sun's new PCI systems, Sun works with selected vendors to verify that their PCI products are ready for Sun customers. EDT Company is one of the certified vendors to develop the image board driver for Solaris. The test report from Sun for PCI DV is shown in Table 2.4 [51].

Table 2.4 Test Report for PCI DV from Sun

Card Name: PCI DV

Product Type: Camera Interface

Vendor Name: Engineering Design Team

Description: This board provides high-resolution image capture for digital video cameras.

FCode Firmware on board NO

Energy Star Compatible NO

Basic Tests per Platform / Solaris Revision(s) (See Note A)

Venue:	Sun I/O Testing lab
Driver packages tests with:	(EDTpci11w EDT DR11 Parallel interface Driver (sparc) pci11w release 1.1)
1. **Workstation (Ultra30)**:	2.5.1 HW497 TESTED
2. **Desktop Server (Ultra-E450)**:	2.5.1 HW497 TESTED
3. **Enterprise Server (E3000)**:	2.5.1 HW497 NOT TESTED
4. **Workstation (Ultra5 & Ultra10)**:	2.5.1 HW497 NOT TESTED
5. **UltraAX in standard PC box**:	2.5.1 HW497 NOT TESTED
Results:	NO ERROR observed; Verified Basic and functional tests PASSED.

Product Test Notes/Warnings: NONE

NOTE A: Basic Tests include:

1. pkgadd/pkgrm
2. Boot verification (The system boots Unix with card installed)
3. PCI 2.1 compliance (Tests PCI hardware interface)

2.6 D/A Converter

The D/A converter performs digital signal to analog signal transformation. The calculated error signal is sent to D/A board and then converted into an analog signal to control the agile mirror. The D/A board in BBSO's correlation tracker is a NuDAQ PCI 6208V Multi-channel Analog Output Board from ADLink Technology Inc. The PCI-6208V is a high-density analog output card with 8 identical voltage output channels. This device employs ultra-stable nichrome (NiCr) thin-film resistors to provide monotonicity, low distortion, and low differential linearity error over long periods of time. The PCI-6208V uses a 32-bit PCI Bus with 16-bit resolution voltage outputs. Its output range is ±10V(14-bit resolution guarantee). The voltage setting time (-10V~+10V) is about 2μs. The major specifications of PCI-6208V are listed in Table 2.5 [52].

Table 2.5 Specifications of PCI-6208V

Number of channels	8
Converter	B.B. PCM56U
Conversion type	Monolithic multiplying
Resolution	16-bit (14-bit guarantee)
Voltage output range	±10V
Voltage output driving	±5mA max
Setting time	2μ second
Gain error	±0.2% (max, without trimming)
Connector	37-pin D-sub connector(female)
Bus interface	32-bit slave PCI bus

Since the PCI-6208V is initially designed for plug & play in Windows 95/98, there is no device driver available for Sun's Solaris from ADLink. The National Solar Observatory at Sunspot developed a special device driver for PCI-6208V under Solaris. With their approval, the Sunspot's device driver has been installed at BBSO and it is working properly.

Due to the agile mirror's frequency response being non-linear when the frequency is between 100-300Hz, a Bessel filter has been used to correct the mirror frequency response. The frequency response and Bessel filter are shown in Figures 2.7 and 2.8 respectively. This Bessel filter was built at BBSO by Owen Phairis. After correction, the response is shown in Figure 2.9.

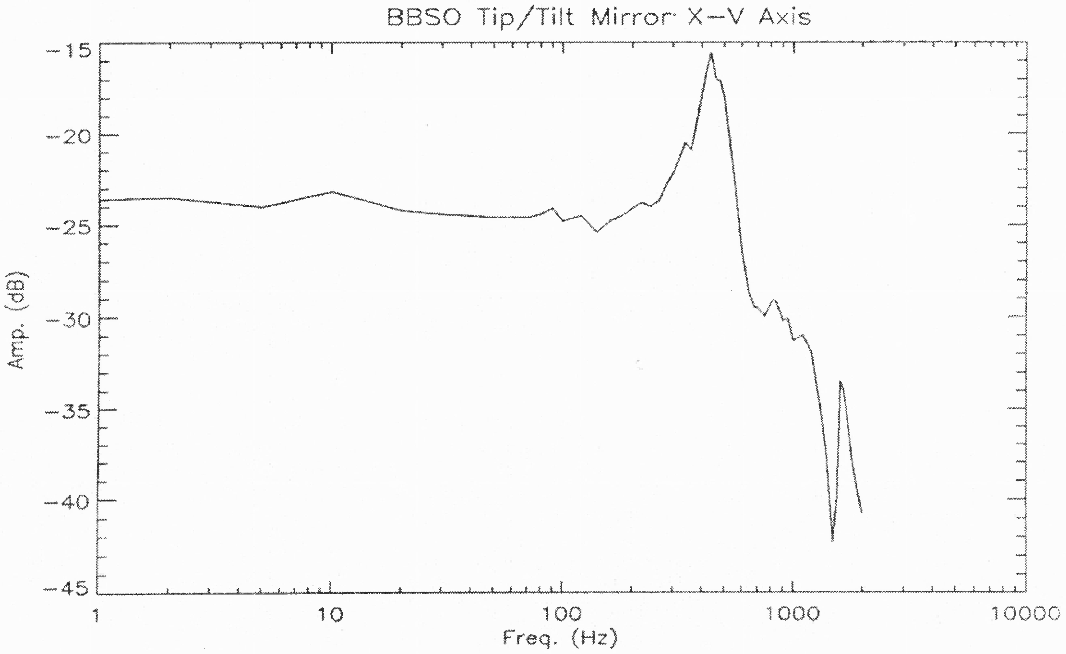

Figure 2.7 Agile mirror frequency response.

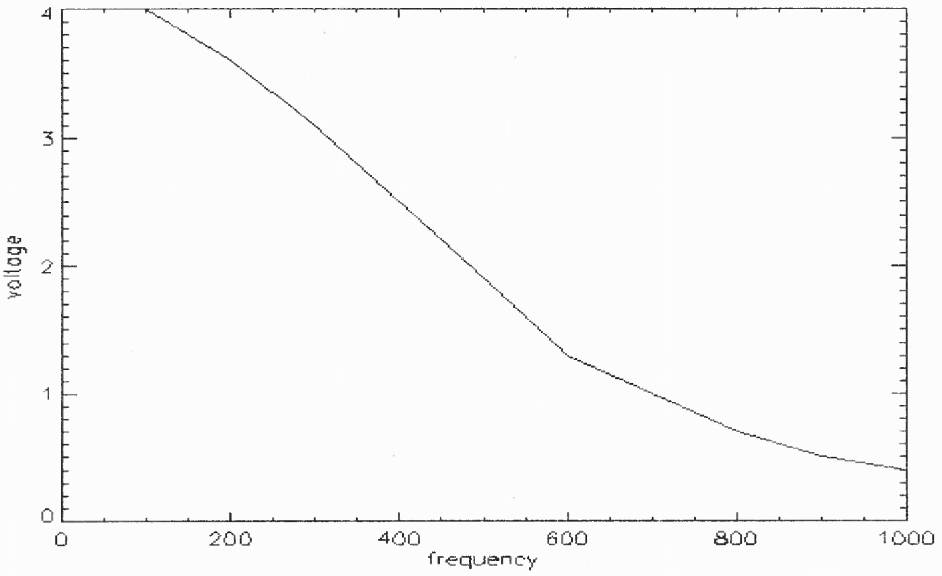

Figure 2.8 Bessel filter (low pass).

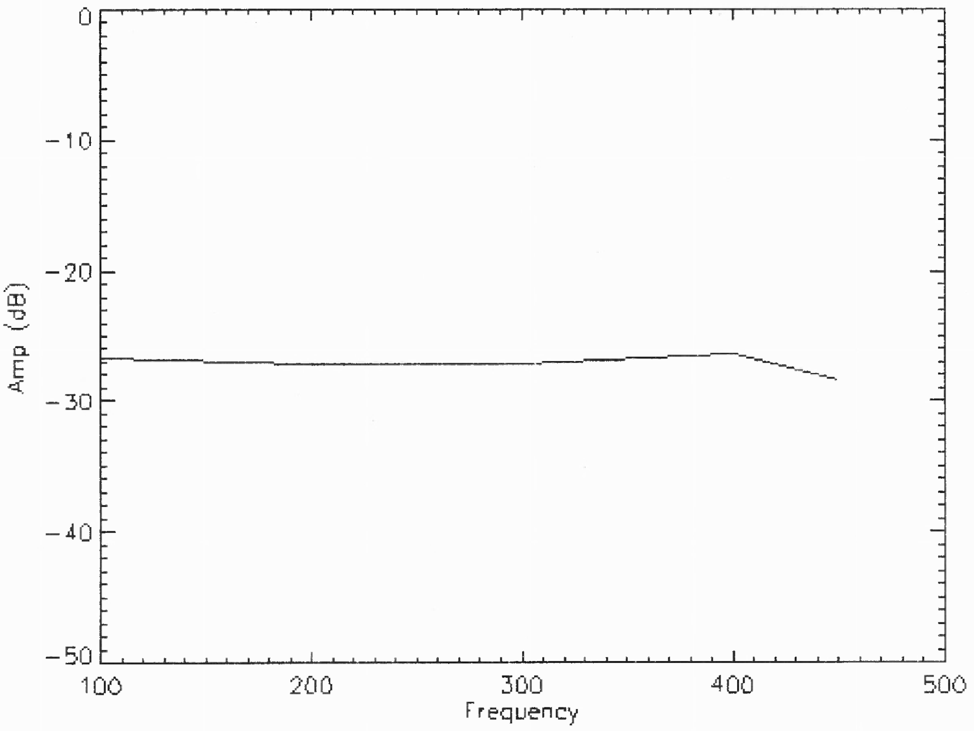

Figure 2.9 Corrected Frequency Response.

2.7 Software Development

2.7.1 Software Development Environment

Since the BBSO correlation tracker is a Sun Ultra-30 based, software-realized fast image tracking system, the software development plays a key role in the entire system.The BBSO Correlation Tracker is developed under the Solaris 2.6 operating system using C programming language. The software uses the library functions provided by EDT Inc. and Motif Graphical User Interface functions, which come with the X window system that are packaged with the Solaris 2.6.

The software can be divided into three parts, an image grabbing program that runs in the background, an image monitoring program that displays the live image and runs in the foreground, and a memory sharing subroutine that provide a common shared memory area used to fulfill the communication between the background software and foreground software. The reference image updating is accomplished by using a thread control and the updating method can be easily modified without rewriting other program parts.

2.7.2 Image Grabbing Program

The Image Grabbing Program performs all the key processes in the BBSO Correlation Tracker and has been given the highest priority, which includes all the hardware controls and error signal calculations. Its flowchart is shown in Figure 2.10.

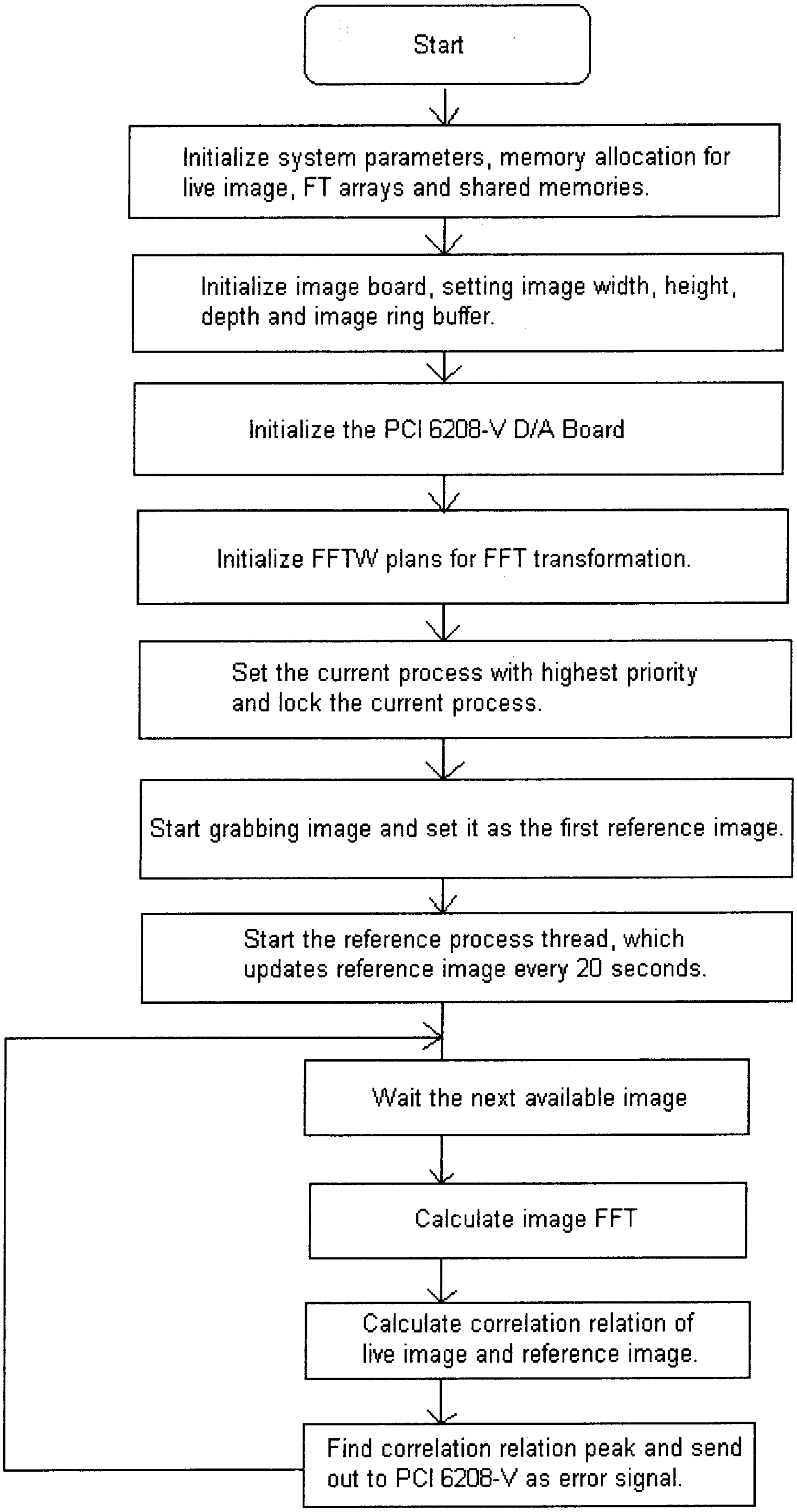

Figure 2.10 Image grabbing program.

The main purpose of image grabbing program is to grab live images from PCI DV board, perform FFT transformation, calculate the image shift and send error signal to the D/A board. This program is given the highest priority and runs in the background to obtain the maximum image processing speed. It is the key to the complete BBSO Correlation tracker system.

The image grabbing procedures are mainly based on three EDT system functions, pdv_open(), pdv_start_images() and pdv_wait_image(). The pdv_open() initializes PCI DV board and returns a device pointer. The pdv_start_images() uses the above device pointer to take the live image from image ring buffer and pdv_wait_image() returns the next available image buffer address. By using pdv_start_images() and pdv_wait_image() in proper order, the program can perform image processing while waiting for the next available image, and therefore, increase the system processing speed.

Reference updating is a separate task which is performed asynchronously to the main tracker task. This reference updating procedure is done in parallel by using another thread. When doing image alignment offline, the usual method is to chose the best reference image by calculating the image contrast. In the correlation tracker system, since complicated image calculation in updating reference image would reduce system's throughout, the reference image updating is accomplished every 20 seconds without any image calculation.

The FFT subroutine used in this program is FFTW developed at MIT by Matteo Frigo and Steven G.Johnson. FFTW is a free C subroutine library for computing the Discrete Fourier Transform in one or more dimensions, of both real and complex data.

The FFTW's performance is typically superior to most publicly available FFT software. The FFTW can be downloaded from http://www.fftw.org.

The FFTW uses "plan" to process the FFT. A "plan" is a pre-initialized data array which will hold the FFT data. By using the pre-initialized "plan", the FFT calculation is faster than others. In our tracker program, two 2-D plans have been established for forward and backward Fourier Transform. Due to the CA-D10064T camera's extra bits in its image output (79x64 actual resolution), in the binning mode, the image size is 40x32, and the FFT subarea is chosen as 26x26. Though this is not a power of 2, there is no big difference observed between a 26x26 image and a 16x16 image (which is used in National Solar Observatory at Sunspot). The reason is that the real slowdown in the program results from image grabbing process, i.e., the pdv_wait_image().

The overall performance of the program is listed in Table 2.6.

Table 2.6 Time Exhausting Distributions

Total loop time	920μs
Forward Fourier Transform	225μs
Complex product computation	275μs
Backward Fourier Transform	215μs
Find the correlation peak	28μs
Send error signal to D/A	12μs

The total image processing speed is around 1100 frames/sec in 2x2 binning mode with a FFT subarea of 26x26 pixels.

2.7.3 Image Monitoring Program

The image-monitoring program is the graphical user interface of the BBSO correlation tracker. It provides the user a tool to communicate with the tracker program. The image-monitoring program is accomplished with C programming language and Motif, X-Window GUI functions. The interface consists of eight major buttons and their call back functions. Since X Window programming uses multi-thread, event driven techniques, the program runs under a loop and each function is fulfilled by its corresponding call back function. The main object of the program is to display real time images taken from the shared memory, control image brightness and image size, and turn the tracker on or off.

The communication between this program and the image grabbing program is fulfilled by using the shared memory created by the latter program. Through the shared memory, the grabbed images and tracker control parameters are exchanged. The flowchart of the image-monitoring program is shown in Figure 2.11.

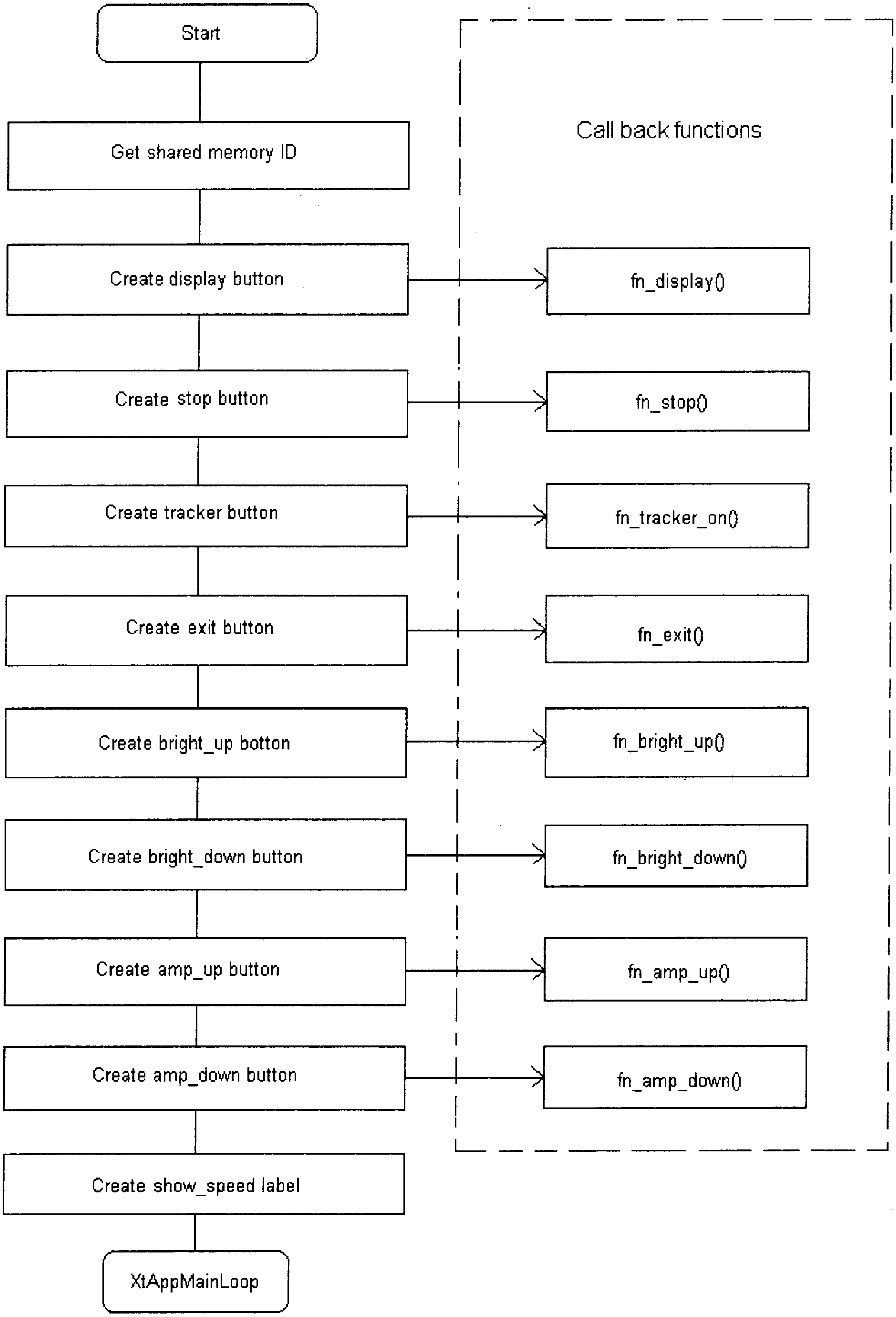

Figure 2.11 Image monitoring program.

The Call back functions used in image monitoring are described as follows,

fn_display(), uses current screen depth, amp and brightness to display the images taken from the shared memory. The parameters amp and brightness are determinted by fn_amp_up() or fn_amp_down() and fn_bright_up() or fn_bright_down(), which determine the image brightness and image size diplayed on the system monitor. The X Window function XputImage() is used to display the image.

fn_stop(), stops displaying the live image to increase the image processing speed.

fn_tracker_on(), this function performs as a switch to turn on the tracker or turn off the tracker.

fn_exit(), terminates program and return to operating system.

fn_bright_up() and fn_bright_down(), controls the image brightness displayed on the system monitor.

fn_amp_up() and fn_amp_down(), adjusts the image size diplayed on the system monitor.

The show_speed_label() is used to monitor the image processing speed.

2.8 Results

The initial results of the BBSO correlation tracker are shown in Figure 2.12. All the tests are carried out by Leonid Didkovsky at BBSO.

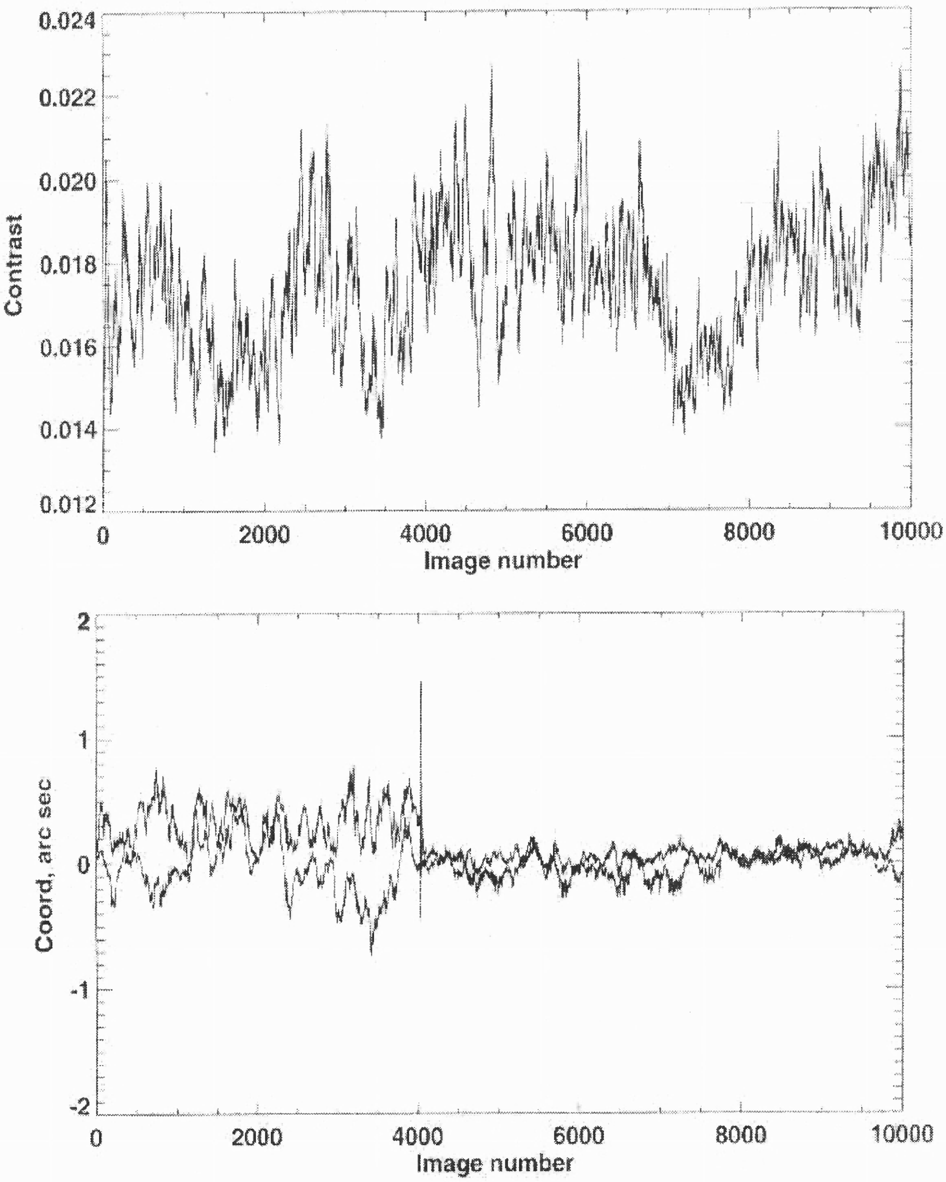

Figure 2.12 Correlation Tracker results. (from Leonid Didkovsky at BBSO).

In Figure 2.12, the top one shows the image contrast changes and the bottom one shows the image shift changes when correlation tracker turns on and off. Though the image contrast did not change much, a very significant decrease in image shaking has been observed. The image shift is reduced from 0.7 arc sec maximum to 0.2 arc sec maximum, which means the new correlation tracker system has achieved the same performance as the FFT hardware based correlation tracker [14]. The rms of average image shift has been decreased from 0.415 to 0.097 arc sec. This result has shown that the correlation tracker based on Sun Ultra-30 works very effectively to reduce image shaking.

Figure 2.13 shows the images obtained when the correlation tracker is on and off. The image was integrated by using 5000 images. The contrasts are 1.18 and 1.64 respectively. A total increase of 39% has been achieved.

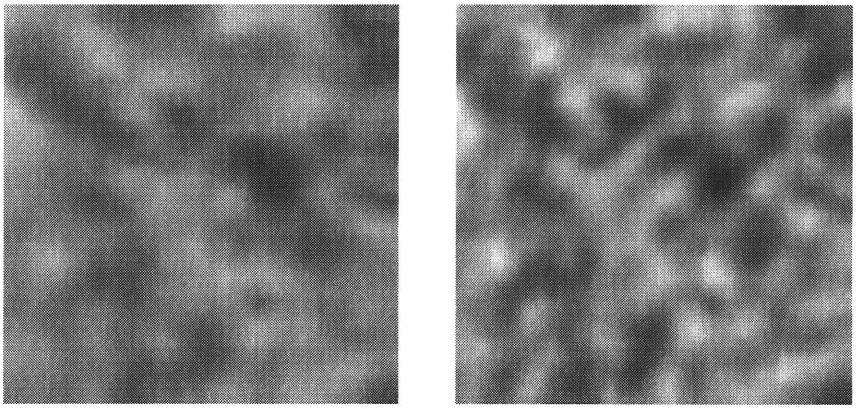

Figure 2.13 Image comparison with CT off (left) and on (right) (from Leonid Didkovsky at BBSO).

From the above results, the correlation tracker based on a Sun Ultra-30 workstation has been proved to work very well in reducing the image shift. Compared to the existing correlation tracker system, the advantage of the new system is quite obvious, simple, stable and easy to use. The complex image processing hardware is no longer needed in the new system. Also, since the whole system is based on the software development under Solaris operating system, it is easier to maintain and update. The real-time processed images can be easily dumped to some external storage media for later digital image processing. Since the agile mirror feeds the entire optical path of 26” telescope, other benches and cameras benefit from the improved stability.

CHAPTER 3

THE DIGITAL MAGNETOGRAPH SYSTEM

The second system built at BBSO for this Ph.D project is a new digital magnetograph system. The system uses part of BBSO's existing video magnetograph (VMG) system: a quarter wave plate, a Ferro-electric liquid crystal to switch polarizations and a new 256x256 pixels, 12-bit Dalsa area scan camera, which is used as the detector and as the driver to switch the liquid crystal. The maximum data transfer rate of the system is 100 frames per second. The camera is interfaced to a Sun Ultra-30 workstation with an EDT PCI DV imaging board for data acquisition. The computer has 128Mbyte of RAM and up to 1000 live images can be stored in memory once for quick post-exposure image processing. The new magnetograph system has significantly improved the sensitivity and spatial resolution over the old BBSO VMG system. In particular: (1) new digital image data are 12 bits deep while the video signal is digitized as 8 bits. Polarizations weaker than 1% cannot be detected by a single pair subtraction in the video system. The digital system can detect a polarization signal of about 0.3% by a single pair subtraction. (2) The data rate of the digital system is 100 frames per second, and that of the video system is 30 frames per second. So the time difference between two polarizations is reduced in the new system. Under good seeing conditions, the data rate of 100 frames per second ensures that most of the wave front distortions are 'frozen' and the conditions in the left and right-handed circular polarized image pairs are stable. (3) Magnetograms are constructed after image selection and alignment to enhance the image quality. (4) A method for stray light correction has been used to enhance the magnetograph's signal-to-noise ratio. One disadvantage of the faster system is that, since a larger field of view camera would reduce the image grabbing speed, the 256x256 camera provides a smaller field of view than the VMG system

3.1 Hardware Description

The video magnetograph (VMG) system at Big Bear Solar Observatory was first invented by Leighton (Mosher, 1976) and has been improved throughout the years. Although detectors and the imaging system have been changed over time, the basic setup remains the same. Although BBSO often provides the most sensitive magnetographs, as evidenced by a study of intranetwork fields [40], it suffers from some obvious limitations. The most obvious shortcoming is the detector system – an analog video camera. The frame rate of the camera is 30 frames per second, i.e., images representing two polarized signals are taken 1/30 second apart. Two images may be shifted with respect to each other due to atmospheric seeing or guiding fluctuations. Blurring and differential image motion will introduce additional distortions between consecutive images. Furthermore, the video signal is digitized only to 8 bits which leads to saturation of strong signals.

The new digital magnetograph system is composed of a 256x256 CA-D1-256T Dalsa camera which is used to obtain a larger field of view than the 64x64 0064T used in Correlation Tracker, an EDT PCI DV image grabbing board and a Sun's Ultra-30 workstation operated under Solaris 2.6 operating system. The description of the system is shown in Figure 3.1.

The new CCD camera works with EDT PCI DV imaging board and can take 12-bit images at 100 frames per second speed. The time difference between two polarized signals is about 5 ms with an exposure time of 5 ms. Since the image grabbing speed is much higher than that in the VMG system, the whole digital system can provide much more stable images than the old system.

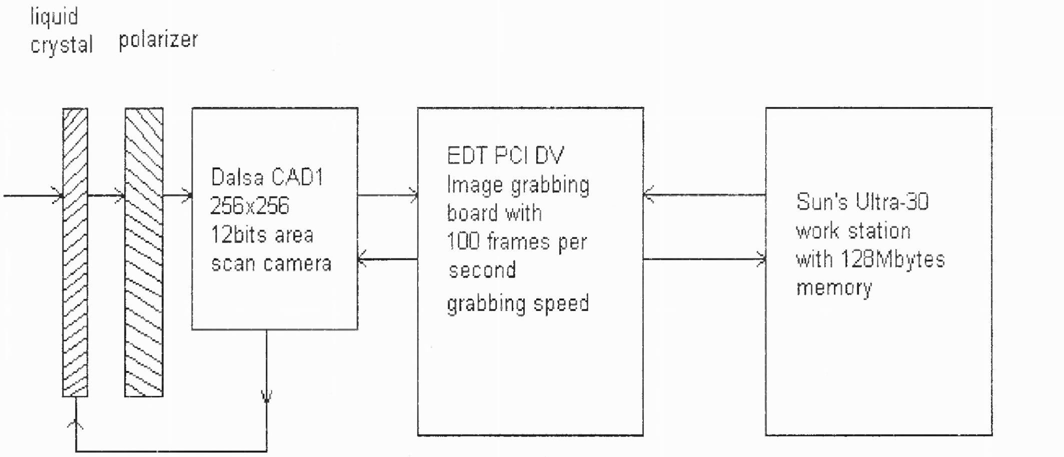

Figure 3.1 Digital solar magnetograph system at BBSO.

To utilize the high frame grabbing speed, the grabbed images are stored in the RAM first and then dumped to the hard disk. Since the Ultra-30 is equipped with 128Mb RAM, one sequence of 1000 frames can be stored in the memory at once. The total number of sequences that can be stored in the hard disk is determined only by the hard disk capacity itself. By using this system, 67 sequences of 1000 frames of images have been grabbed, which take about 1 hour and 27 minutes, and the total stored images size is about 8 GByte. These images will be used in the following chapters to perform image processing.

3.2 Software Description

The system software is developed by using the C programming language and Motif graphical user interface under the Solaris 2.6 operating system. The main tasks of the program are divided into two parts: hardware control and live image display and storage. Using system subroutines provided by EDT, the image frame buffer size, camera shutter speed and exposure time can be easily controlled. The whole system runs in a big loop, in each loop, 1000 images will be grabbed once (depending on memory size) and then dumped into the hard drive. After a time interval between two image series, a new loop begins and another series of images will be grabbed and stored. A filename generation subroutine produces the image storing file name according to current date and time. Then, different series of images will be stored in different files with a date and time stamp on it. The live-image-display routine accomplishes the tasks that display the live image on the display device. The image display can be adjusted by two variables: image size and brightness. In the present system, the maximum stable working speed for image grabbing is about 100 frames per second and the maximum number of images that can be grabbed at once (temporarily stored in system memory) are 1000 frames.

The software working flowchart is shown in Figure 3.2. The software works in a big XtAppMainLoop, which is a standard function in the X Window system. Each callback function provides a subroutine that will be called by the correspondent push button in the XtAppMainLoop. Since the software is organized in a highly modularized way, it is very easy to maintain and update the system software. Any new functions added to the system will be relatively independent of all the existing modules and will be added to the callback list.

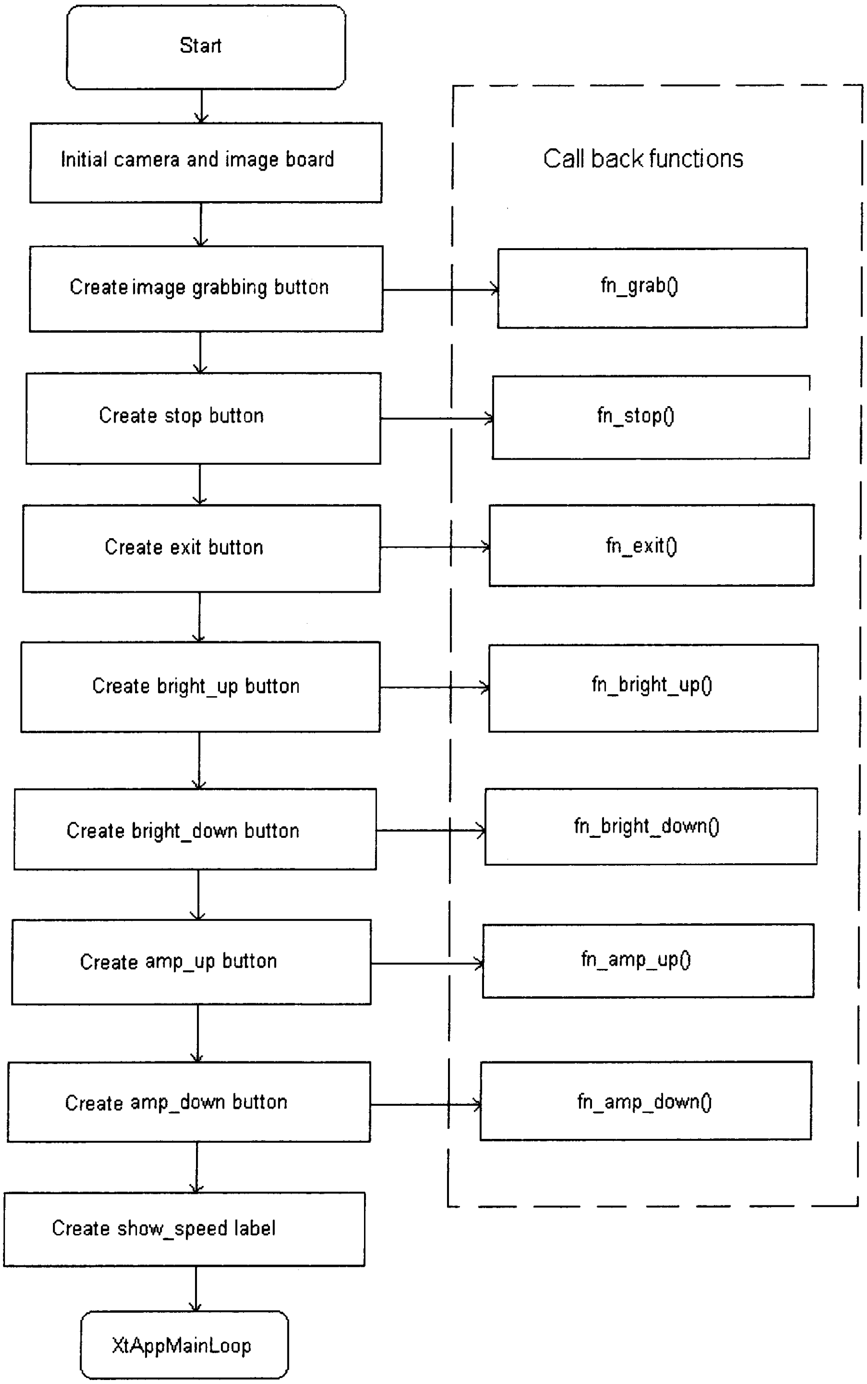

Figure 3.2 The flowchart of the mainframe of solar magnetograph system software.

Among all the Callback functions, the most important one is the fn_grab(), which performs image grabbing, displaying and image storing. The flowchart of fn_grab() is shown in Figure 3.3.

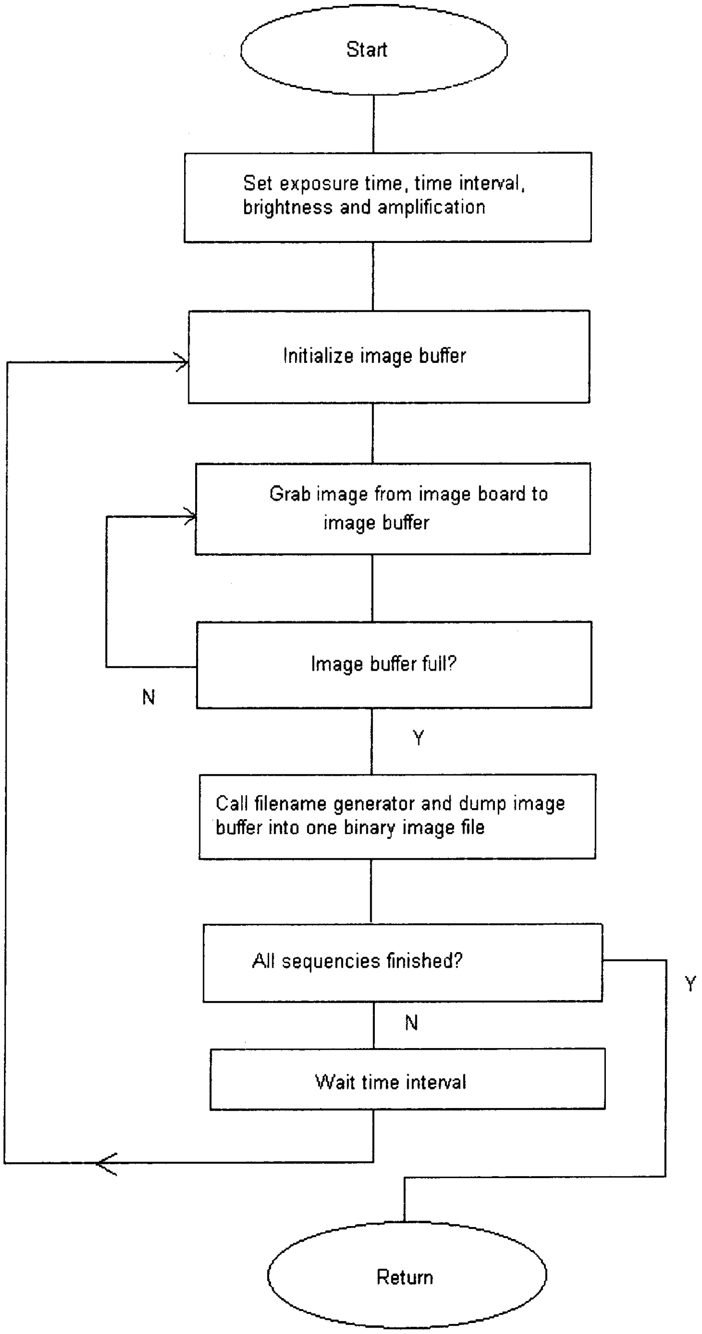

Figure 3.3 The flowchart of fn_grab( ).

3.3 Conclusions

To obtain the high-resolution solar magnetograph, a new digital magnetograph system has been built in Big Bear Solar Observatory. The new digital magneto system has significantly improved the sensitivity and spatial resolution over the old BBSO VMG system. The new digital image system has a 12-bits data depth and can detect a polarization signal of about 0.3% by a single pair subtraction compared to that of the old VMG - 1% [8]. Also, since frame rate has been increased from 30 frames per second to 100 frames per second, under good seeing, most of the wavefront distortions are frozen and clearer images can be obtained.

The discussions in the following chapters are based on the images grabbed by using the above digital magnetograph system. A total number of 64000 images are used in different methods discussed below. The total images are stored in 64 image files and each image file contains 1000 images. The total time interval for image grabbing is about 1 hour and 27 minutes without any time interval between image sequences. Each image has a field of view of 210 arcseconds with a image resolution of 210/256=0.82 arc seconds per pixel. The image location is near the disk center, at 25E160N. All the images are taken in 256x256 pixels with an exposure time of 5ms.

CHAPTER 4

IMAGE AVERAGING

4.1. Image Averaging Principle

For most digital images, the white noise that is randomly distributed over the frequency domain is inevitable. To raise the S/N ratio, the traditional way is to use averaging method and that is still the most effective way to reduce the random noise. In addition to averaging, image selection also plays an important role in our experiments.

Consider a noisy image $g(x,y)$ formed by the addition of noise $\eta(x,y)$ to an original image $f(x,y)$; that is,

$$g(x,y)=f(x,y)+\eta(x,y), \tag{4.1}$$

where the assumption is that at every pair of coordinates (x,y), the noise is uncorrelated and has zero average value. The objective of the following procedure is to reduce the noise effects by averaging a set of noisy images.

If the noise satisfies the constraints just stated, it is a simple problem to show that if an image $\overline{g}(x,y)$ is formed by averaging M different noisy images of the true brightness distribution $f(x,y)$,

$$\overline{g}(x,y)=\frac{1}{M}\sum_{i=1}^{M} g_i(x,y), \tag{4.2}$$

then it follows that

$$E\{\overline{g}(x,y)\}=f(x,y), \tag{4.3}$$

and

$$\sigma^2_{\overline{g}(x,y)}=\frac{1}{M}\sigma^2_{\eta(x,y)}, \tag{4.4}$$

where $E\{\bar{g}(x,y)\}$ is the expected value of $\bar{g}(x,y)$, and $\sigma^2_{\bar{g}(x,y)}$ and $\sigma^2_{\eta(x,y)}$ are the variance of $\bar{g}(x,y)$ and η, all at coordinates (x,y). The standard deviation at any point in the average image is

$$\sigma_{\bar{g}(x,y)} = \frac{1}{\sqrt{M}} \sigma_{\eta(x,y)} . \tag{4.5}$$

Equations 4.4 and 4.5 indicate that, as M increases, the variability of the pixel values at each location (x,y) decreases. Because $E\{\bar{g}(x,y)\} = f(x,y)$, this condition means that $\bar{g}(x,y)$ approaches $f(x,y)$ as the number of noisy images used in the averaging process increases.

4.2 Dark Frames and Flat Field Frames

One of the major problems encountered when using astronomical images obtained from CCDs is the lack of flat fielding. Very often people have been forced to deal with images that have been pre-processed by someone else and yet still retain variations in the background value. To avoid such problems, the Flat Field and Dark Current have to be taken into consideration before any solar magnetograms are constructed.

The flat field frames used in the following analyses were obtained from a quiet Sun region near disk center while moving the telescope along both axes in the fast mode. The optical path was not altered during the flat fielding procedure. 1000 single frames (500 left- and right-handed circular polarized frames each) were averaged to obscure the granular pattern and to reduce white noise by a factor of 22.3. The temporal evolution of solar structures and the seeing variations can result in a blurred image with low contrast. This image is virtually free of high spatial frequency features so that low pass filtering of the images to avoid artificial polarization signals due to flat field artifacts is not necessary. The flat field for the setup during our experiment is shown in Figure 4.1

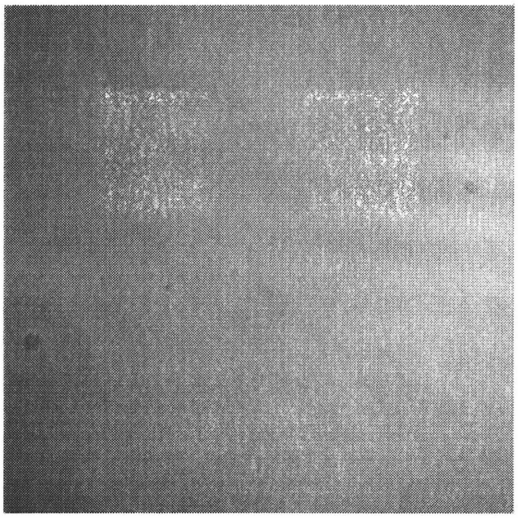

Figure 4.1 Flat field obtained from quiet Sun near disk center

The dark current is obtained by blocking the light to the CCD camera. Again, a total of 1000 dark frames were taken to reduce the white noise. In the following discussion, each image *i(x,y)* has been corrected by flat field *f(x,y)* and dark current *d(x,y)*,

$$i'(x,y) = \frac{i(x,y) - d(x,y)}{f(x,y)}.$$

4.3 Averaged Image Statistics

The averaged solar magnetograms are shown in Figure 4.2. Considering the image shift increases as the image number increases [8], all the image averaging has been done in one image series. From Figure 4.2, as the image number increases, the image becomes clear and more magnetic field details appear. But when the averaging number is sufficiently large (>300), the images remain nearly the same, which is shown in Figure 4.3.

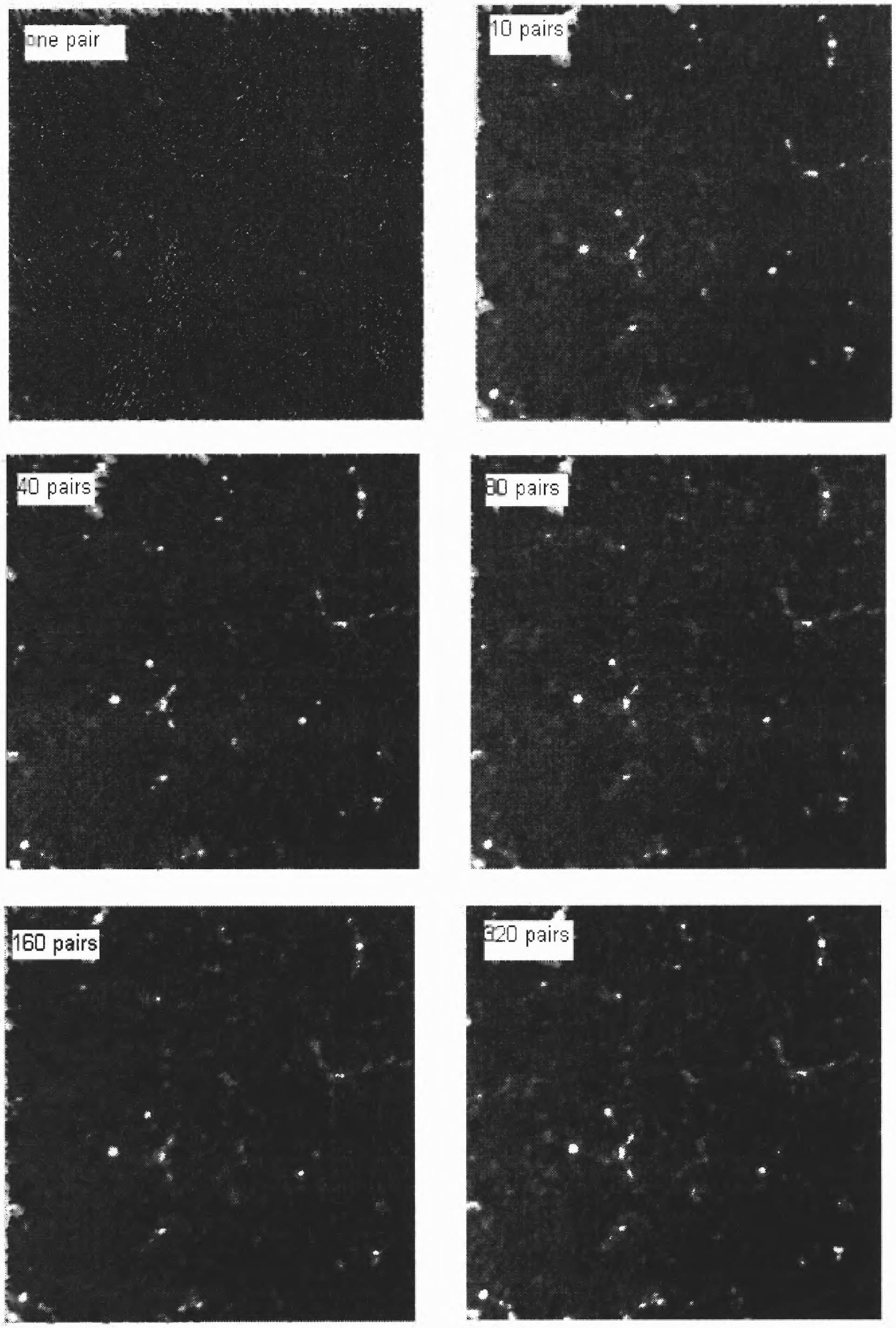

Figure 4.2 Magnetograms of one pair subtraction and 10, 40, 80, 160, 320 pairs of images.

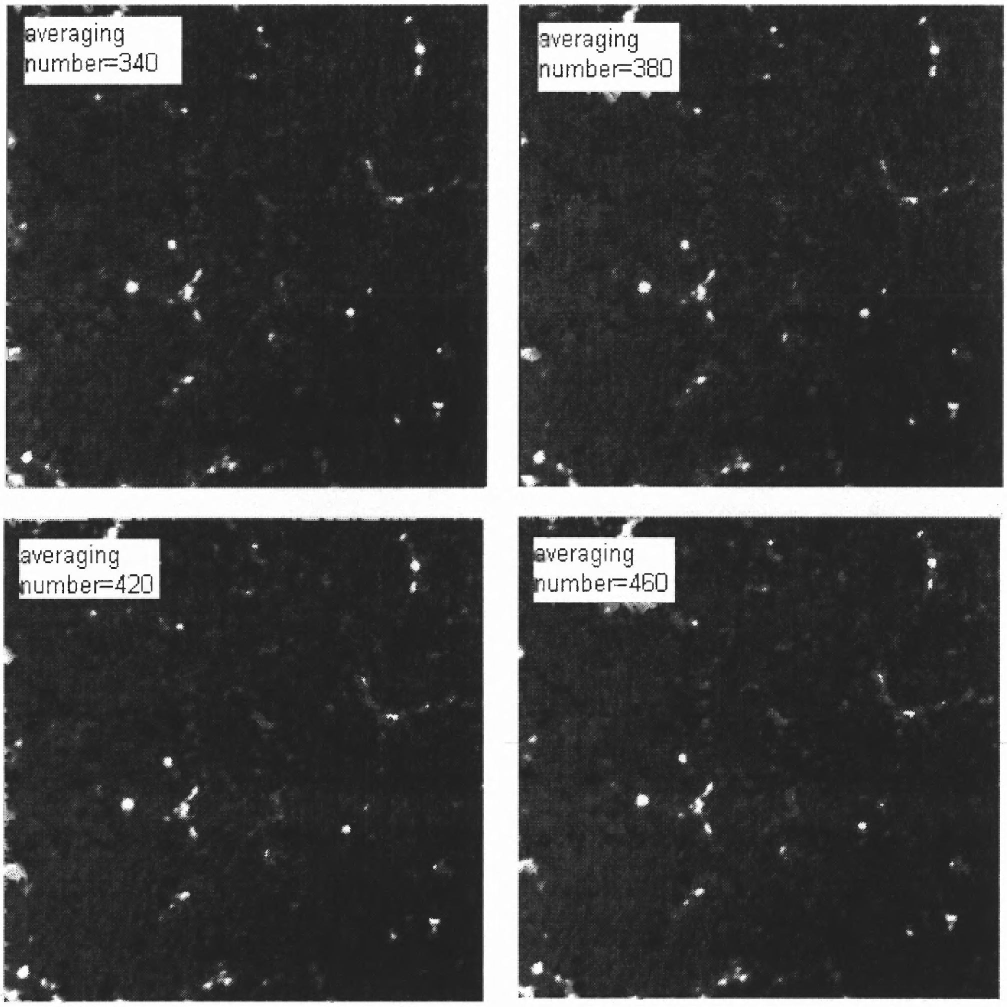

Figure 4.3 Averaged images show very small changes when averaging numbers are big enough.

From an ideal situation, the averaging number would be taken as large as possible. But considering the image analyzing efficiency and systematic effects, a threshold value must be determined that balances image improvements with time taken to produce image.

To analyze the noise reduction efficiency, first take a look at the graph of change in standard deviation with image number, which is shown in Figure 4.4.

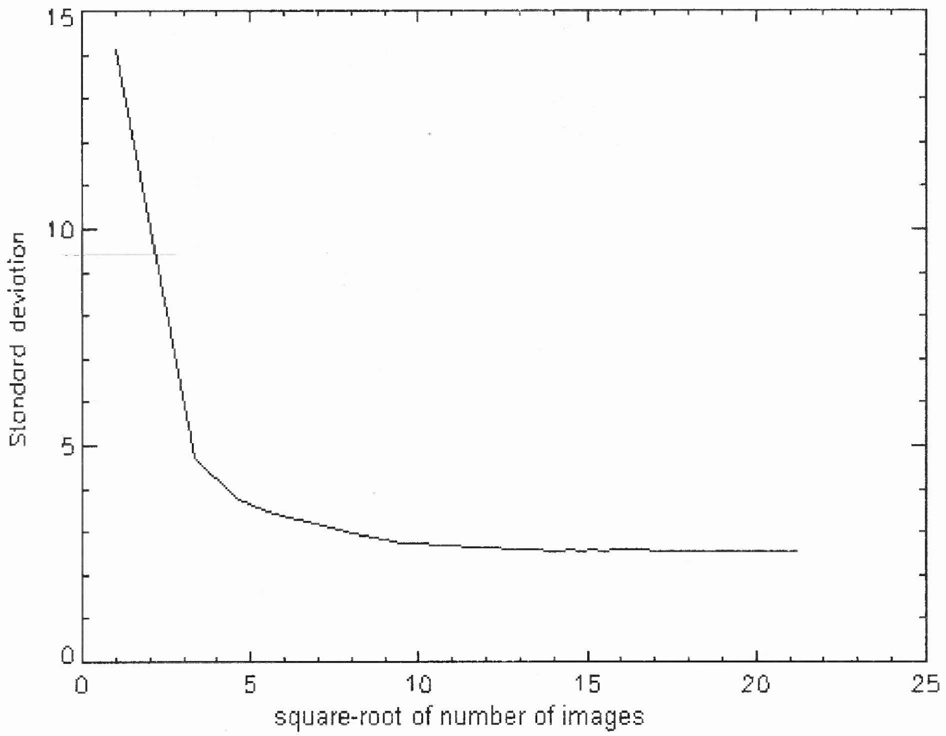

Figure 4.4 Standard deviation vs number of images averaged.

Since the magnetogram is strongly dominated by widely spread white noise, the standard deviation is very large for a single magnetogram. As the number of averaged images increases, the white noise decreases sharply at first, and then tends toward a constant when the number of averaged image increases. Looking at the histogram shown in Figure 4.5, as the number of averaged images increases, the histogram narrows, which just shows us the big difference between a heavily polluted magnetogram and a high S/N image. As in high S/N ratio image, different filters and methods have been developed to expand the histogram of the signal, which means a higher standard deviation is desirable and more details will be displayed. But in magnetogram, since the image contains both positive and negative values, a narrower histogram and a lower standard deviation reflect the lower noise, until the standard deviation becomes dominated by the properties of the true signal. At this point the curve becomes flat.

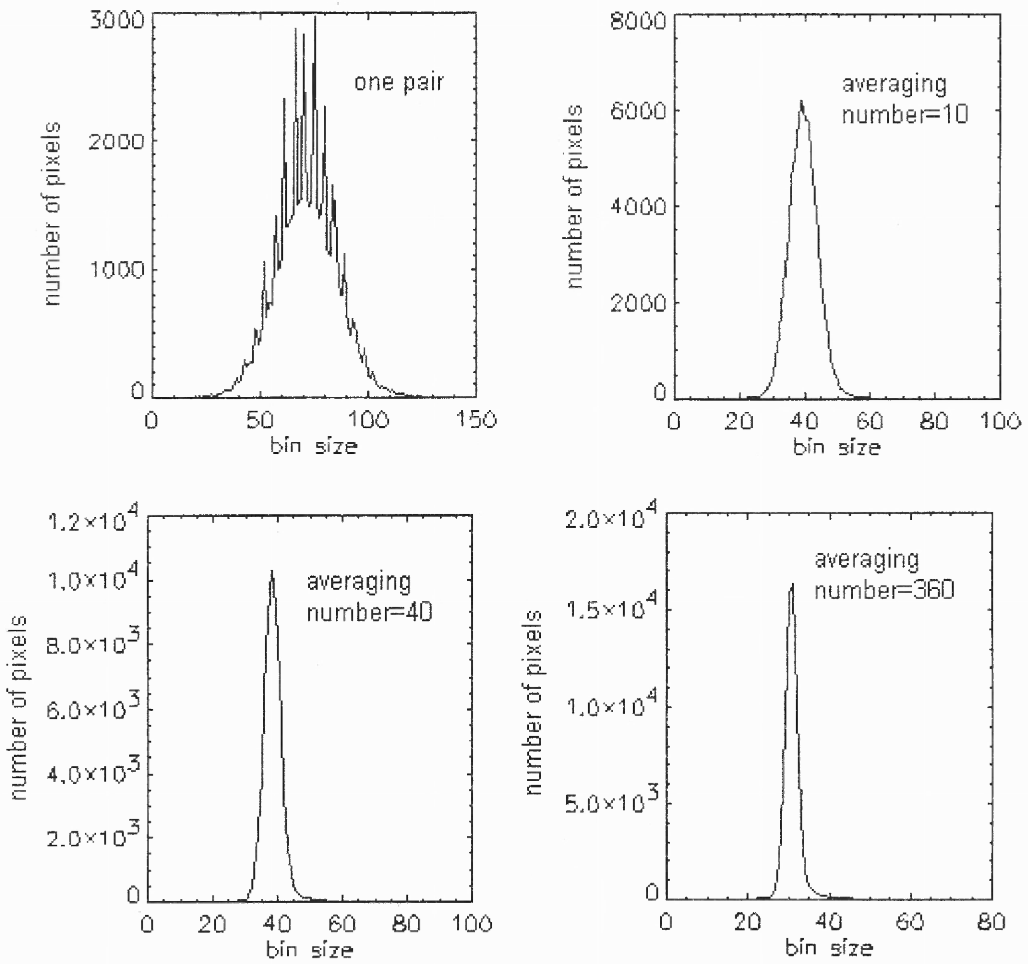

Figure 4.5 Histograms of images by using different averaging number.

The following is a theoretical analysis of the decrease in standard deviation with increase in number of averaged images. From the above discussion, the standard deviation will be reduced as the number of averaged images increases due to the noise reduction. The relationship between an image variance and the number of averaged images can be concluded as follows,

$$Variance = \frac{V_0}{M} + V_\infty , \tag{4.6}$$

where V_0 is the variance of a single image, M is the number of averaged images and V_∞ is the image variance of the original brightness distribution. This relationship tells us that when the image number increases, the white noise is reduced by square root of M. Meanwhile, the standard deviation also decreases by about $\sqrt{\frac{V_0}{M} + V_\infty}$.

To find the appropriate parameter to describe the white noise level, only second moment is not enough. The higher order of image moment must be taken into consideration. From digital image processing theory, the fourth image moment (Kurtosis) is very sensitive to noise [41] and can be used to describe the noise level [42]. Then the Kurtosis needs to be taken into consideration.

The image Kurtosis is defined by the following definition,

$$K = \frac{\mu_4}{\sigma^4} = \frac{E[X - E(X)]^4}{[E[X - E(X)]^2]^2} \text{ -3}, \tag{4.7}$$

where, μ_4 is the fourth moment and σ^4 is the fourth power of the standard deviation σ.

It is larger if the distribution has sizeable tails that extend much further from the mean E(X) than $\pm\sigma$.

Figure 4.6 shows the image Kurtosis as function of averaging image numbers.

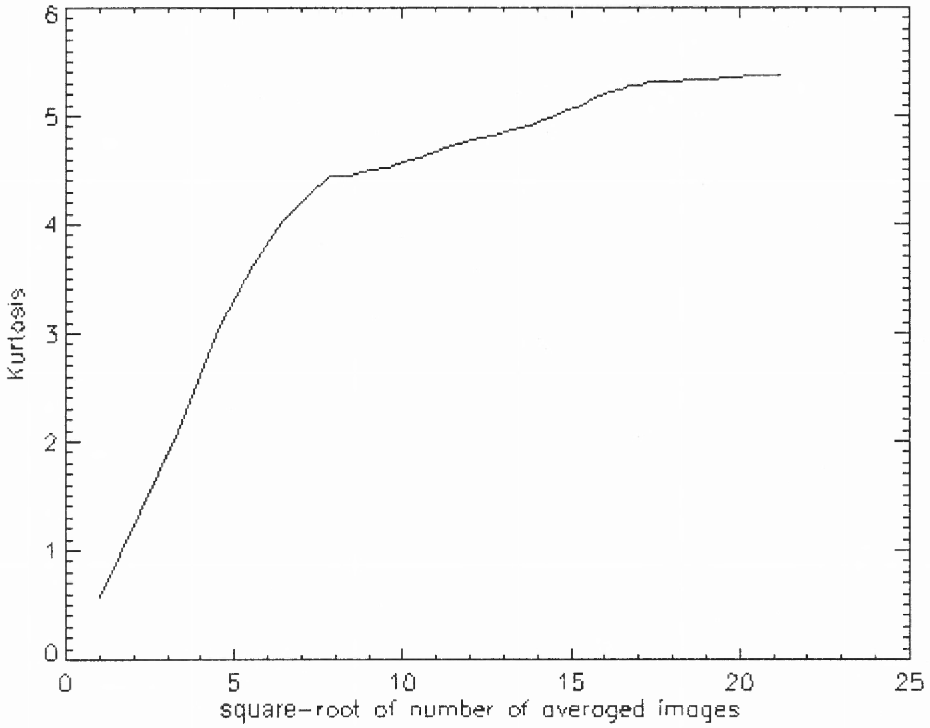

Figure 4.6 Kurtosis vs number of averaged images.

The evidence is very obvious that, with the number of averaged images increase, the image Kurtosis increases sharply at the beginning and then tends to saturate when averaging number tends to be very big. The whole idea behind this conclusion reminds us that in solar magnetogram, the Kurtosis can be considered as a very efficient parameter to evaluate the relative image signal to noise ratio and can be used to calculate the averaging image number that is enough to ensure the lower white noises. Since the kurtosis of averaged images is positive, the system's point spread function then will be considered as a gaussian function [43] and this will be discussed later in Chapter 8.

4.4 The Properties of White Noise in Solar Magnetogram

Since the Kurtosis can be effectively used as an important parameter in judging the white noise level in solar magnetogram, another problem is to investigate the extent to which the noise has true gaussian distribution.

Subtracting averaged image from non-averaged image. The difference is the undiminished white noise, which along with its histogram are shown in Figure 4.7. From the histogram, it can be seen that the noise is more widely spread than the averaged image histogram and has a same range of outline as the un-averaged magnetogram, which implies that the original magetogram is heavily dominated by the white noise.

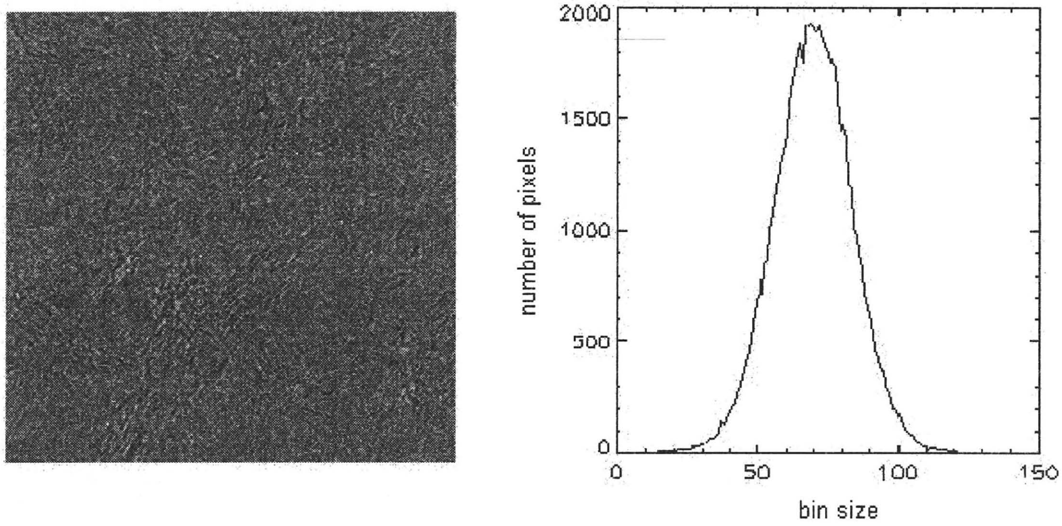

Figure 4.7 Eliminated noise and its histogram.

After performing a gaussian fitting, the diminished white noise has a perfect gaussian distribution given by the formula below,

$$f(x) = \frac{1}{\sqrt{2\pi}\sigma} \exp\left(-\frac{(x-x_0)^2}{2\sigma^2}\right),$$

where x denotes the pixel gray level and σ is the image standard deviation. In our case, x_0 is equal to 70 and σ is equal to 13.5, which is much bigger than that of the averaged magnetogram - 6.4. The result of gaussian fitting result is shown in Figure 4.8. The excellent fit shows that the noise remaining after signal subtraction is true gaussian noise.

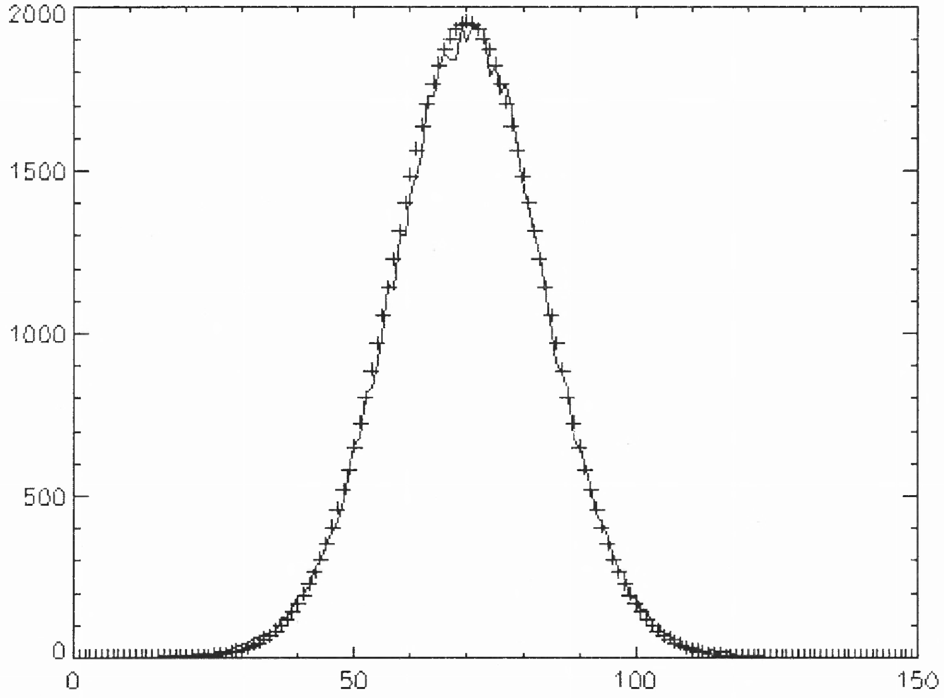

Figure 4.8 Gaussian fitting for white noise.

4.5 Fourier Spectrum Analysis

Figure 4.9 shows the logarithmic Fourier spectrum for an averaged image and a non-averaged image. The graph shows that the averaged image Fourier spectrum has been largely reduced in nearly every frequency except at very low frequencies, which again implies that a largely spread white noise has dominated the magnetogram before the image averaging. The result that the differences of Fourier spectra are more significant in higher frequency than at lower frequency tells us that the noise is bigger in the high frequency regime than in the low frequency regime. This gives us the hint that the diminished white noise has more influence on small-scale magnetic field than on large-scale magnetic fields. This leads to the result that without image averaging, the background noise is very big and it may totally conceal the fine magnetic structures. From Figure 4.2, the big difference in fine magnetic structure is obvious.

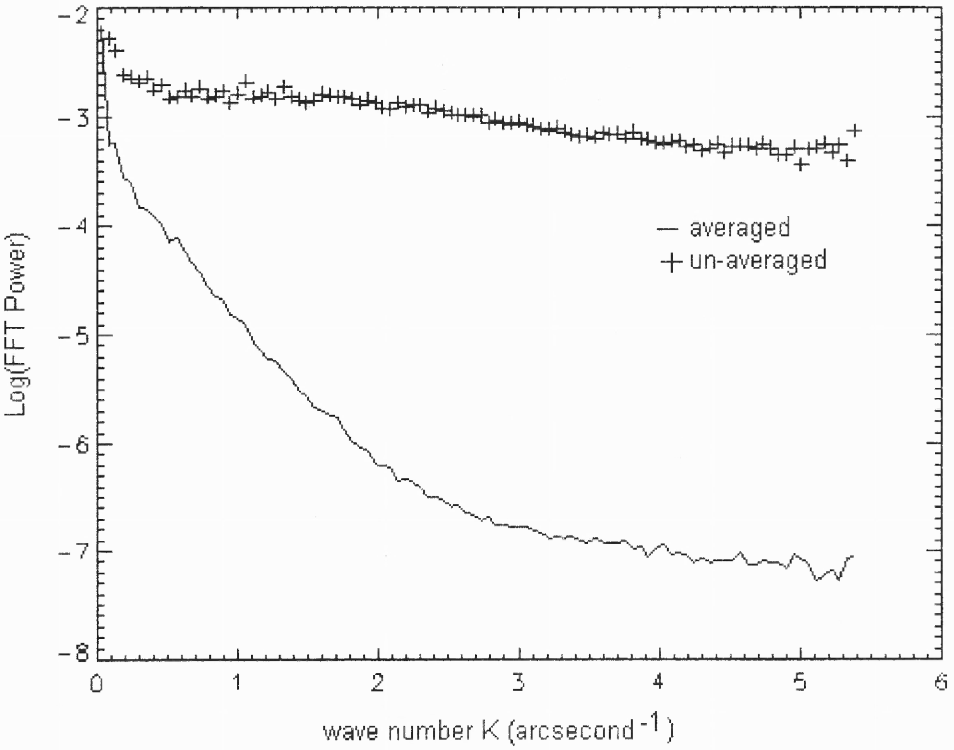

Figure 4.9 Fourier spectrum of averaged and non-averaged magnetogram.

4.6 Conclusions

Image averaging method is a very effective method to reduce the image white noise. The averaged solar magnetograph is clearer, its histogram is narrower and its Fourier spectrum is tending to be steeper in logarithmic graph. The eliminated noise by the image-averaging method has a perfect gaussian distribution. Due to the contribution made by the white noise, the image standard deviation is also reduced by $\sqrt{\frac{V_0}{M} + V_\infty}$ when averaging M images, which means the standard deviation is no longer appropriate to be taken as the noise reduction parameter. A higher order image moment Kurtosis can be used as the relative standard to calculate the image averaging efficiency. This standard has only been proved to be effective by performing the Gaussian distributed white noise reduction in solar magnetograms.

CHAPTER 5

IMAGE SELECTION

5.1 Image Selection Method

In the previous section, the Kurtosis has been discussed and it has been shown that it can be taken as a standard to calculate the effective averaging number when processing the solar magnetogram. It is not necessary to use all the images for the image averaging process. Since the range of image shifts increases as the number of averaged images increases [8], reducing the number of averaged images not only enhances the image processing efficiency but also reduces some image shifts by only considering some best images. From Figure 4.6, since the Kurtosis changes very slowly above 300 frames, it allows us to only select the best 300 pairs of images to perfom the image averaging. Because all the images before image averaging have the same order of white noise, the standard deviation will still be used as the standard for judging the 'best' images. Due to the complexity of solar magnetograms, i.e., all the even images have one polarization and all the odd images have the other polarization, the image selection process has to ensure that the order of even and odd images should be the same as that before the image selection.

There are two ways to select the 300 pair of best images while keeping the odd-even order unchanged. One way is to select 300 best even images and then following odd images as the 300 best pair, and the other method is to calculate average standard deviation of each pair of images first and then select the best 300 pair of images. By taking a comparing test of the two methods, the latter one has been chosen as our image selection method since it has a slightly better result in calculated image contrast though the first one is easy and simple.

The flow chart by using the latter image selection method is shown in Figure.5.1.

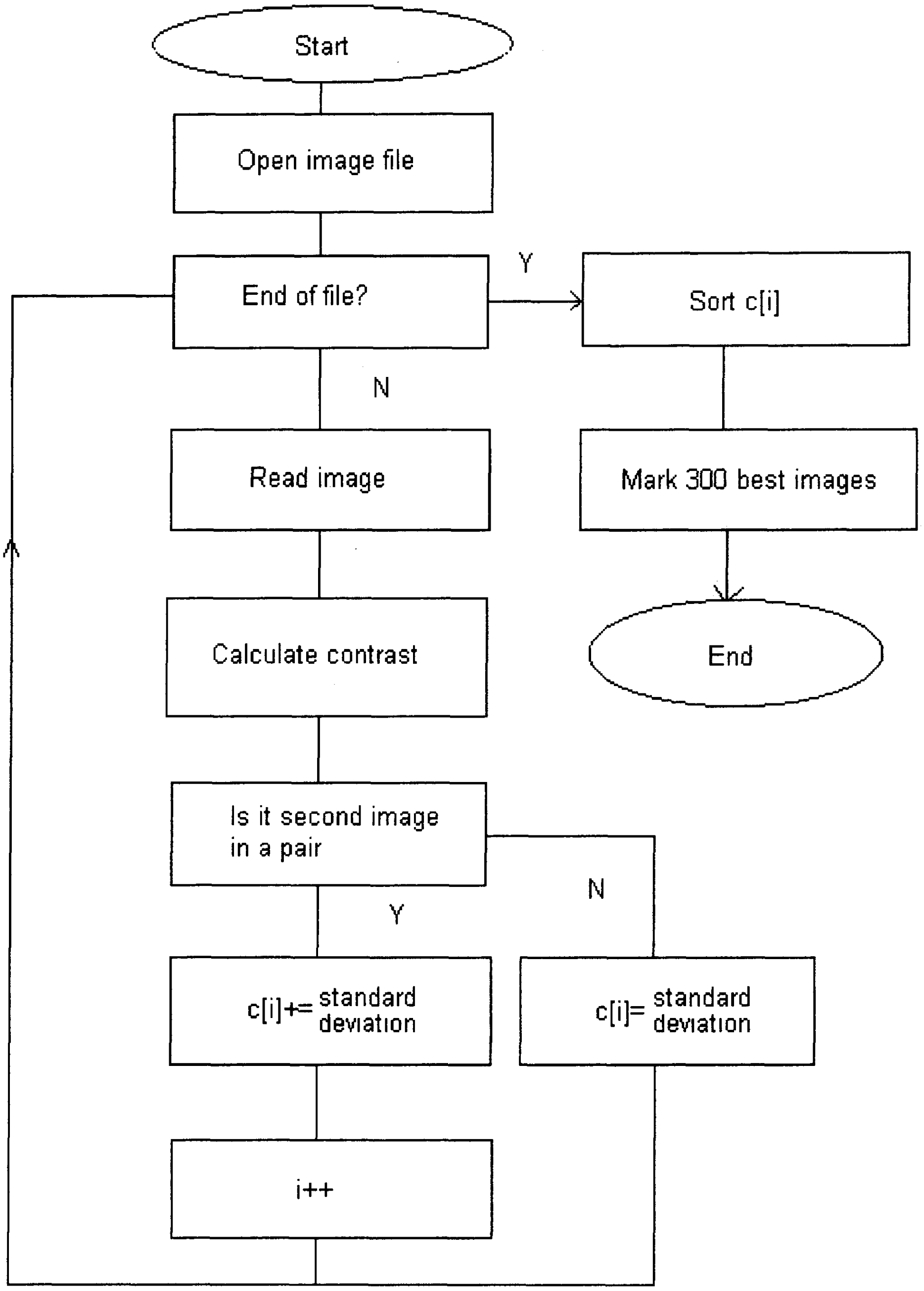

Figure 5.1 Image selection flowchart.

Figure 5.2 shows the standard deviations from a series of 1000 images.

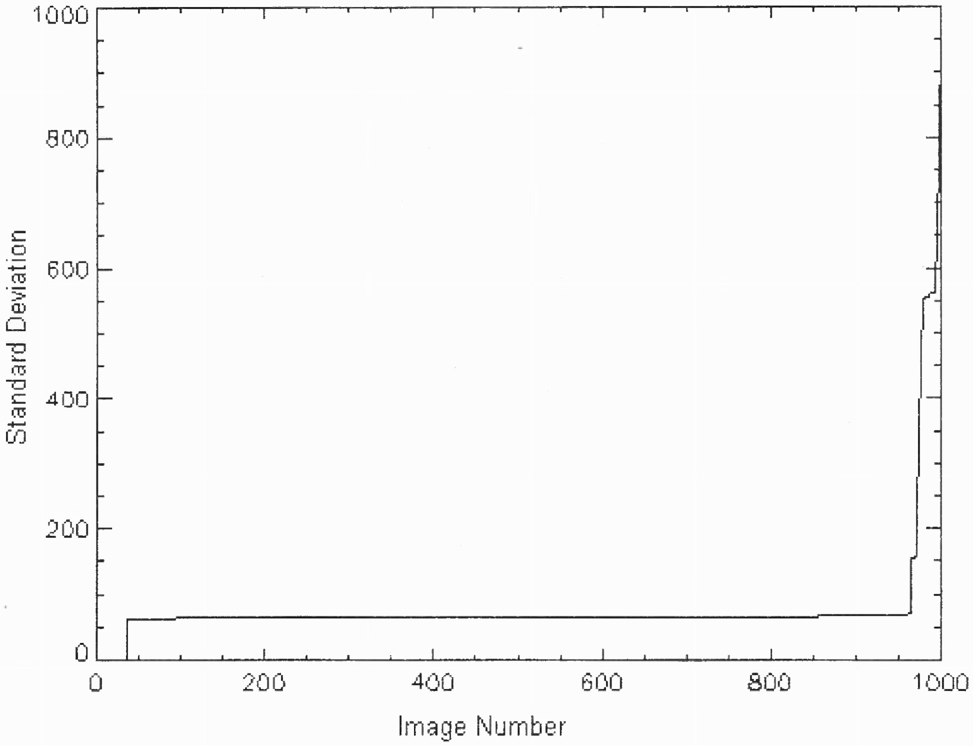

Figure 5.2 Sorted Image standard deviation in a series of 1000 images.

In Figure 5.2, the images with some highest contrasts and lowest contrasts are considered to be bad images and this has been proved by our tests. The best images should be considered in the upper right area, i.e., the area between 600 and 900. Actually, there is only a little difference between the best 300 and best 800 images in this data set, which means the standard deviation can only be taken as a relative quantity in analyzing the image quality. Some influences may not be correctly reflected in the standard deviation figure, such as image shift, whose influence on image contrast is small. Also, the figure tells us the image selection number or the critical point on the Kurtosis graph.

That the image selection could be effective in increasing the contrast could come about in two ways. One is because the 300 best images really are better than the other images. Alternatively, it may be just because of the reduced number of averaged images, because the cumulative image shift increases as the number of averaged image increases. A smaller number of properly selected images could result in a higher standard deviation while still effectively reducing the white noise, because the standard deviation due to the image properties is greater.

5.2 Image Analysis

Figure 5.3 shows the processed magnetogram by using the image selection and the original magnetogram.

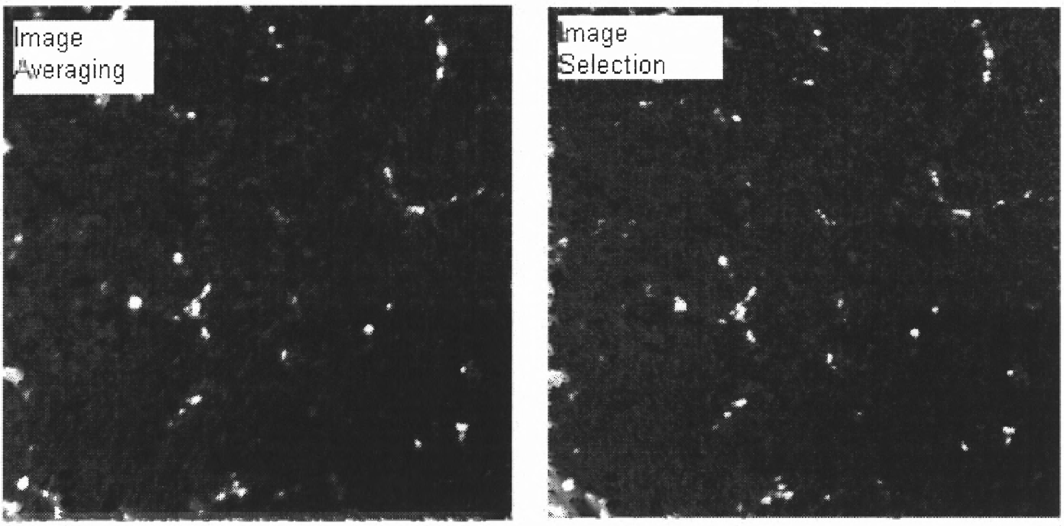

Figure 5.3 Image averaging vs image selection.

From the above figure, the overall improvement by using image selection is not very obvious, but in a small scale. By using image selection, magnetograph perfomance seems to have been slightly improved. Since the difference is not big enough, the discussion will be more focused on the contrast comparison and histogram comparison.

Figure 5.4 is the result of standard deviations after image selection compared with the standard deviation without image selection. Each data point from image selection is a result from 300 pairs of images and a total of 64x1000 images have been used in the analysis. From the figure shown above, the contrast improvement is obvious. The average enhancement in the standard deviation after image selection is about 3.85% though there is one magnetogram that even got worse than before using this measurement technique. This result proves that image selection is an effective tool in solar magnetogram construction.

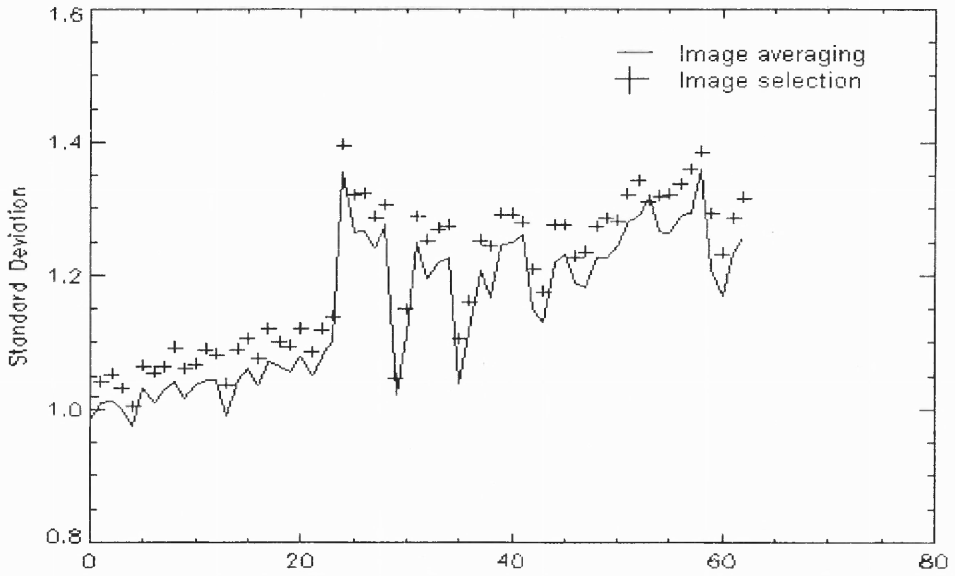

Figure 5.4 Contrast enhancement by using image selection.

From equation 4.6, the standard deviation due to reduced number of images taking part in the calculation of image averaging should be increased by:

$$\frac{\Delta\sigma}{\sigma}=\frac{\sqrt{(\frac{V_0}{M_1}+V_\infty)}-\sqrt{(\frac{V_0}{M_2}+V_\infty)}}{\sqrt{(\frac{V_0}{M_2}+V_\infty)}}, \tag{5.1}$$

where M_1 and M_2 are numbers of averaged images under the two schemes.

In our case, M_1 is equal to 300 frames and M_2 is equal to 460 frames (which is the number of averaged images used without frame selection). V_0 is equal to 200 and V_∞ is estimated to be 6.7(which comes from the calculated average image moment). The variance change $\frac{\Delta V}{V}$ that comes from the reduced image number should be as low as 0.2%. This shows that the contrast enhancement of ~3.85% is mostly due to the improvement in the quality of images that take part in the image averaging, despite the smaller number of images averaged. Figure 5.5 shows the comparison of the two histograms.

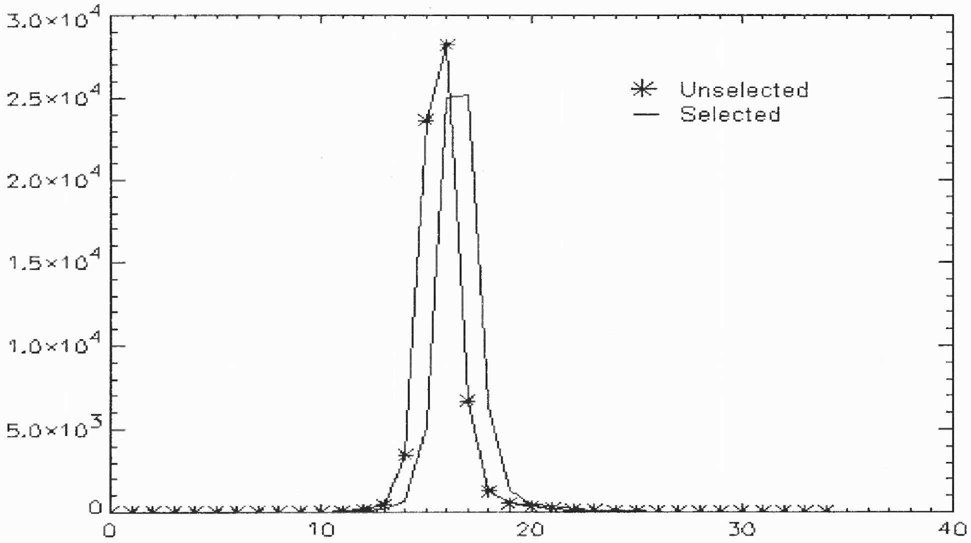

Figure 5.5 Histograms of selected and unselected magnetograms, the former is shifted 1 bin to the right for clarity.

From the figure, the histogram of the image processed by image selection has a wider peak. The corresponding σ represented by the two histograms are 6.39 and 6.97. The selected image histogram increased about 9%. This is not surprising because the standard deviation increased by about 3.85% and they are related by equation 5.1.

5.3 Fourier Spectrum Analysis

The following discussion will be carried out on Fourier domain. Figure 5.6 shows the comparison of logarithmic Fourier spectra before and after the image selection.

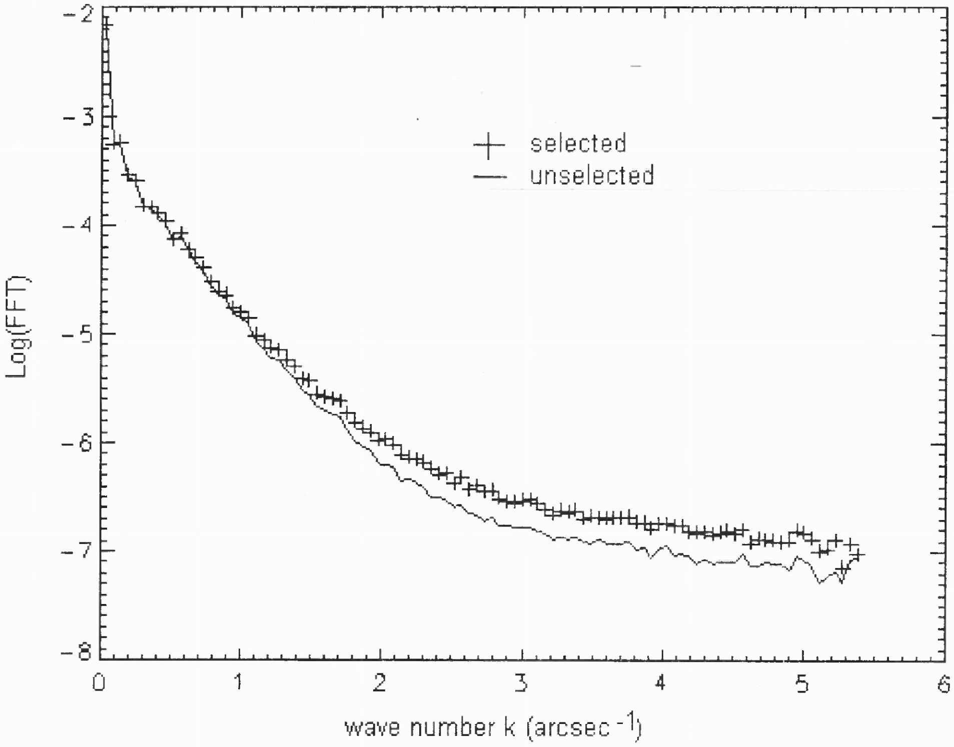

Figure 5.6 Logarithmic Fourier spectra.

From the figure, after image selection, the Fourier spectrum becomes stronger in high frequency area and remains nearly the same in lower frequency area.

There are two reasons that could result - more detailed information has been revealed in high frequency area, or more high frequency noise has been added to magnetogram. The above Kurtosis analysis and standard deviation analysis indicates that the increased high frequency spectrum means more detailed information has been revealed while the large-scale magnetic field remains unchanged.

From the figure, the increased power in frequency spectrum occurs mostly in the area lager than 1.5 arcsec^{-1} in frequency domain. Since the original magnetogram size is about 210 arc second, 1.5 arcsec^{-1} in frequency domain should correspond to a range of smaller than (2*3.14/1.5) = 4.2 arc second in the spatial domain. This indicates that the increased high frequency detail in solar magnetogram by image selection should be smaller than 4.2 arcsecond and that is why the image improvement may not be visually obvious in our image, which has a resolution of 210/256=0.82 arcsecond/pixel.

As shown above, though the number of averaged images decreases, the image quality enhances by ~3.85%. Since reduced number of averaged images can effectively reduce the influence of image shift, the image selection cannot only suppress white noise but also reduces systematic error.

CHAPTER 6

IMAGE ALIGNMENT

6.1 Image Correlation Relation

As described before, besides the random white noise, the sources of additional noise in magnetogram mainly come from two factors, seeing and stray light. Bad seeing usually comes from the disturbance of the earth's atmosphere, which results in a image shift between different images and also can result in a shift between different parts in a same image [1]. When obtaining solar magnetograms, in order to enhance the signal to noise ratio, usually hundreds or even thousands of images need to be added together to reduce the noise. In this case, the shift between images or the shift between different parts of the images will greatly reduce the image quality. To eliminate image shift, the image cross correlation method is a very useful tool and has been widely used in solar image processing [12-14].

Considering two images *f(x,y)* and *g(x,y)*, the cross correlation of the two images is defined as follows,

$$f(x,y) \otimes g(x,y) = \int f(u,v)^* \cdot g(u+x, v+y)dudv.$$

The Fourier transformation of the cross correlation is,

$$FFT(f(x,y) \otimes g(x,y)) = (FFT(f(x,y)))^* \cdot FFT(g(x,y)),$$

where * represents the conjugate function.

When *f(x,y)* and *g(x,y)* are identical,

$$FFT(f(x,y) \otimes g(x,y)) = (FFT(f(x,y)))^* \cdot FFT(g(x,y)) = |FFT(f(x,y)|^2,$$

then, the cross correlation becomes self correlation and the Fourier power spectrum reaches its maximum.

This principle can be very useful if taking *f(x,y)* and *g(x,y)* as two identical images only with a image shift $(\Delta x, \Delta y)$. When $\Delta x = \Delta y = 0$, the cross correlation of the shifted two images will reach its maximum.

When applied to the correction of image shift between two images, the procedures are,

1) Find a best image in a set of images to be processed as the reference image;
2) Calculate the Fourier transform and its conjugate;
3) For each image to be processed, calculate the Fourier transform, then multiply by the conjugate Fourier transform from step (2);
4) Apply inverse Fourier transform to the multiplication from step (3);
5) Find the maximum value in the correlation relation from step (4); The corresponding coordinates (x,y) of this maximum value are the image shift.
6) Use the calculated image shift to restore the image to its 'original' place.

Since in most cases, the image shifts are very different in different areas in the image, a local correlation method called the destretch method is often used in solar magnetogram processing.

In the destretch method, the image is divided into several sub areas. For each sub area, the relative image shift is calculated. Since different sub areas have different image shift, the corrected image is much more accurately restored than the image in a simple alignment method.

By testing few image series, the result shows that the simple alignment method could make the solar magnetogram even worse in some cases when the image size is relatively big. The destretched method is thus preferred over simple image alignment.

6.2 Destretched Image Analysis

Figure 6.1 shows the solar magnetograms before and after image destreching. The destretching method has been applied to each image before averaging. From the figure, as the destretching sub area becomes smaller, the image becomes sharper though the visual difference is small, and one has to compare them very carefully.

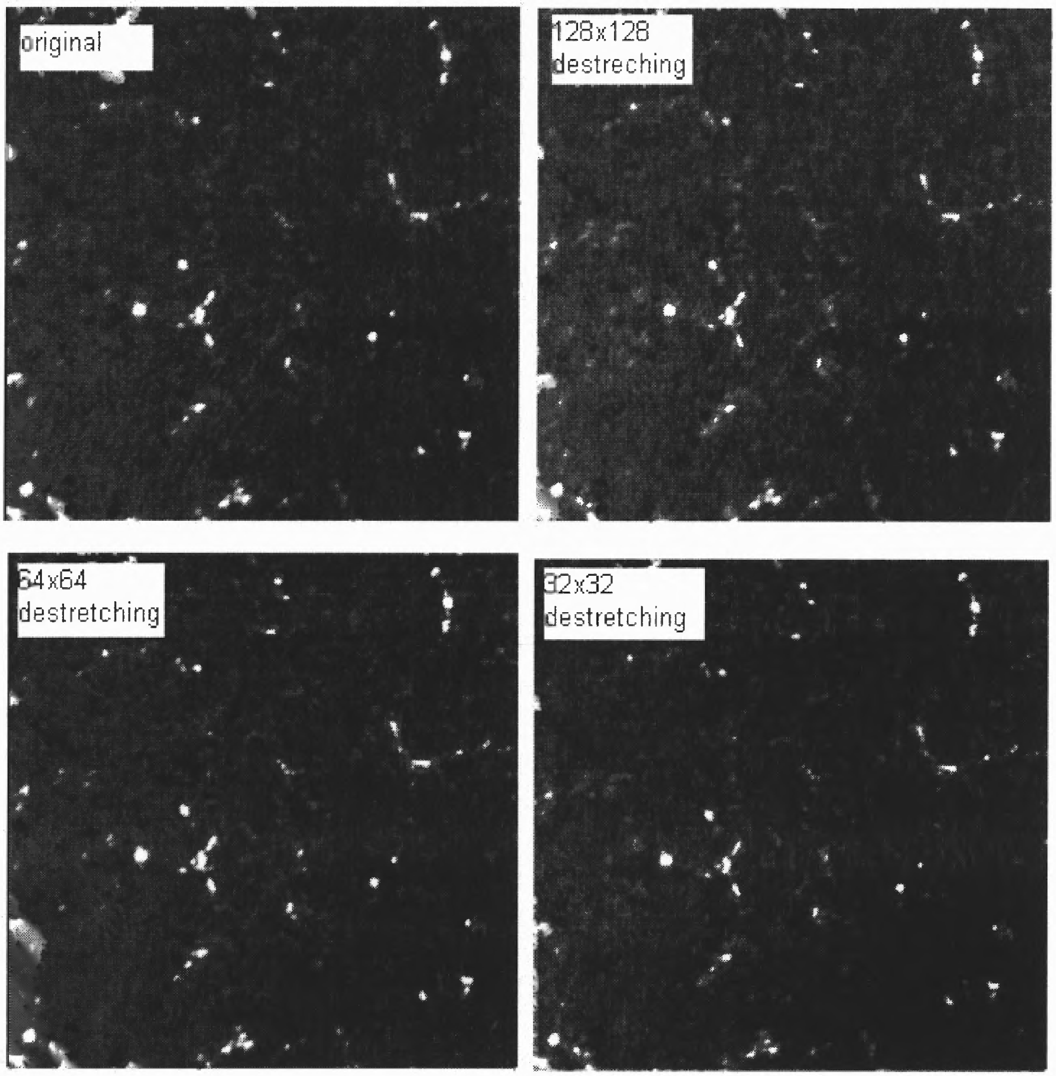

Figure 6.1 Original image and destretched images by using different sub sizes.

Actually, a further discussion will be carried out by comparing their standard deviations and their Fourier spectra. The efficiency of the destretching method really depends on each image. In our test, the maximum enhancement of the standard deviation can reach as high as 26.11%. Figure 6.2 show the best destretched image and its original image.

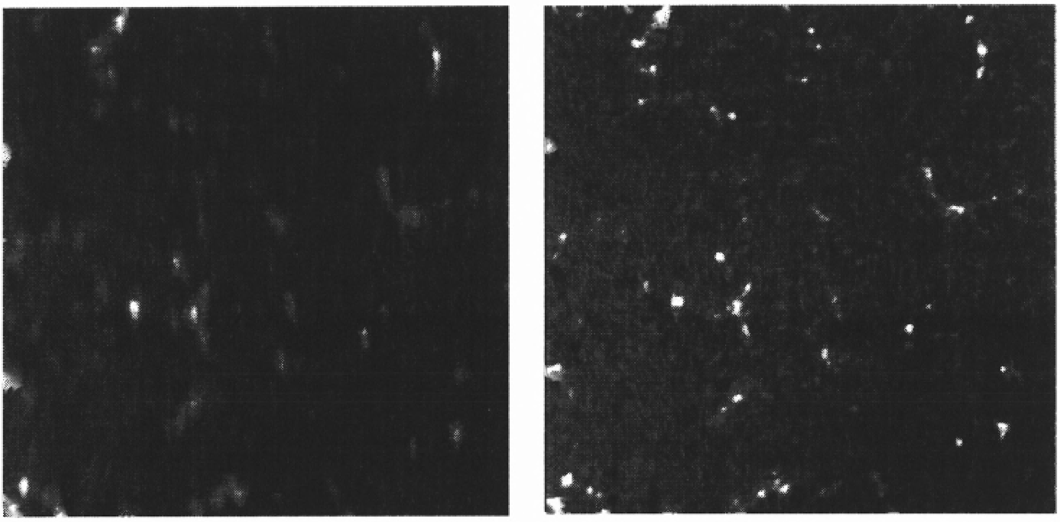

Figure 6.2 The maximum enhancement of the contrast can be as high as 26.11%.

Figure 6.3 show the changes in standard deviation before and after the 128x128 image destretching and the percentage change in image contrast, which tells us the efficiency of image destretching depends on each image that is being processed. The magnetograms corresponding to the peak value are shown in Figure 6.2.

Unlike the very stable efficiency in image averaging and image selection method, the contrast percentage change before and after a 128x128 image destretching varies from –5.44% to 25.09%. However, about 17.2% of the images actually show a decrease by an average of 1.3%. Even so, a total average percentage of 2.1626% increase in contrast has been achieved.

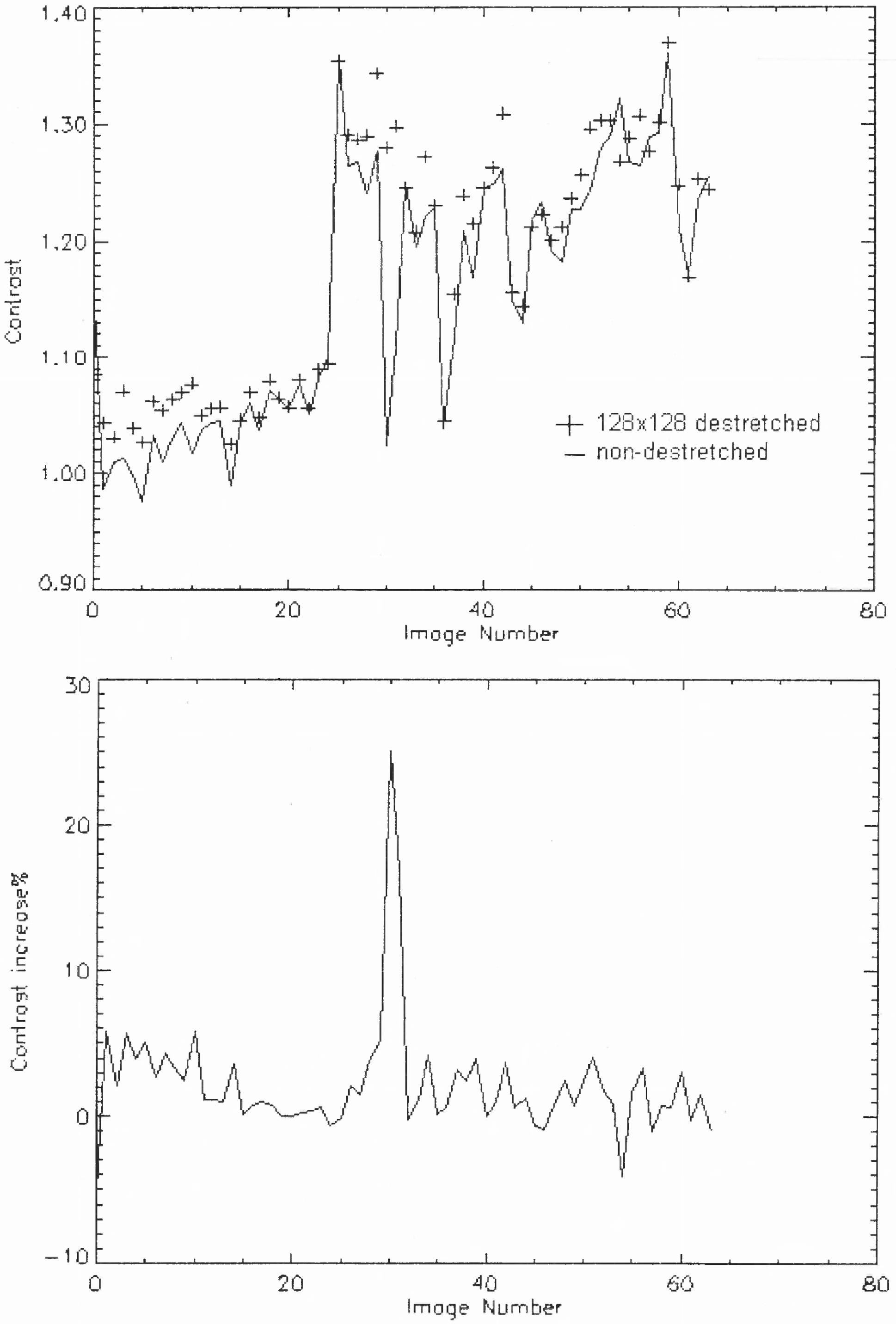

Figure 6.3 Contrast comparison and their percentage increase for 128x128 subareas.

Figure 6.4 shows the 32x32 destretched image contrast and its percentage increase in contrast.

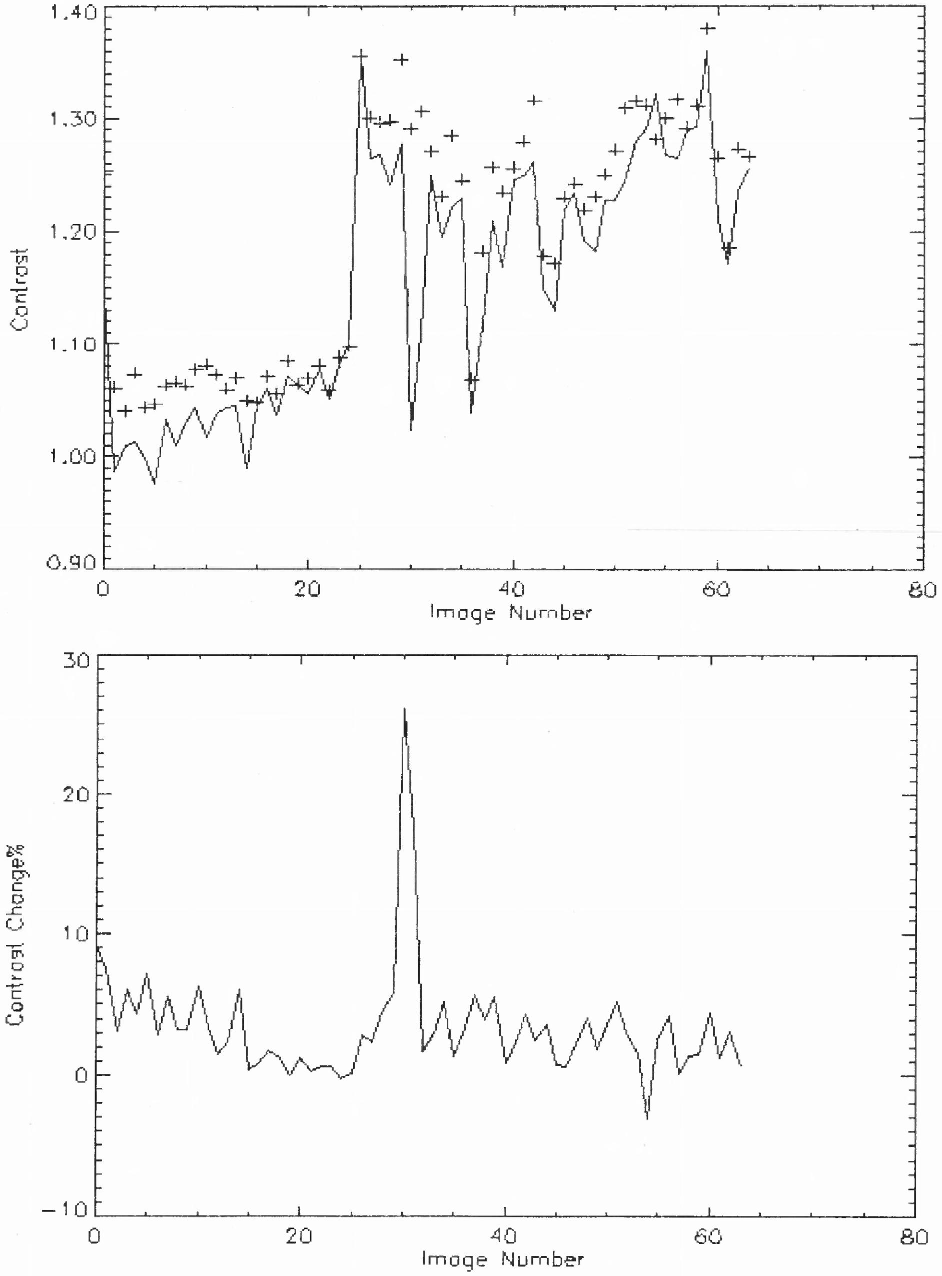

Figure 6.4 Contrast increase by using a 32x32 sub area.

As shown in the above figure, when destretched sub areas become smaller, this image processing method becomes more accurate and more efficient. For a 32x32 image destretching, the average percentage change in standard deviation ranges from –3.11% to 26.11%. The average image contrast change has been increased from 2.1626% to 3.4218%, and the total number of images that are wose than before have been decreased from 17.2% to 3.1%. This notable change indicates that it is very important to keep the destretched sub area small enough to increase its accuracy yet large enough to maintain efficiency.

From the above discussions, it should b noted that a substantial contrast enhancement has been achieved by using the image destretching method. The result shows that the smaller the destretching sub area, the bigger is the standard deviation. The average standard deviation increases are 2.1626%, 2.5943 and 3.4218% for 128x128, 64x64 and 32x32 destretching respectively. The increase is added to the 3.85% obtained by using the image selection method. The contrast increase in image selection is very stable, so it is a very effective tool in noise reduction independent of the images themselves, but the amount of improvement by the destretching method really depends on each individual image. From Figure 6.3 and Figure 6.4, the variance in the contrast enhancement in the image selection method is about 1.51% whereas, in destretching method, it is about 16.54%, which is much bigger than image selection and indicates that the image selection is much more stable in reducing image noise.

6.3 Fourier Spectrum Analysis

The logarithmic Fourier spectrum of destretched image and that of undestretched image are shown in Figure 6.5.

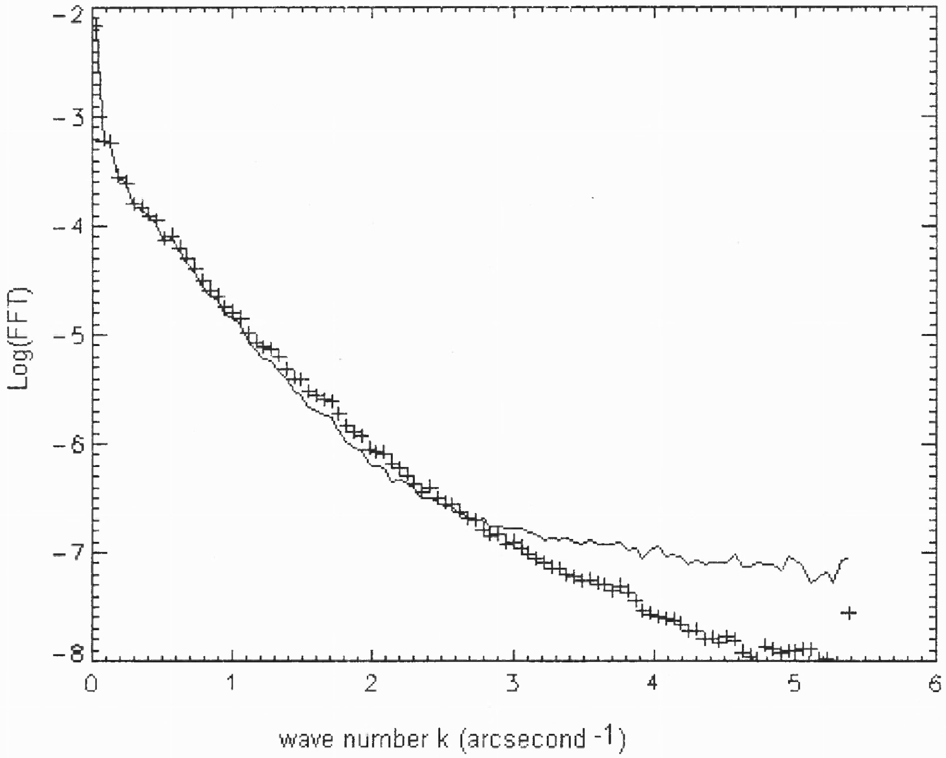

Figure 6.5 Logarithmic Fourier spectra.

From the above figure, the Fourier spectrum of destretched image remains unchanged in low frequency regime and become little stronger in lower-mid regime, then tends to fall off faster, especially in the high frequency regime, which indicates the some of the high frequency noise has been depressed and the noise size in spatial domain should be smaller than 2.2 arc seconds. The difference between the destretched method and the image selection method is that, in image selection method, the high frequency spectrum is stronger than before, which means the image details become richer but the noise introduced by image shift remains unchanged. In image destretching method, because the noise introduced by image shift has been largely eliminated, and the noise is mostly distributed in high frequency area with a scale of 2.2 arc seconds in our case, the Fourier spectrum tends to fall faster. This result is consistent with the result achieved ealier by other solar magnetogram processing researchers [9, 44]. Since image selection and destretching perform different functions, the two methods are usually combined together to eliminate the image shift and enhance the image quality.

Figure 6.5 shows the magnetogram's contrast changes by using destretching method only and combined with image selection. Figure 6.6 shows the their Fourier spectra.

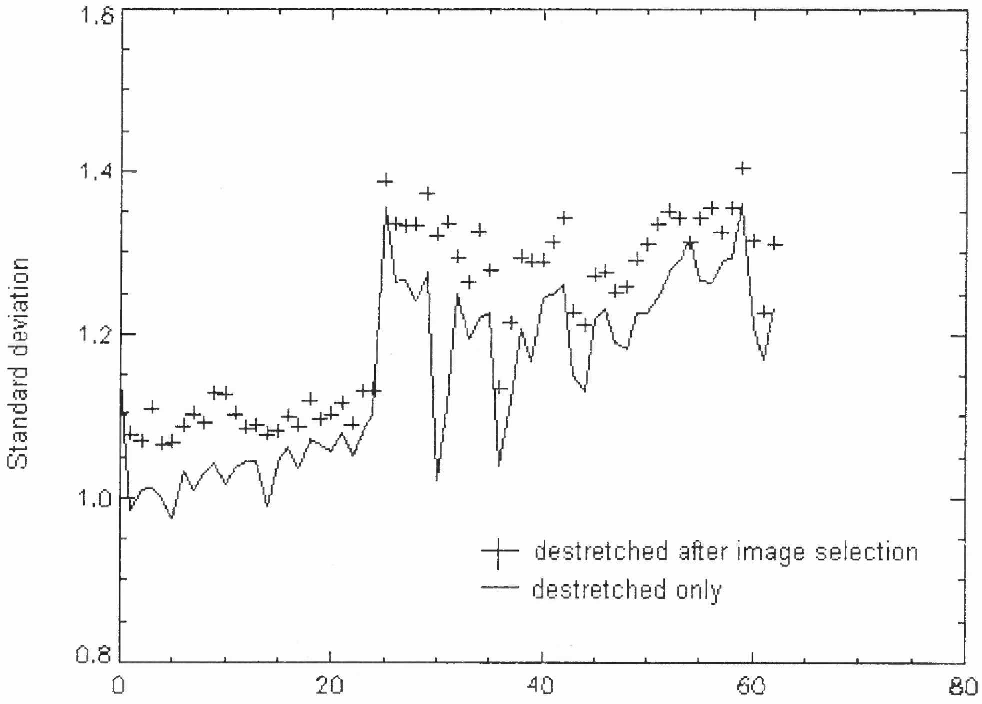

Figure 6.6 Contrast comparison.

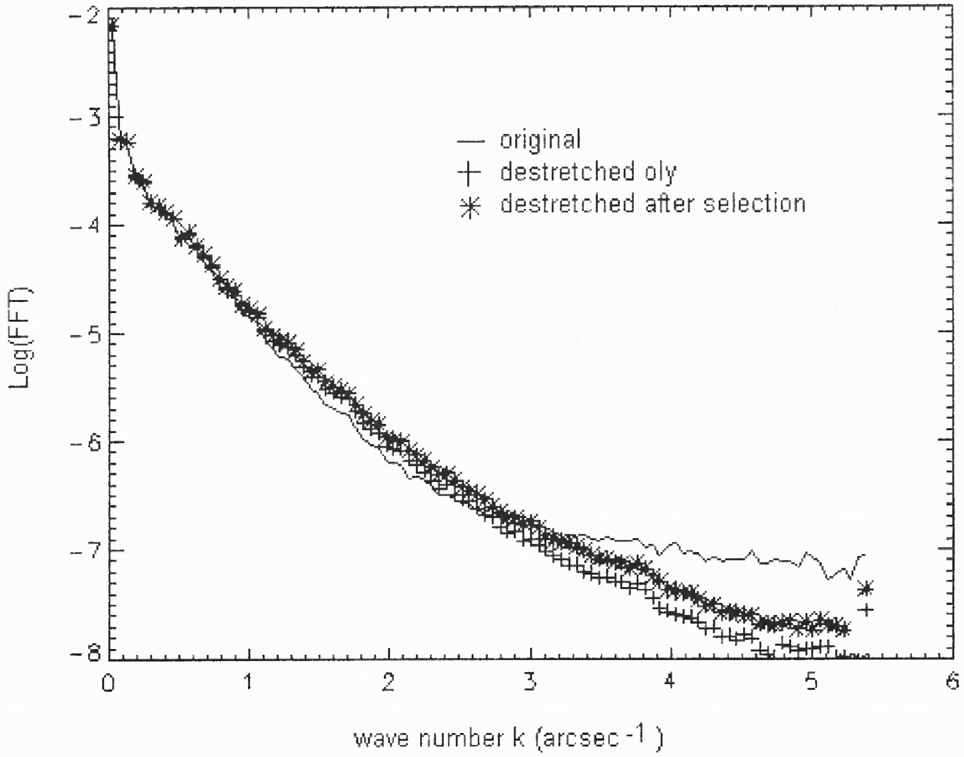

Figure 6.7 Fourier spectra comparison.

By performing image destretching after image selection, not only the image shift can be decreased effectively, but also more high frequency details can be preserved. This has been demonstrated in Figure 6.7, in which the combined destretching curve in high frequency area is lower than that in the image selection method. It is straightened in some scale but still bigger than the destretched only spectrum. By calculating the average image standard deviation, an average contrast of 6.21% has been achieved by using combined image selection and destretching method. Compared to image selection's 3.85% and image destretching's 3.42%, this method has shown its advantages in advancing image quality.

6.4 Conclusion

Image destretching method is an effective solar magnetogram processing tool. The processing result especially depends on the properties of the individual image. Compared with image selection, the Fourier spectrum falls much faster in a logarithmic graph. The intersection point of power spectrum of this method with original magnetogram has moved from 2.5 to 3.0, which means the depressed noise size has decreased from 2.51 arc seconds to 2.07 arc seconds and more details can be revealed.

CHAPTER 7

DECONVOLUTION METHOD

7.1 Stray Light Elimination

One of the difficulties often encountered in solar observations is the image smearing due to stray light produced by observing instruments and the Earth's atmosphere. Generally, stray light degrades spatial resolution, reduces intensity contrast and causes a systematic error in the measurement of light intensity especially in the low intensity regions. The stray light effect on magnetograph observations appears to be more serious than that on photometry [9-10], The key in eliminating stray light is to find the system point spread function (PSF). Several techniques can be used to find the point spread function and to correct the error, like deconvolution, Gaussian fitting and maximum entropy method [9-10, 34-39]. The devonvolution method is simple and easy to use but one noise free magnetogram has to be known in advance. The Gaussian fitting uses the Gufnagel [45] model to describe the atmosphere's disturbance, which has a Gaussian distribution, and by using this model, the point spread function can be obtained. To use Gauss fitting and Gufnagel model directly, the noise modification has to be considered by using a minimum variance method or maximum entropy method. The former method is actually a Wiener-Hopf filter and the latter is a modified Wiener filter [45, 9-10]. In the following chapters, the different methods to eliminate stray light have been studied in solar magnetograph.

7.2 Direct Deconvolution without Noise Modification

7.2.1 Basic Principle

The convolution of two functions $f(x,y)$ and $g(x,y)$ is defined as follows,

$$f(x,y)*g(x,y)=\iint f(u,v)\cdot g(u-x,v-y)dudv,$$

where * denotes convolution operator.

The Fourier transform of the convolution relation is as follows,

$$FFT(f(x,y)*g(x,y))=F(u,v)\cdot G(u,v),$$

where $F(u,v)$ and $G(u,v)$ are the Fourier transforms of $f(x,y)$ and $g(x,y)$ respectively.

The above relationship indicates that the Fourier transform of the convolution of two functions is equal to the product of the two Fourier transforms. This principle has been widely used in optical image and digital image processing.

In an ideal optical system, a point light source $\delta(x,y)$ should get a point image (response). But for the real optical system, the ideal response is impossible. The system response to a point light source usually will be a spread light distribution $h(x,y)$. This spread distribution $h(x,y)$ of a point function $\delta(x,y)$ is called the system's Point Spread Function (PSF). For the ideal optical system, this $h(x,y)$ should be a δ function. The Fourier transformation of the Point Spread Function is called Modulation Transfer Function (MTF), and is represented by $H(u,v)$. Also, for an ideal optical system, MTF should equal to 1.

When an image distribution $g_0(x,y)$ passes the optical system that has a PSF of $h(x,y)$, the output image $g(x,y)$ is just the convolution of $g_0(x,y)$ and the system point spread function,

$$g(x,y)=g_0(x,y)*h(x,y). \tag{7.1}$$

The Fourier transformation of the above equation is,

$$G(u,v) = G_0(u,v) \cdot H(u,v), \tag{7.2}$$

where $G(u,v)$, $G_0(u,v)$ and $H(u,v)$ are Fourier transformations of $g(x,y)$, $g_0(x,y)$ and $h(x,y)$ respectively.

Thus, the MTF is $H(u,v) = \dfrac{G(u,v)}{G_0(u,v)}$.

To obtain the original image $g_0(x,y)$ from the distorted image $g(x,y)$, an inverse filter M can be applied in Fourier domain to $G(u,v)$,

$$M(u,v) = \frac{1}{H(u,v)}, \tag{7.3}$$

and then, the final output image $f(x,y)$ will be exactly the same as $g_0(x,y)$,

$$f(x,y) = FFT(G_0(u,v) \cdot H(u,v) \cdot T(u,v)) = FFT(G_0(u,v)) = g_0(x,y). \tag{7.4}$$

7.2.2 Direct Deconvolution Method

The key in direct deconvolution method is to find the system's Point Spread Function or Modulation Transfer Function. From equations 7.1 or 7.2, if an ideal solar magnetogram $g_0(x,y)$ is known, then $h(x,y)$ can be calculated. This sounds like a logic loophole because $g_0(x,y)$ is just what needs to be obtained.

Fortunately, previous research work reveals that in quiet sun region near the solar center, the power spectrum of a large area has roughly the same Fourier distribution and with a circular symmetry [9-10], which means the point spread function is a real function, and also, the point spread function can be obtained just by taking the square root of the power spectrum. From this point, any high-resolution quiet sun image can be taken as the ideal image $g_0(x,y)$. Its power spectrum, averaged over annular region, divided by the power spectrum of our images leads to Modulation Transfer Function. Alternatively, as discussed below, the best image in a series of solar magnetograms also can also be taken as $g_0(x,y)$ and the MTF can be calculated. Once the MTF is known, the inverse filter can be used to deduct stray light.

For convenience, an assumption has been made that in one image sequence, the MTF calculated from all the even images equals to the MTF calculated from all the odd images (which has been tested using our observations). Then, the inverse filter can be applied to the magnetogram directly, which is proved as:

$$\begin{aligned} M_0(u,v) &= G_{even0}(u,v) - G_{odd0}(u,v) \\ &= \frac{G_{even}(u,v)}{MTF_{even}} - \frac{G_{odd}(u,v)}{MTF_{odd}} \\ &= \frac{G_{even}(u,v) - G_{odd}(u,v)}{MTF} \\ &= \frac{M(u,v)}{MTF} \end{aligned}$$

where $M_0(u,v)$ is the FFT of a stray-light-free magentogram, $M(u,v)$ is the FFT of a dirty magnetogram, $G_{even0}(u,v)$ is the FFT of a stray-light-free even image and $G_{even}(u,v)$ is the FFT of a dirty even image, and so on.

The steps used to obtain the reversed filter is as follows,

1) Select a high-resolution image as $g_0(x,y)$,

2) Calculate its Fourier transform, to get $G_0(u,v)$,

3) Average over annuli to obtain one-dimensional power spectrum, then convert to 2-D again by circular symmetry,

4) Repeat steps (2) & (3) for each to-be-processed image to get $G(u,v)$ for each image,

5) Divide $G(u,v)$ by $G_0(u,v)$ to get the Modulation Transfer Function,

6) Use the above derived MTF to restore its stray-light-free image $g_0(x,y)$.

7.2.3 Result Analysis

To use the deconvolution method or inverse filter to eliminate stray light, a reference image has to be known in advance. The power spectrum of the reference image will be taken as the stray-light-free power spectrum. By using mathematical methods, this power spectrum will be transformed into a 2-D circular, uniform symmetric function. When using this power spectrum to divide a dirty image, the quotient will be the MTF and its inverse Fourier transform will be used as the system's point spread function. In the first step, the image that has the highest standard deviation has been taken as the reference image. Figure 7.1 shows the calculated 1-d MTF and its 2-d image.

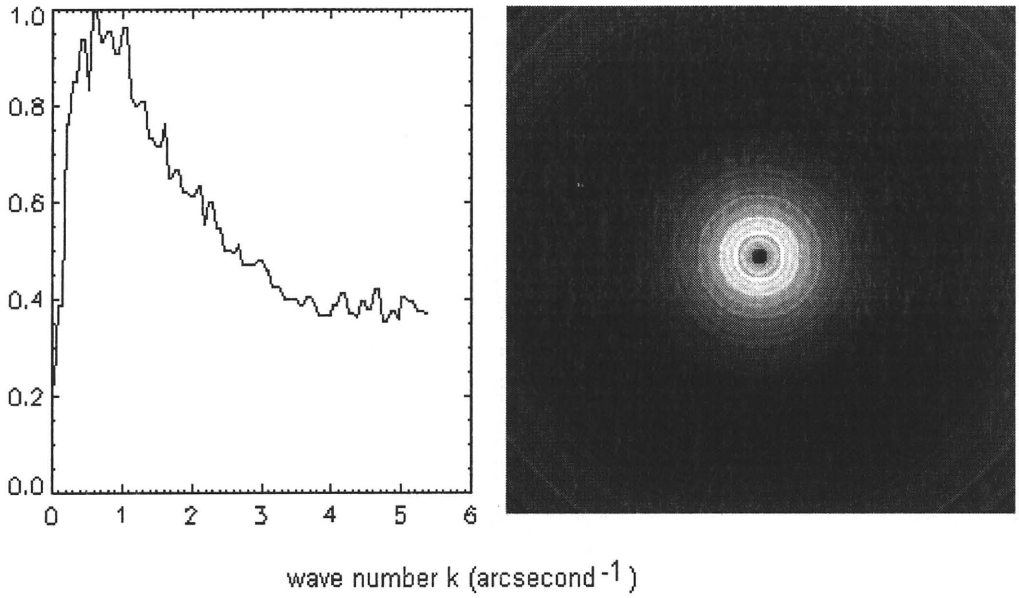

Figure 7.1 MTF in 1-D and 2-D generated by using the best image as reference.

Since the MTF has been assumed to have a circular symmetry, all the images that take part in the calculation of MTF has been processed by a 1-D digitized process. This leads to some tiny circular stripes in the figure. The 1-D scale has been divided into 100 levels. The deconvolved images are shown in Figure 7.2.

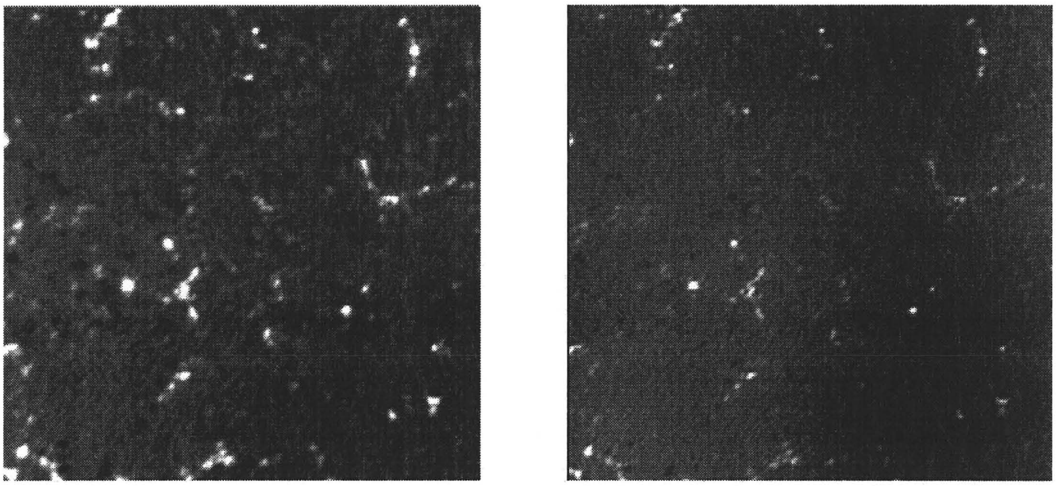

a)original image

b)deconvolved image

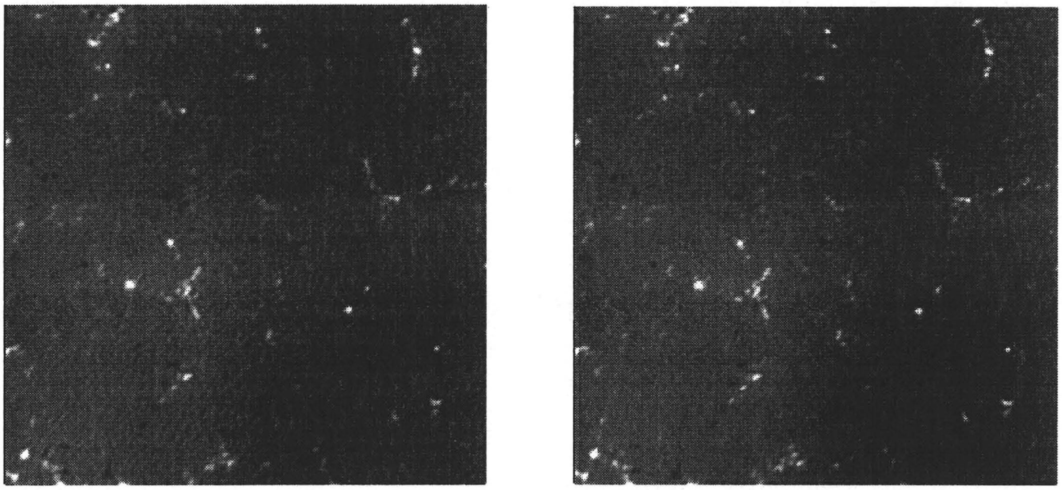

c)deconvolved image after image selectio

d)deconvolved image after image selection and destretching

Figure 7.2 Deconvolution applied to different magnetograms.

The result is quite exciting. The image processed by image deconvolution is much sharper and clearer. More details have been revealed than the original images. Also, as expected, the deconvolved images after image selection and destretching attain the most image enhancement. From visual inspection, the biggest image improvement has been achieved since using image averaging, which means the white noise and stray light are the two dominant noise sources in solar magnetograph observation. Figure 7.3 shows an enlarged local area in the above image. By comparing the two enlarged images, a ~28% increase in resolution has been obtained.

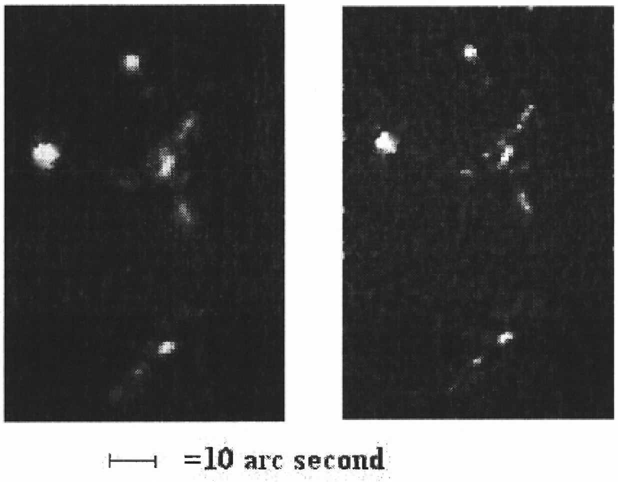

Figure 7.3 Enlarged local area.

The calibrated Fourier spectra have been drawn in a logarithmic scale in Figure 7.4. Since the stray light is distributed on both small and large scales, after image deconvolution the power spectrum in the low frequency regime has decreased significantly, but the power between k=1.5~4.5 has been greatly increased. Such a result tells us that the eliminated stray light was mainly distributed in a range larger than ~4.2 arcsecond and image details between 1.4-4.2 arcsecond have been largely enhanced. The unchanged high frequency part indicates that the direct deconvolution method nearly has no effect on stray light on very small scales, in accordance with previous work [9]. From Figure 7.4, the Fourier spectrum of the deconvolved image shows that the relative quantity of the high frequency spectrum has been increased, and the power distribution is similar to the expected intrinsic image power [46].

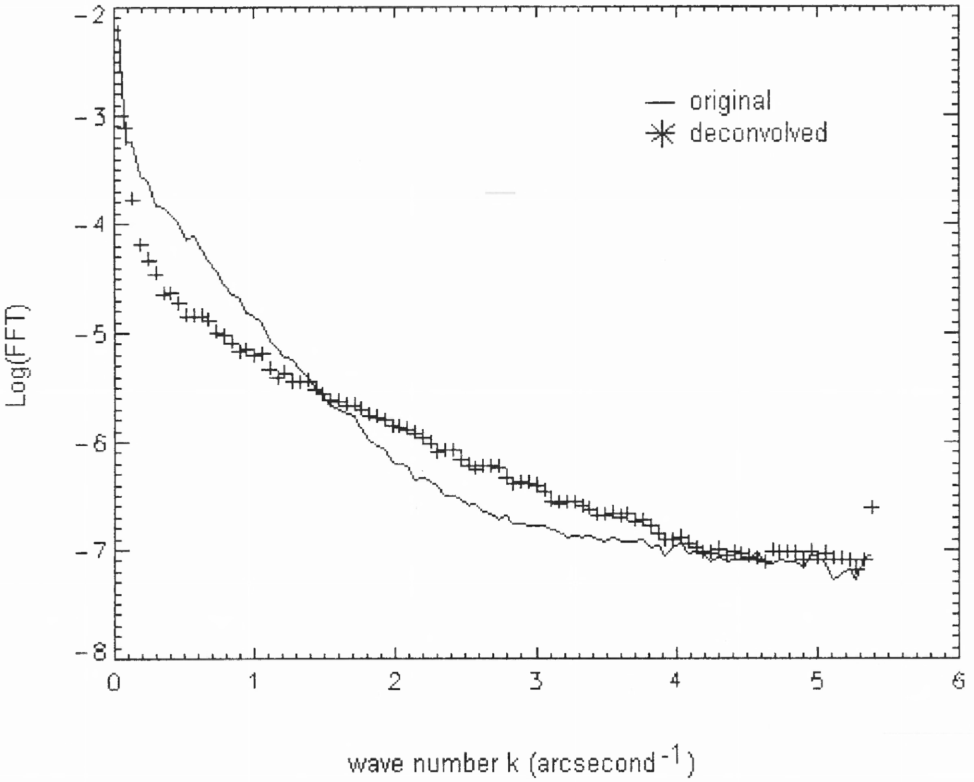

Figure 7.4 Fourier spectra comparison, original and deconvolved.

7.3 Direct Deconvolution with Noise Modification

7.3.1 Basic Principle

The above discussion assumes there is no noise present. If the noise cannot be neglected, equation 7.1 should be modified as follows,

$$g(x,y) = g_0(x,y) * h(x,y) + n(x,y), \tag{7.5}$$

where n(x,y) is the spatial noise, g(x,y) is the dirty image and g_0(x,y) is the noise free image.

Because of the random nature of n(x,y), the exact solution for original image g_0(x,y) cannot be obtained by solving equation 7.5 directly. In this case, the solution can only be obtained as near g_0(x,y) as possible. If the solution for equation 7.5 is f(x,y), then the nest step is to minimize the mean square error,

$$E = E[\{f(x,y) - g_0(x,y)\}^2]. \tag{7.6}$$

The solution for equations 7.5 and 7.6 is a Wiener filter (see Appendix A),

$$M(u,v) = \frac{H^*(u,v)}{H(u,v)\cdot H^*(u,v) + \Phi_n(u,v)/\Phi_0(u,v)}, \tag{7.7}$$

where *H(u,v)* is the system's MTF and $H^*(u,v)$ is the conjugate of *H(u,v)*. Φ_n/Φ_0 is the reverse of S/N ratio. When S/N→∞, M will become the reverse filter *1/H(u,v),* that was obtained before.

If *H(u,v)* is uniform in the azimuthal direction, which means it has a circular symmetry as discussed before, the filter becomes,

$$M(\rho) = \frac{H(\rho)}{H^2(\rho) + \alpha}, \tag{7.8}$$

where $\alpha = \Phi_n / \Phi_0$ is small. Typically, for our data, it can be taken as around 1/100.

7.3.2 Results Analysis

The best image in our image series has been used as the reference $g_0(x,y)$. From equation 7.8, the efficiency of the Wiener filter depends on the S/N ratio, different S/N could lead to a big difference in the processed images. Figure 7.5 shows the images processed by using different S/N ratios.

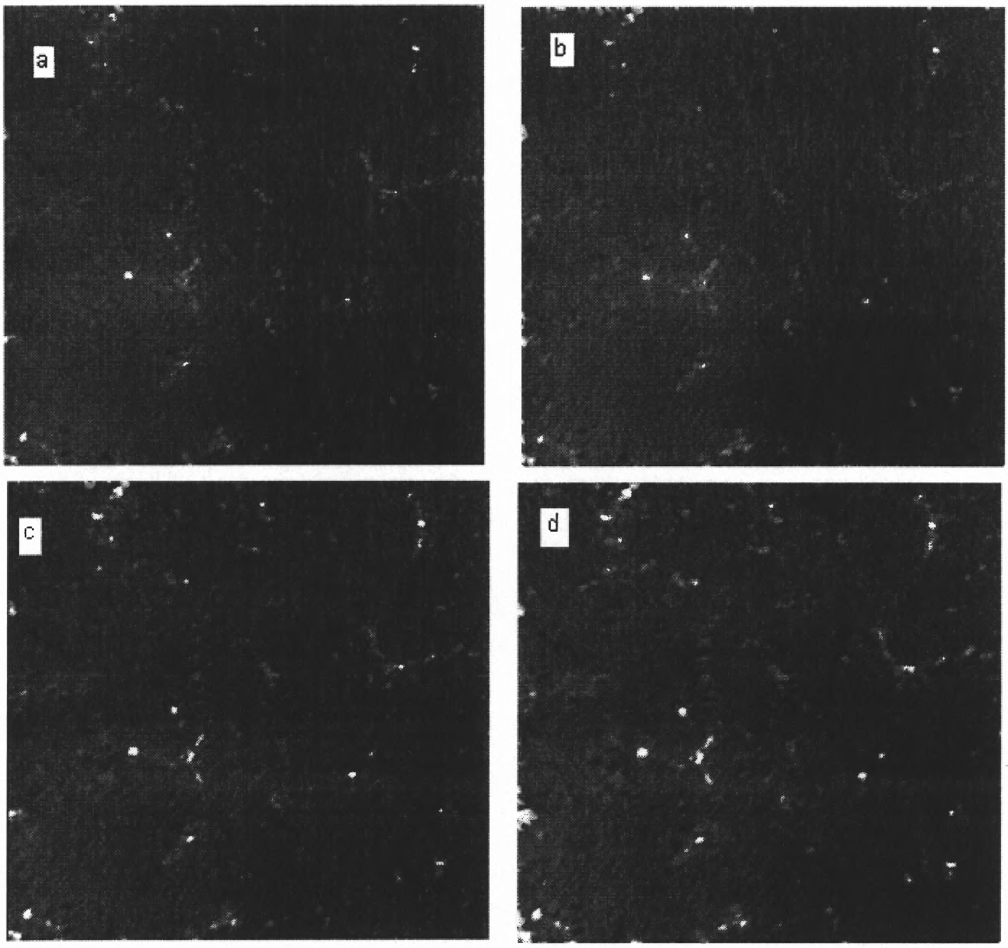

Figure 7.5 Deconvolution with noise modification based on different S/N ratio. (a) no modification, (b)100, (c)1, (d) 0.5.

From the above figure, it can be seen that the Wiener filter is a low-pass, smoothing filter. As the S/N ratio decreases, the smoothing becomes more extreme. When S/N decreased to 0.5, the image quality has been decreased to about the quality of the original undeconvolved image. The reason why the Wiener filter works so poorly in our case is that the random noise component has been reduced by image averaging. In the direct deconvolution method, the PSF comes directly from the real image that includes the noise which is then included in the MTF. This is very important because in the Wiener's model, the MTF is based on theoretical calculations of the properties of gaussian noise only. The MTF does not include other non-gaussian noise present in real seeing. Our conclusion is that Wiener filter is no longer helpful if an intensive image averaging and image destretching have been applied to the solar magnetogram first and the MTF comes from the seeing itself. But if somehow the image noise has not been deducted effectively before the deconvolution, the noise modified deconvolution is still recommended, which can also be seen form Figure 7.5. Furthermore, if the MTF cannot be derived from the seeing and has to be calculated by a mathematical method, thus the Wiener filter is required as seen in the next chapter.

7.4 Conclusions

The deconvolution method is very effective in eliminating the effects of stray light. The processed image is sharper and clearer. More high frequency details have been revealed from deconvolved images. The Fourier spectrum of the processed image tends to have more power at high frequencies and tends to approach the intrinsic power spectrum. When multiple intensive noise deduction methods have been used before the image deconvolution, such as image averaging, image selection and image destretching, and if the MTF has directly come from the seeing, a noise modification to the deconvolution is unnecessary. Though use of the Wiener filter is not so effective under this situation, it is still effective compared to those that have not used any deconvolution method at all. By looking at the Figure 7.6, one can conclude that, the deconvolution method has a very strong edge enhancement effect.

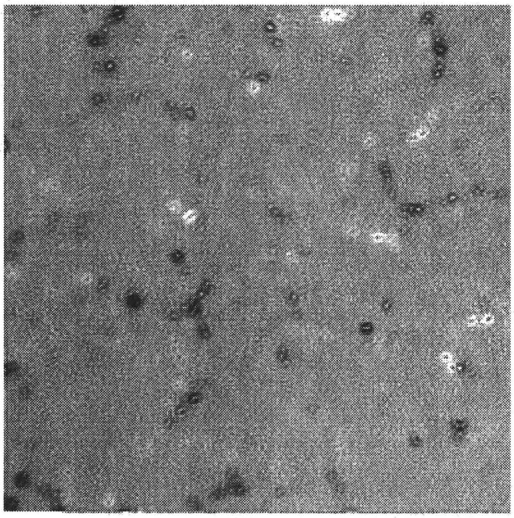

Figure 7.6 Image substraction of deconvolved and non-deconvolved images.

Finally, deconvolution is an easy, fast and very effective method that can be used to eliminate the stray light effectively in solar magnetograms. The spatial scale of the eliminated stray light is bigger than 4.2 arcsecond. When combined with image averaging, image selection and image destretching, the processed magnetogram has a very fine structure and a power increase has been observed between 1.4 - 4.2 arcsecond while the high frequency power remains the same. To obtain the maximum effect, a high-resolution image as near as possible to the ideal, must be used.

CHAPTER 8

GAUSSIAN FITTING

8.1 Basic Principle

The stray light in solar magnetograms come from both the disturbed Earth's atmosphere and the optical instrument used in observation. The shortcoming of the methods discussed in the previous chapter is that a high-resolution image is needed in advance. But, in some cases, a very clean high resolution image in advance is impossible, in which case the direct convolution method cannot be used.

There are different kinds of models to describe the atmospheric disturbance [10, 31-33]. In our experiment, the Gufnagel model is being used. According to Gufnagel [45], the disturbance caused by the earth's atmosphere can be described in a Gaussian function. If one can make sure that the main factor in a disturbed system is the atmospherov turbulence, then Gufnagel model could be very useful.

From Gufnagel, the turbulence caused by the atmospheric heating can be described by a system point spread function h(x,y) that has a Gaussian distribution. The h(x,y) can be written as follows,

$$h(x,y) = \frac{1}{2\pi\sigma^2} \cdot \exp[-\frac{x^2+y^2}{2\sigma^2}], \tag{8.1}$$

where σ^2 is the variance, and is a quantity that describes the influence made by the air disturbance.

By taking the Fourier transform of both sides of equation 8.1, the Modulation Transform Function can be determined,

$$H(\mu,v) = \exp[-2\pi^2\sigma^2(\mu^2+v^2)]. \tag{8.2}$$

This Modulation Transfer Function has a normalized value of 1 at image center (0,0).

Assuming the solar magnetogram has a circular symmetry, and this is often satisfied in solar magnetogram in quiet sun near solar center as indicated before, then, from Wiener filter,

$$\begin{aligned} M(\rho) &= \frac{H(\rho)}{H^2(\rho)+\alpha} \\ &= \frac{\exp(-2\pi^2\sigma^2\rho^2)}{\exp(-4\pi^2\sigma^2\rho^2)+\alpha} \end{aligned} \tag{8.3}$$

where $\rho = \sqrt{u^2 + v^2}$, α is the inverse of signal to noise ratio. Usually α can be taken as a constant.

Equation 8.3 is the Fourier domain filter that will be used in our Gauss Fitting processing.

8.2 Determination of Gufnagel Model

From equation 8.3, Wiener filter based on Gufnagel model could be very different according to two important parameters, air disturbance σ and signal to noise ratio α. The only best way to determine the air turbulence and S/N ratio could be to compare different image processing result by using different parameters. Since the visual change that results from different parameters would be very small in a whole field of view, only some key features from the image have been taken and enlarged to compare, such as some relatively stronger magnetic field.

By looking over several images that use different air turbulence conditions, the parameter σ has been determined roughly between 1.26~12.6 arcsecond. The tests will be carried out in this range.

Figure 8.1 shows different local area images processed by using different air disturbance σ. While doing the comparison, α has been taken as a constant of 0.01 corresponding to a standard signal to noise ratio of 100.

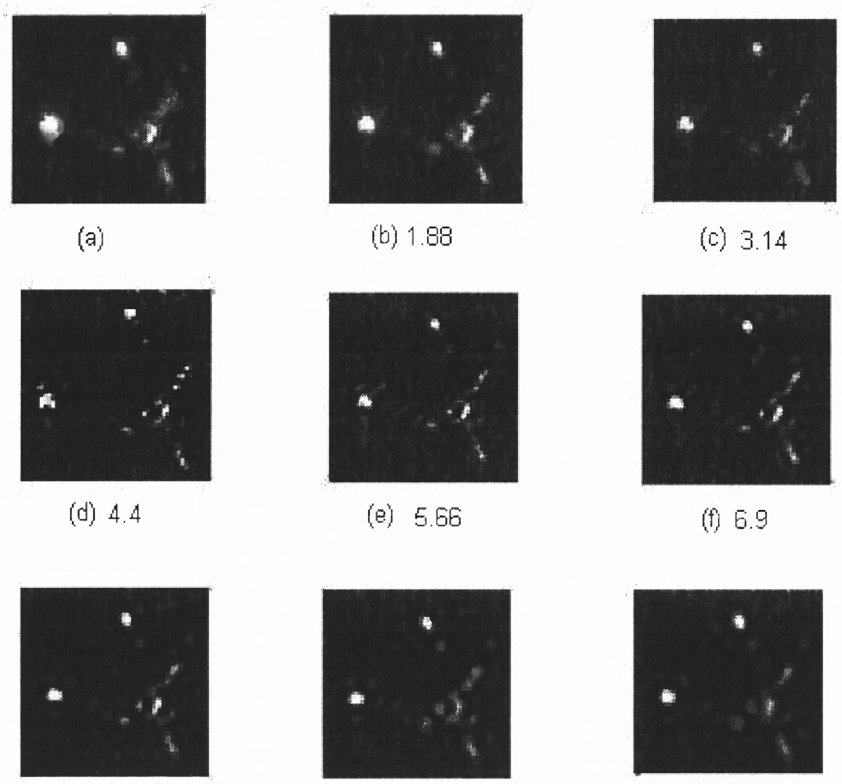

(a) (b) 1.88 (c) 3.14

(d) 4.4 (e) 5.66 (f) 6.9

(g) 8.16 (h) 9.42 (i) 10.1

Figure 8.1 Original image (a) and Gauss Fitting processed images (b)-(i) with different parameter σ (arc second). The image size is 41 arcsecond.

From the above images, as σ increases from 1.88 to 5.66, the image becomes sharper and clearer. As for σ = 8.16, image (g), the edge is becoming coarser and distinct tingling appears. It is very easy to determine that the best air turbulence σ should be taken as between 4.4-5.66 arcsecond. In the following discussion, σ has been chosen as 5 arcsecond. Also from Figure 8.1, the filter's effect on edge enhancement is very strong. But when σ becomes too big, the images become over-enhanced at the edges of features and cause the other details to nearly disappear. From this point of view, the Gufnagel model based Wiener filter acts like a differential filter that has a very strong effect on edge enhancement, and the air turbulence is just the displacement that controls the scale of enhancement.

With σ as 5 arcsecond , the next step is to determine noise to signal ratio α. Also, this could be a meaningful method in determining an image's S/N ratio. Only a sub-window is used to judge the best α. The comparison results are shown in Figure 8.2.

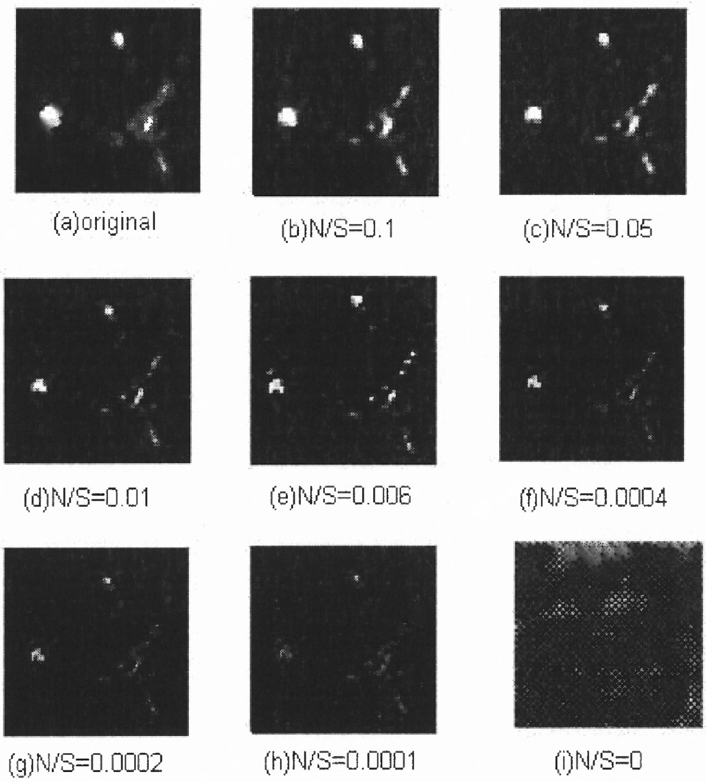
(a)original (b)N/S=0.1 (c)N/S=0.05

(d)N/S=0.01 (e)N/S=0.006 (f)N/S=0.0004

(g)N/S=0.0002 (h)N/S=0.0001 (i)N/S=0

Figure 8.2 Original image and Gauss Fitting processed images with different N/S ratio.

From Figure 8.2, it is easy to see that the best α is between 0.006~0.008 corresponding to a S/N ratio between 1.25%~1.67%. Another conclusion that can be derived from the above figure is that the effect of varying α is totally different from that of σ in the Gufnagel based Wiener filter. The α parameter controls the image resolution more like a high-pass filter. When α is 0, Wiener filter is degenerated to an inverse filter, and only gaussian noise can be eliminated as discussed before.

8.3 Result Analysis

Figure 8.3 shows the Wiener filter based on the Gufnagel modle. The turning point in high frequency area means a heavy drop for this component and the turning point is determined by α.

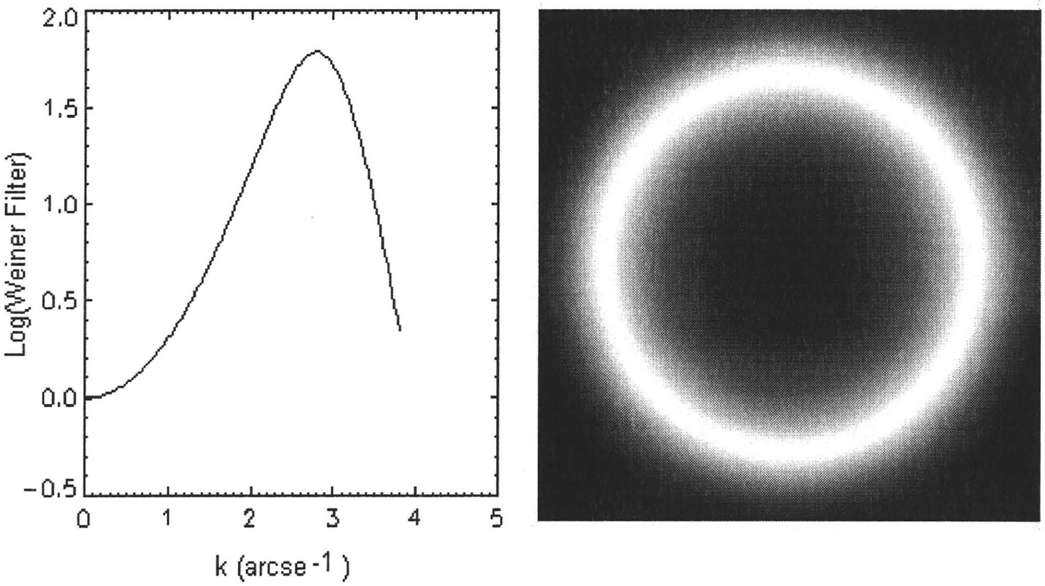

Figure 8.3 Wiener filter based on Gufnagel Model , with σ=5, α=0.007.

Figure 8.4 shows some images from different image processing procedure.

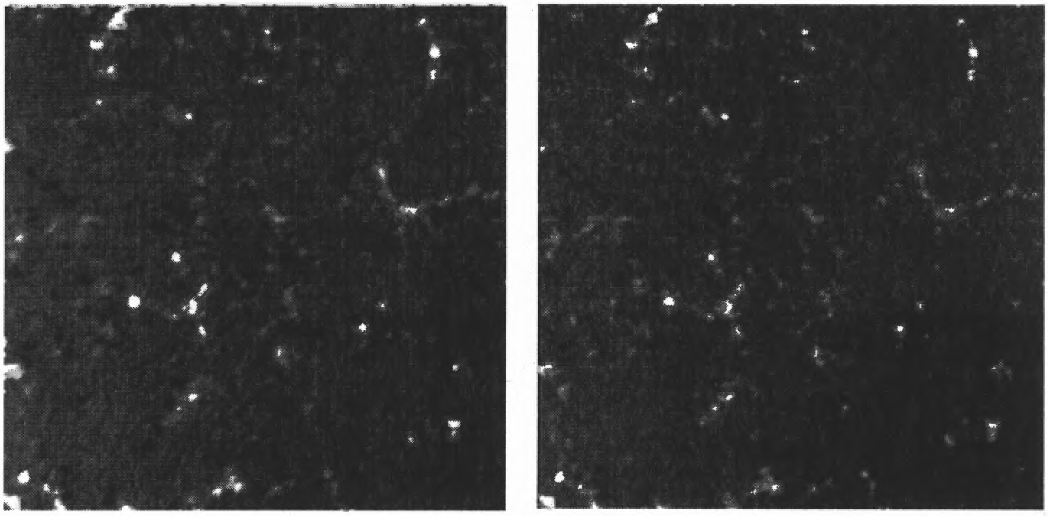

(a) original image

(b) destretched after image selection

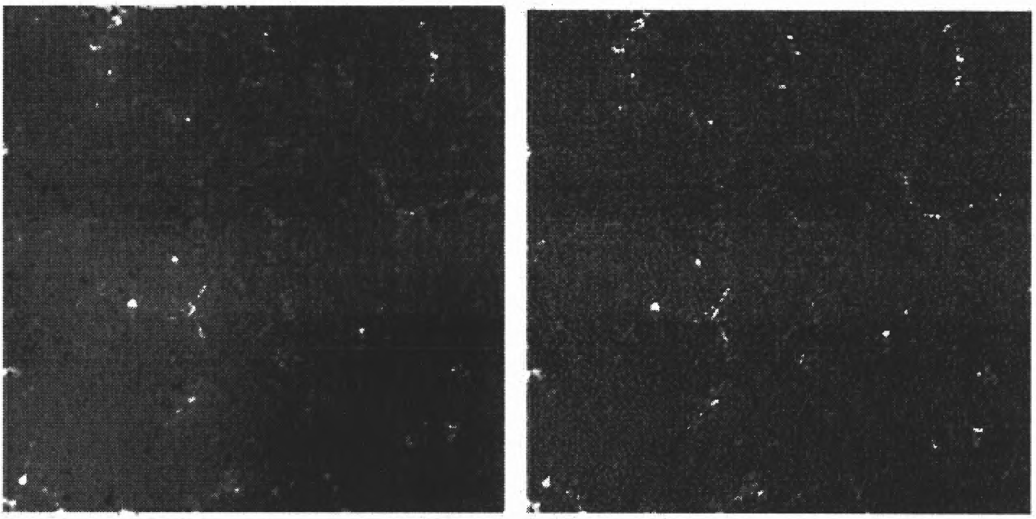

(c) direct deconvolution

(d) Gauss fitting

Figure 8.4 Image comparison by using different image processing methods.

From Figure 8.4, Gauss Fitting processed image (d) is obviously sharper when compared with image (a) and (b). This is very important to us since it means that even if any high quality reference image is not ready for use, the Gufnagel model and Wiener filter still can be used to eliminate stray light. One thing to remember is that, by using Gufnagel model, the assumption has been made that, the stray light is mainly due to the atmospheric heating turbulence rather than due to instruments.

Another notable prospect in Figure 8.4 is that though image quality has been greatly improved by using Gaussian fitting, when compared with image (c), it is still a little worse. The reason is quite straightforward. Since the MTF used by direct deconvolution reflects a real seeing condition when the image was taken, the MTF not only includes the atmospheric heating turbulence, but also includes the stray light from optical instruments which is not included in Gufnagel model. Figure 8.5 shows the comparisons of logarithmic Fourier spectra of above four images.

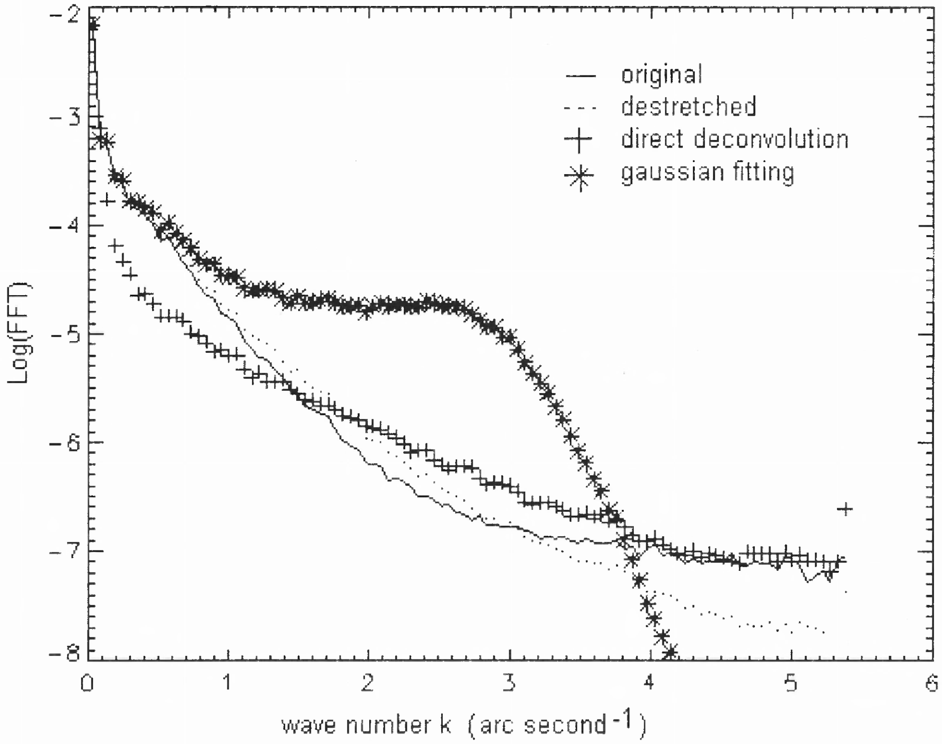

Figure 8.5 Four typical Fourier spectra.

Except the two lower Fourier spectra that have been discussed before, the difference between the direct deconvolution and Gauss fitting is notable. The big difference between Gauss fitting and direct deconvolution is their different attitude towards the noise. In direct deconvolution method, all the environmental influence has been included in MTF, while in Gauss fitting, only the stray light that comes from air turbulence with gaussian distribution has been included. That is why the noise modification must be used when using Gufnagel model. From Figure 8.5, both deconvolution and gaussian fitting methods increase the power in the area around 1.5-6.0 arcsecond. But, when entering the small-scale area, the FFT of Wiener filter processed image takes a sharp turn and begins to drop deeply. This is what leads to the smoothing evident in Figure 7.5. This sharp turn reflects the fact that the Wiener filter thinks the high frequency regime has been heavily polluted by noise and has to be deducted which can be seen from Figure 8.3. On the contrary, the FFT of deconvolution processed image still keeps its direction and holds the straight shape till a very high frequency regime. The real reason has to be that, in direct deconvolution method, since MTF has included every information it needs to filter the stray light, it can very effectively distinguish image signal from its background stray light. On the other hand, the Gufnagel model is just a mathematical model to describe some idealized air turbulence (though it is very successful). Since α is the parameter used to judge the noise level in Gufnagel model, the bigger the α is, the more high frequency component will be cut in Wiener filter. To support our analysis, the Fourier spectra of different α levels have been shown in Figure 8.6.

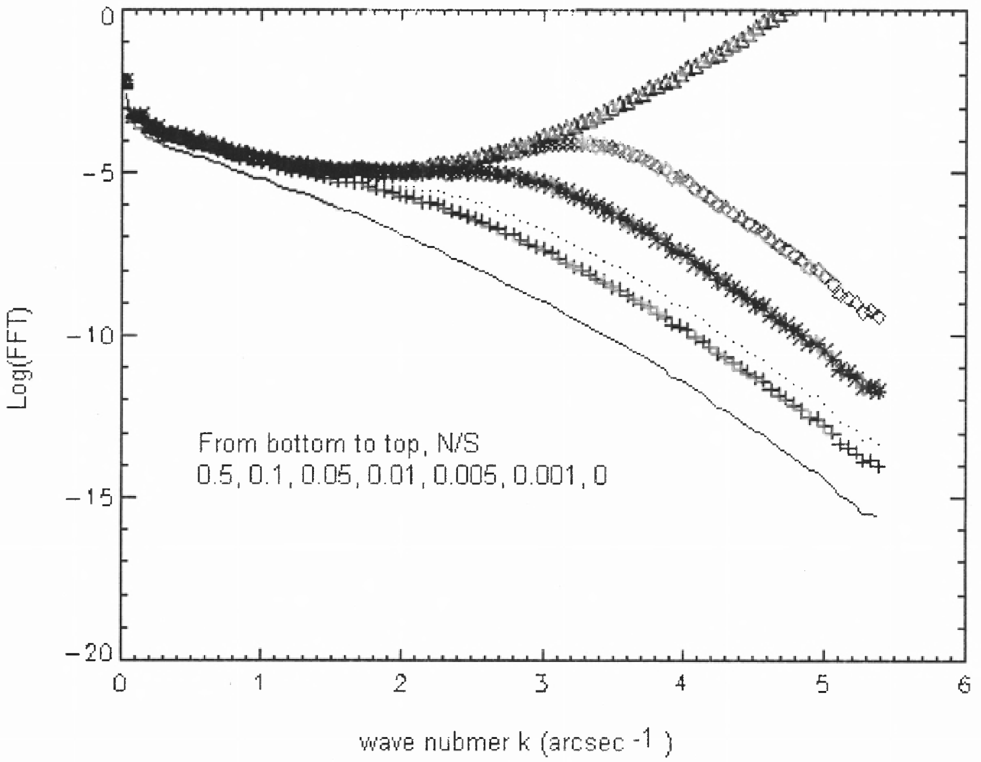

Figure 8.6 Fourier spectra of processed magnetogram with different N/S ratio by using Gauss Fitting.

From the above figure, it is easy to see that, when α becomes larger, the more noise will be supposed to be included in the original image and the more high frequency signal will be lost. When α equals 0, all the high frequency component will not be depressed at all. Actually, they are all amplified, but the image then becomes awful as shown in Figure 8.2. The big difference between the seeing generated MTF and Gauss fitted MTF is that the former contains most of the noise effects that come from the seeing. Then, the stray light can be effectively eliminated from the image.

8.4 Conclusions

The Gaussian fitting by using Gufnagel model is a very effective way to eliminate the stray light effect on solar magnetogram. The method is especially useful when a high-resolution reference image cannot be obtained in advance. The processed image by using Gauss fitting is much better than before which proves that the stray light has been very effectively depressed or eliminated. Due to its limitation, the Gauss fitting has to be combined with some noise modification method, such as Wiener filter. Though its result is very impressive, the processed image is still a little worse than the processed magnetogram by using the MTF that comes directly from the comparison with reference image. Finally, if a high-resolution reference image exists in advance, the direct deconvolution is still recommended before utilizing Gauss fitting. But, if the high-resolution reference image cannot be obtained in advance, Gauss fitting is highly recommended because it is very effective in eliminating stray light effect and also it is very simple and easy to use.

CHAPTER 9

MAXIMUM ENTROPY METHOD

Gauss fitting is derived from a very basic principle that relates to minimizing the mean square error. In this chapter, another principle, maximizing entropy, has been investigated to derive another most approached image solution.

Maximum entropy method has been widely used in astronomical image processing[35-39]. Different methods can use different entropy definition[34]. In this chapter, the maximum entropy function has come from Gull and Skilling[47], and the method is based on Jongchul Chae's work[10].

9.1 Basic Principle

Assume $g(x,y)$ is the blurred image, $g_0(x,y)$ is the noise free image and $h(x,y)$ is the system's point spread function. Then,

$$g(x,y)=g_0(x,y)*h(x,y), \qquad (9.1)$$

where * denotes convolution operation.

The goal of Maximum Entropy is to determine a two-dimensional distribution f(x,y) under the constraint

$$a(x,y)g_0(x,y)+b(x,y)>0, \qquad (9.2)$$

with any specified distributions $a(x,y)$ and $b(x,y)$.

The maximum entropy principle uses a Bayesian approach which maximizes the function

$$H_H=\alpha S+L, \qquad (9.3)$$

where S is the entropy which is a measure of the solution's compatibility with a priori information, and L is the likelihood which is a measure of the solution's fitness to data. The parameter α, a regularizing parameter, determines the weights of the two terms.

According to Skilling [47], the entropy of the solution can be defined like

$$S = \sum_{i,j} (z_{i,j} - m_{i,j} - z_{i,j} \log {}^{z_{i,j}} \big/ {}_{m_{i,j}}), \tag{9.4}$$

where m can be any kind of image and z could be a positive-definite variable

$$z(x, y) = a(x, y) g_0(x, y) + b(x, y)$$

and the likelihood can be defined in Fourier domain

$$L = -\frac{c}{2} \sum_{\mu,v} | G_{0_{\mu,v}} H_{\mu,v} - G_{\mu,v} |^2 , \tag{9.5}$$

where G_0, H and G are the Fourier transforms of *$g_0(x,y)$, $h(x,y)$ and $g(x,y)$* respectively.

The iterative formula for *$g_0(x,y)$* or equivalently, *$G_0(\mu, v)$* which maximizes H can be written as[10]:

$$G_{0i,j}^{(k+1)} = \frac{G_{i,j} H^{*}_{i,j} + \alpha(\lambda^{(k)} G^{(k)}_{0i,j} - Q^{(k)}_{i,j})}{| H_{i,j} |^2 + \alpha \lambda^{(k)}}, \tag{9.6}$$

where $Q^{(k)}_{i,j}$ and $\lambda^{(k)}$ are given as follows,

$$Q^{(k)}_{\mu,v} = \frac{N \sum_{i,j} a_{i,j} \log({}^{z^{(k)}_{i,j}} \big/ {}_{m_{i,j}}) \Theta(i, j, u, v)}{\sum_{i,j} a^2_{i,j} / m_{i,j}}, \tag{9.7}$$

$$\lambda^{(k)} = \frac{N \sum_{i,j} a^2_{i,j} / z_{i,j} (\delta g^{(k)}_{0i,j})^2}{\sum_{i,j} a^2_{i,j} / m_{i,j} \sum_{i,j} (\delta g^2_{0i,j})^2}, \tag{9.8}$$

where $\Theta = e^{2\pi i(ui/N+vi/N)}$ is the Fourier kernel, and $\delta g_{0i,j}^{(k)}$ is the inverse Fourier transform of $\delta G_{0u,v}^{(k)}$, which is the error of each iteration.

Equations 9.6, 9.7 and 9.8 are the solutions for equation 9.1 that maximizes the entropy. Since equation 9.6 is an iteration equation, the initial value for $G_0(u,v)$ is very crucial here. From the experience provided by Jongchul Chae, the initial value for $G_0(u,v)$ has been taken as $G(u,v)$.

From the above discussion, the basic procedures to use the maximum entropy method are as follows,

(1) Give $a(x,y), b(x,y), m(x,y), g(x,y), h(x,y), \alpha$ as input.

(2) Calculate $G(u,v), H(u,v)$ by using Fourier transforms.

(3) Initialize: $k = 0, g_0{}^{(k)}(x,y) = g(x,y), G_0{}^{(k)}(u,v) = G^{(k)}(u,v), \lambda^{(k)} = 1$.

(4) Calculate $Q^{(K)}(u,v)$ by using Fourier transform (equation 9.7).

(5) Get $\delta G_{0\mu,v}^{(k)}$ and $\delta g_{0i,j}^{(k)}$ by using inverse Fourier transform.

(6) Renew $g_{0i,j}^{(k+1)} = g_{0i,j}^{(k)} + \delta g_{0i,j}^{(k)}$ and $G_{0u,v}^{(k+1)} = G_{0u,v}^{(k)} + \delta G_{0u,v}^{(k)}$

(7) Calculate λ^* using equation 9.8.

(8) $\lambda^{(k+1)} = (\lambda^* + \lambda^{(k)})/2$.

(9) Go to step (4) if error limit not reached.

9.2 Result Analysis

When using the above flow chart, the most important step is to determine the initial value when doing the iteration. Taking different a, b and $g_0^{(0)}$ could really bring very different iteration cycles. Even worse, when an improper initial value has taken, the iteration itself dose not converge at all. In our experiment, the original image has been taken as the initial value, which is reasonable because the processed image should not have a big divergence from its original one. Another variable that needs to be determined when using maximum entropy method is the point spread function. Since the best PSF has been proved to be the one calculated from the direct deconvolution method, that PSF has been used through all our maximum entropy method. In most cases, the parameters a and b can be taken as any array that satisfies equation 9.2, and the result with a precision below 1e-6 can be reached within 6 iterations, which shows that the equations 9.6-9.8 have a very stable solution.

Figure 9.1 shows the processed image and the original image.

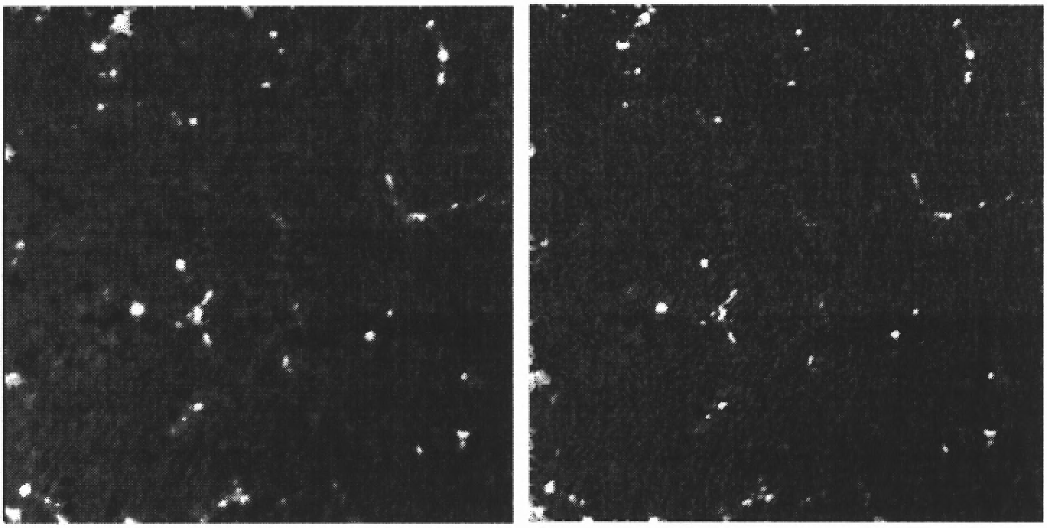

Figure 9.1 Original image and image processed by using maximum entropy method.

The figure tells us that the maximum entropy method could improve the image quality, but the effect in our experiment is not so exciting as the above methods.

The reason could be that the maximum entropy method is more efficient when large-scale scattering light is present[10].

Figure 9.2 shows the amplified local area magnetograph comparison.

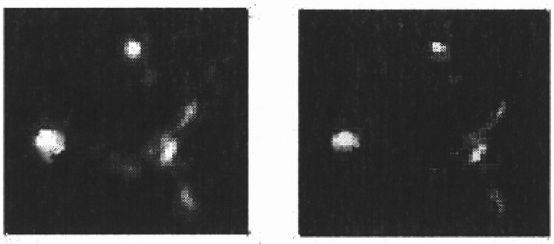

Figure 9.2 Local area comparison, original image and maximum entropy processed image.

Figure 9.3 shows the power spectrum comparison.

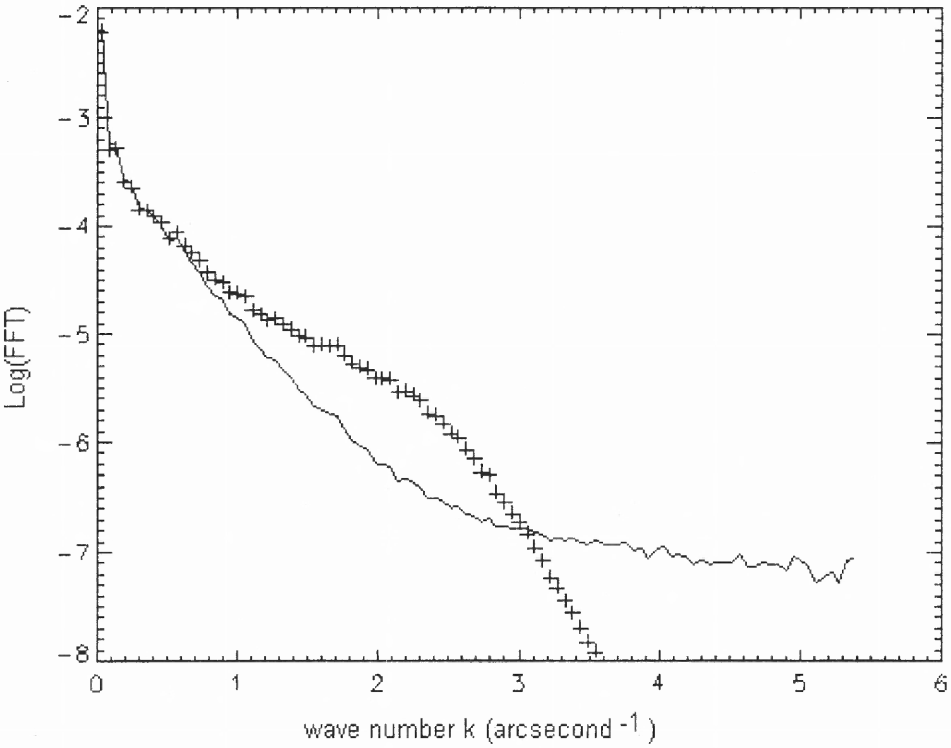

Figure 9.3 Power spectra comparison.

In the figure, the processed image holds the same power as the original image in the lower frequency regime, but in the mid frequency regime, the power is enhanced significantly, which means the maximum entropy works well in some relatively large area. When the frequency becomes higher and higher, the power spectrum begins to drop sharply. This property is some what like that of a Wiener filter. Actually, looking carefully at equation 9.6, it really looks like a Wiener filter except for an extra term in the numerator. When $\alpha=0$, the solution for maximum entropy is an inverse filter. In our experiments, the solution varies very slowly as α changes, but if α is much larger or smaller than 1%, the equations could result in no solution at all.

9.3 Conclusions

The maximum entropy has been proven to be a very effective method in some of the past research studies[10]. But, this is the first time that the method has been used on weak magnetogram of solar granule. In our practice, the maximum entropy method has shown its efficiency. In a very large range, the equations have showed a very stable solution with very high precision (~1e-6). From Fourier spectrum analysis, the processed image showed that the maximum entropy method has some properties similar to that of a Wiener filter. If α is equal to 0, the solution is actually an inverse filter. In our project, the solution is not sensitive to the choice of α. But if α tends to be far from 1% (10 times bigger or smaller as tested), the equations could have no converging solutions at all.

CHAPTER 10

CONCLUSIONS

In the first part, a real-time image alignment system, in the form of correlation tracker has been described. This new correlation tracker does not use the traditional FFT hardware and separated image array detector and A/D processor. A CCD camera, an EDT image board, a D/A converter and a Sun Ultra-30 workstation make up this highly integrated new tracker. Since all the controls come from Ultra-30, which substitutes most of the hardware functions in the old tracker system, the software programming becomes the key component in the new system. For the same reason, the new correlation tracker is more convenient to control and maintain. The test results show that the new correlation tracker has achieved the same efficiency in eliminating image shifts as the other, hardware based trackers developed elsewhere. By using correlation tracker, the integrated image has gained a higher resolution and contrast.

To obtain high-resolution solar magnetogram, a second system, the new digital magnetograph system, has also been built at the Big Bear Solar Observatory. The new digital magnetograph system has significantly improved the sensitivity and spatial resolution over the old BBSO VMG system. The new digital image system has a 12-bits data depth and can detect a polarization signal of about 0.3% by a single pair subtraction compared to the old VMG's 1%. Also, the frame rate has been increased from 30 frames per second to 100 frames per second, under good seeing, which ensures that most of the wavefront distortions are frozen, which makes the images amenable to post-imaging data analysis.

Several different digital image processing methods also have been applied to the digital images obtained from the new system. The different noise deduction methods have been systematically studied in an effort to reduce three main noises, white noise, seeing and stray light. The three kinds of noises have been greatly depressed by using different processing methods, averaging, image selection, destretching, direct deconvolution, Gauss fitting and maximum entropy. The properties, advantages and shortcomings of different processing methods have been investigated by the studies both in spatial and Fourier domain. By considering both method effects and time efficiency, the results indicate that the image selection is the best suitable method to reduce white noise and image shaking. Though destretching method has the best result in eliminating image shift, whether the new parallel system can afford its processing time remains a problem. Another notable method is direct deconvolution. Since the method uses a relatively best image as reference to calculate the PSF without doing any modification, it is much faster than maximum entropy method. The question as to which method will be used at BBSO parallel computing system can only be resolved by the systems speed. Without time limitation, the destreching and maximum entropy methods should be the best methods. When considering time efficiency, the image selection and direct deconvolution methods are recommended.

APPENDIX A

MINIMUM MEAN SQUARE ERROR AND WIENER FILTER

In a linear system, the image i(x,y) is the convolution of original image o(x,y) and system's point spread function h(x,y) plus noise n(x,y), is,

$$i(x',y') = \iint o(x',y')h(x'-x,y'-y)dxdy + n(x',y'). \tag{A.1}$$

The expectation value for o(x,y) is given by,

$$\hat{o}(x,y) = \int m(x',y')i(x-x',y-y')dx'dy'. \tag{A.2}$$

The mean square error is,

$$E = E[\{\hat{o}(x,y) - o(x,y)\}^2]. \tag{A.3}$$

By choosing m to minimize E, the expectation value would be the best value.

Assume $\phi_0(x,y)$ and $\phi_n(x,y)$ are the self correlations of o(x,y) and n(x,y), $\Phi_0(\mu,\nu)$ and $\Phi_n(\mu,\nu)$ are their Fourier transformations. Substituting equations A.1 and A.2 into equation A.3,

$$\begin{aligned} E[\{\hat{o}(x,y) - o(x,y)\}^2] &= \phi_0(0,0) - 2\iint m(x',y')h(x,y)\phi_0(x'+x,y'+y)dxdydx'dy' \\ &+ \iint m(x_1',y_1')m(x_2',y_2')\{\iint h(x_1,y_1)h(x_2,y_2)\phi_0(x_1'+x_1-x_x'-x_2)dx_1dy_1dx_2dy_2 \\ &+ \phi_n(x_1'-x_2',y_1'-y_2')\}dx_1'dy_1'dx_2'dy_2', \end{aligned} \tag{A.4}$$

then,

$$\begin{aligned} E[\{\hat{o}(x,y) - o(x,y)\}^2] &= \iint [\Phi_0(u,v) - \{M(u,v)H(u,v) + M^*(u,v)H^*(u,v)\} \\ &\times \Phi_0(u,v) + |M(u,v)|^2 \{|H(u,v)|^2 \Phi_0(u,v) + \Phi_n(u,v)\}]dudv \\ &= \iint \{|M(u,v) - \frac{H^*(u,v)\Phi_0(u,v)}{\Gamma(u,v)}|^2 \Gamma(u,v) + \frac{\Phi_0(u,v)\Phi_n(u,v)}{\Gamma(u,v)}\}^2 dudv, \end{aligned} \tag{A.5}$$

where,

$\Gamma(u,v) = |H(u,v)|^2 \Phi_0(u,v) + \Phi_n(u,v)$

From equation A.5, to minimize E, the filter M should be:

$$M(u,v) = \frac{H^*(u,v)}{H(u,v)H^*(u,v) + \Phi_n(u,v)/\Phi_0(u,v)}. \tag{A.6}$$

REFERENCES

1. H. Zirin, *Astrophysics of the Sun*, Cambridge University Press, Cambridge, 1988.

2. Chik-Yin Lee, Jongchul Chae, Haimin Wang, "Dynamical Characteristics of Small-Scale Hα Upflow Events on the Quiet Sun", *The Astrophysical Journal*, vol. **545**, no.2, pp. 1124-1134, Dec. 2000.

3. Bin Zhang, Yuanyong Deng, Jinshan Wang, "Acquirement of digital solar magnetic images", *Proc. SPIE*, vol. **3808**, pp. 783-791, Oct. 1999.

4. Christoph U. Keller, "SOLIS: a modern facility for synoptic solar observations", *Proc. SPIE*, vol. **3352**, pp. 732-741, Aug. 1988.

5. Harrison P. Jones, Thomas L. Duvall Jr., John W. Harvey, Charles T. Mahaffey, Jan D. Schwitters, Jorge E. Simmons, " The NASA/NSO spectromagnetograph", *Solar Physics*, vol. **139**, no.2, pp. 211-232, Jun. 1992.

6. M. J. Hagyard, E. A. West, N. P. Cumings, "The new MSFC Solar vector magnetograph", *Final Report National Aeronautics and Space Administration*, Marshall Space Flight Center, Huntsville, AL, Feb. 1984.

7. Patrick Summ, Jean-Philippe Igersheim, "Application of photon-counting techniques to streak camera readout systems", *SPIE*, vol. **4128**, pp. 110-119, Nov. 2000.

8. Haimin Wang, C. Denker, Tom Spirock, P. R. Goode, S. Yang, W. Marquette, J. Varsik, R. J. Fear, J. Nenow and D. D. Dingley, "New Digital Magnetograph At Big Bear Solar Observatory", *Solar Physics*, vol. **183**, no.1, pp. 1-13, November 1998.

9. Jongchul Chae, Hong Sik Yun, Takashi Sakurai, Kiyoshi Ichimoto, "Stray-light effect on magnetograph observations", *Solar Physics*, vol. **183**, no.2, pp. 229-244, Dec. 1998.

10. Jongchul Chae, Hong Sik Yun, Takashi Sakurai, Kiyoshi Ichimoto, "Stray-light correction in magnetograph observations using the maximum entropy method", *Solar Physics*, vol. **183**, no.2, pp. 245-261, Dec. 1998.

11. Rafal C. Ganzalez, Richard E. Woods, *Digital Image Processing*, AddisonWesley Publishing Company, New York, 1993.

12. Charles F. Claver, George H. Jacoby, David R. Silva, Arthur D. Code, "High-speed image motion study at the WIYN3.5-m telescope", *Proc. SPIE*, vol. **3353**, pp. 1130-1137, Sep. 1998.

13. Ronda Venkateswarlu, Merg H. Er, Yu H. Gan, Yew C. Fong, "Area-correlation tracker with improved reliability", *Proc. SPIE*, vol. **3086**, pp. 224-253, Jun. 1997.

14. F. Endler, F. L. Deubner, "The influence of seeing on the observation of short period fluctuations in the solar atmosphere", *Astronomy and Astrophysics*, vol. **121**, no.2, pp. 291-296, May 1983.

15. O. von der Lühe, A. L. Widener, Th. Rimmele, G. Spence, R. B. Dunn, and P. Wiborg, "A solar feature correlation tracker for ground-based telescopes," *Astron. Astrophys.*, vol. **224** , pp. 351-360, 1989.

16. E.Ballesteros, J. A. Bonet, C. Martin, F. J. Fuentes, F. Lorenzo, A. Manescau, T. Viera, J. J. Diaz and E. Joven, "A solar correlation tracker using a video motion estimation processor", *in Site Properties of the Canarian Observatories*, C. Munoz Turon (Ed.) 1997.

17. T. Rimmele, R. R. Radick, and K. S. Balasubramaniam, editors, "High resolution solar physics: theory, observations and techniques", *Proc. 19th Sacramento Peak Summer Workshop*, ASP Conf. Series vol. **183**, pp. 365, 1999.

18. O. von der Lühe, "Measurements of characteristics of image motion with a solar image stabilizing device", *Astronomy and Astrophysics*, vol. **205**, pp. 354-360, 1998.

19. O. von der Lühe, "A study of a correlation tracking method to improve imaging quality of ground-based solar telescopes", *Astronomy and astrophysics*, vol. **119**, pp. 85-94, 1983.

20. E.Ballesteros, M. Collados, J. A. Bonet, F. Lorenzo, T. Viera, M. Reyes and I. Rodrigues Hidalgo, "Two dimensional, high spatial resolution, solar spectroscopy using a Correlation Tracker", *Astronomy and astrophysics*, Suppl. Ser. Vol. **115**, pp. 353-365, 1996.

21. Th. Rimmele, O. von der Lüke, P.H. Wilborg, A. L. Widener, R. B Dunn, G. Spence, "Solar feature correlation tracker", *Proceedings of SPIE International Symposium on Optical Applied Science and Engineering*, vol. **1542**, pp. 186-193, San Diego, CA, July 1991.

22. A. Clocchiatti, F. Courbin, High-Z Supernova search team, "Background matching & subtraction versus PSF deconvolution: comparison of two photometric techniques applied to images", American Astron. Soc. Meeting, vol. **197**, pp. 1705, 2000.

23. Z. Tang, S. Wang, W. Jin, "Removal of Tracking Error with Image Restoration", *The Astronomical Journal*, vol. **121**, no.2, pp. 1199-1206, Feb.2001.

24. Brian D. Jeffs, Julian C. Christou, "Blind Bayesian restoration of adaptive optics telescope images using generalized Gaussian Markov random field models", *Proc. SPIE.*, vol. **3353**, pp. 1006-1013, Sep. 1998.

25. P. Magain, F. Courbin, S. Sohy, "Deconvolution with Correct Sampling", *Astrophysical Journal*, vol. **494**, pp. 472, Feb. 1998.

26. Jean-Marc Conan, Michau Vincent, Gerard Rousset, "Signal-to-noise ratio and bias of various deconvolution from wavefront sensing estimators", *Proc. SPIE*, vol. **2828**, pp. 332-339, Oct. 1996.

27. T. Zaccheo, "Digital Image Restorations: Algorithms and Accuracy with Applications to Astronomical Observations", *Dissertation Abstracts International*, TUFTS University, vol. **56**, no.5, Section B, pp. 2801, Jan. 1995.

28. J. Starck, A. Bijaui, I. Valtchanov, F. Murtagh, "A combined approach for object detection and deconvolution", *Astronomy and astrophysics Supplement*, vol. **147**, pp. 139-149, Nov. 2000.

29. Julian C. Christou, Stuart M. Jefferies, E. Hege, "Object-independent point spread function and wavefront phase estimation", *Proc. SPIE*, vol. **3762**, pp. 201-210, Sep. 1999.

30. Noriake Miura, Naoshi Baba, Takashi Sakurai, Kiyoshi Ichimoto, Dirk Soltau, Peter Brandt, "Resolution Improvement of Solar Images", *Solar Physics*, vol. 187(2), pp. 347-356, Jul. 1999.

31. J. Sylwester, B. Sylwester, "Reconstruction of Images with Poisson Noise", *Acta Astronomica*, vol. **49**, pp. 189-199, Jun. 1999.

32. O. Bendinelli, G. Parmeggiani, "Multi-Gaussian deconvolution of elliptical sources: Reliability tests using ground-based and HST images", *Astronomical Journal*, vol. **109**, no.2, pp. 572-578, Feb. 1995.

33. S. Zaroubi, Y. Hoffman, K. B. Fisher, O. Lahav, "Wiener Reconstruction of the Large-Scale Structure", *Astrophysical Journal*, vol. **449**, pp. 446, Aug. 1995.

34. J. Starck, F. Murtagh, P. Querre, F. Bonnarel, "Entropy and astronomical data analysis: Perspectives from multiresolution analysis", *Astronomy and Astrophysics*, vol. **368**, pp. 730-746, Mar. 2001.

35. Stella Seitz, Peter Schneider, Matthias Bartelmann, "Entropy-regularized maximum-likelihood cluster mass reconstruction", *Astronomy and Astrophysics*, vol. **337**, pp. 325-337, Set. 1998.

36. M. P. Hobson, A. N. Lasenby, "The entropic prior for distributions with positive and negative values", *Monthly Notices of the Royal Astronomical Society*, vol. **298**, no.3, pp. 905-908, Aug. 1998.

37. J. Nunez, J. Llacer, "Bayesian image reconstruction with space-variant noise suppression", *Astronomy and Astrophysics Supplement*, vol. **131**, pp. 167-180, Jul. 1998.

38. B. R. Frieden, J. David, "Closed-form maximum entropy image restoration", *Proc. SPIE,* vol. **3164**, pp. 140-148, Oct. 1997.

39. K. Arzner, A. Magun, "Fast maximum entropy restoration of low-noise solar images", *Astronomy and Astrophysics*, vol. **324**, pp. 735-742, Aug. 1997.

40. H. Wang, F. Tang, H. Zirin, J. Wang, "The Velocities of Intranetwork and Network Magnetic Fields", *Solar Phys.*, vol. **165**, pp. 223, 1996.

41. P.L. Rosin. Measuring corner properties. *Technical Report CSTR-96-18*, Brunel University, 1996.

42. J. Yan, P. Campisi, D. Hatzinakos, "Filem Grain Noise Removal and Generation for Color Images", *ICASP '98 meeting*, 1998.

43. Eero P. simoncelli, Edward H. Adelson, "Noise removal via Bayesian wavelet corning", *3rd IEEE Int'l Conf on Image Processing*, Lausanne, Switzerland, Sep. 1996.

44. V. Abramenko, V. Yurchyshn, H. Wang, P. R. Goode, "Magnetic power spectra in the solar photosphere derived from Ground and space based observations", *Solar Physics*, 2001, in press.

45.R. E. Hufnagel, N. R. Stanley, "Modulation Transfer Function Associated with Image Transmission through Turbulent Media", JOSA, Vol. **54**, no.1, pp. 52, January 1964.

46. O. Espagnet, R. Muller, T. Roudier, N. Mein, "Turbulent power spectra of solar granulation", Astron. Astrophys, vol. **589**, pp. 271, 1993.

47. S. F. Gull, J. Skilling, *Maximum Entropy and Bayesian Methods*, Kluwer Academic Publishers, Cambridge, England, 1989.

48. Dalsa Inc., *1996-1997 Data Book*, Ontario, Canada, 1996.

49. EDT. Inc., *PCI DV User's Guide*, March 2000.

50. Sun Microsystems Inc., *Sun Ultra 30 Reference Menu*, March 1997.

51. Sun Microsystems Inc., *I/O Technologies and Solutions*, 1990-2001

52. ADLink Technology Inc, *NuDAQ 6208 Series Multi-channel Analog Output Board User's Guide,* October 1999